UNIVERSITY OF CALIFORNIA SAN DIEGO

New observations of fine-scale physical and biogeochemical dynamics enabled by ocean-wave-powered profiling

A Dissertation submitted in partial satisfaction of the requirements
for the degree Doctor of Philosophy

in

Oceanography

by

Bofu Zheng

Committee in charge:

Andrew J. Lucas, Chair
Falk Feddersen
Peter J.S. Franks
Jennifer A. MacKinnon
Sutanu Sarkar
Amy Waterhouse

2023

The Dissertation of Bofu Zheng is approved, and it is acceptable in quality and form for publication on microfilm and electronically.

University of California San Diego

2023

DEDICATION

I would like to dedicate this dissertation to my dad Jingping Zheng, and my mum Yuju Yang for their forever love.

EPIGRAPH

诸位在校，有两个问题应该自己问问：第一，到浙大来做什么？第二，将来毕业后做什么样的人？

竺可桢

气象学家，浙江大学前校长

Two questions that you should ask yourself: first, what do you want to accomplish during your time here? second, what kind of person do you want to become afterward?

Chu, Kochen

Meteorologist, former president of Zhejiang University

TABLE OF CONTENTS

LIST OF FIGURES

ACKNOWLEDGEMENTS

Training a student to become a Ph.D. is a multidimensional task, where the advisor cultivates students in every scientific aspect. The task is even more difficult if the student's first language is not English. Drew is a wonderful advisor, and more importantly, my friend. I am fortunate to have Drew because he is always by my side, supporting me, guiding me, criticizing me (in a good way), and inspiring me. Drew expects me to become the best in my field and he takes every opportunity -- meetings, emails, and numerous slack messages -- to equip me with all the necessary skills I need for the good of my future. Drew gifts me the ability to live a good life far beyond the scientific world. Indeed, I can't find a better advisor. Thank you Drew for shaping me into a better myself! You are the BEST!

I want to thank my committee members, Peter, Jen, Amy, Falk, and Sutanu for providing support and help whenever I need them. It always feels warm knowing that I have people on my back. Here, especially to Peter, my academic grandfather, and Dr. November, I want to thank you for your scientific insights, attitude to perfection, and spirit of jokes -- I leaned so much from you.

I want to thank all my collaborators, Tamara, Arnaud, Rob, Peter, Kristen, Uwe, Clarissa, and Andrew. Every single discussion, comment, and email exchange makes the project more exciting and the paper in better shape. I benefit a lot from you guys by learning not only cutting-edge knowledge but more importantly the methodology to do good science, from targeting questions, testing hypotheses, and telling stories.

I want to thank all the professors who taught me oceanography knowledge, including Profs. Ying Chen, Haocai Huang from Zhejiang University, Dr. Weifeng (Gordon) Zhang from WHOI, and all my SIO instructors. You laid a solid foundation for me.

I want to thank my parents for their endless love throughout my whole life. Thank you for bringing me into this world. Thank you for giving me the freedom to choose what I want to do. Love you forever!

I want to thank my Applied Ocean Science (AOS) family, Annie, Billy, Eric, Kelley, and Narda. You guys gave me a family when I came to the US alone. I feel included, happy, and relaxed surrounded by you. Remember the moments when we ate tacos, laughed in the office, and complained about the homework?

I want to thank the MOD group for all the support. On the engineering side, Riley and Mike provided instrumental help. On the science side, it was so fun discussing scientific problems, let alone riding the ocean together on research cruises with MODers. Special thanks to Alex for being an awesome officemate – hope the best for the stop sign on Naga Way.

I want to thank Mayday -- my favorite band. Your music accompanied me through countless days and nights, healed me with your tenderness, and empowered me with your uplifting spirits.

Finally, even though I hate COVID, I feel grateful for it teaching me to cherish. Make every second count when being with loved ones, because this intercept in space and time is a miracle in life. ☺

Chapter 1, in full, is a reprint of the material as it appears in: Zheng, B., Lucas, A.J., Pinkel, R., Le Boyer, A. (2022). Fine-Scale Velocity Measurement on the Wirewalker Wave-Powered Profiler. *Journal of Atmospheric and Oceanic Technology*, 39(2), 133–147. The dissertation author was the primary investigator and author of this paper.

Chapter 2, in part, has been submitted for publication of the material as it may appear in *Proceedings of the National Academy of Sciences of the United States of America*, Zheng, B., Lucas, A.J., Franks, P.J.S., Schlosser, T., Anderson, C., Send, U., Davis, K., Barton, A. (2023). The dissertation author was the primary researcher and author of this paper.

Chapter 3, in part is currently being prepared for submission for publication of the material. Zheng, B., Lucas, A.J., Schlosser, T., Anderson, C., Send, U., Davis, K. (2023). The dissertation author was the primary researcher and author of this material.

VITA

2017 Bachelor of Engineering in Mechanical Engineering
Zhejiang University

2022 Master of Science in Oceanography
Scripps Institution of Oceanography
University of California San Diego

2023 Doctor of Philosophy in Oceanography
Scripps Institution of Oceanography
University of California San Diego

PUBLICATIONS

Zheng, B., Lucas, A.J., Schlosser, T., Anderson, C., Send, U., Davis, K. (2023). Multiscale physical control of cross-shore nitrate gradient over the inner continental shelf. In prep for *Limnology and Oceanography.*

Zheng, B., Lucas, A.J., Franks, P.J.S., Schlosser, T., Anderson, C., Send, U., Davis, K., Barton, A. (2023). Dinoflagellate vertical migration fuels an intense red tide. Submitted to *Proceedings of the National Academy of Sciences of the United States of America.*

Zheng, B., Lucas, A.J., Pinkel, R., Le Boyer, A. (2022). Fine-Scale Velocity Measurement on the Wirewalker Wave-Powered Profiler. *Journal of Atmospheric and Oceanic Technology*, 39(2), 133–147.

ABSTRACT OF THE DISSERTATION

New observations of fine-scale physical and biogeochemical dynamics enabled by ocean-wave-powered profiling

by

Bofu Zheng

Doctor of Philosophy in Oceanography

University of California San Diego, 2023

Professor Andrew J. Lucas, Chair

Novel instrumentation plays a crucial role in enabling new observations and providing deeper insights into ocean dynamics. In my thesis, I present methodologies for collecting high

spatial-temporal resolution observational data, which allows for a better understanding of physical and biogeochemical processes in the coastal ocean. Specifically, I integrate two novel sensors, the acoustic Doppler current profiler (ADCP) and the Submersible Ultraviolet Nitrate Analyzer (SUNA), onto the Wirewalker (WW) wave-powered profiler. I discuss issues related to fine-scale velocity measurements, biological modulation of nitrate during a harmful algal bloom, and nitrate dynamics over the inner continental shelf.

The thesis begins by presenting a new methodology to observe oceanic fine-scale velocity using the combination of velocimeters and the Wirewalker profiler. By correcting vehicle-motion-induced velocity contaminations and removing surface wave signals, a background velocity field with a spectrum wavenumber runoff at a scale of ~3 m over a 100 m vertical range was obtained. This vertical resolution is several times finer than that possible from other velocity-measuring platforms with similar measurement ranges.

Next, I present in situ evidence demonstrating the vertical migration of the dinoflagellate that facilitates their nitrate uptake during the 2020 red tide in the Southern California Bight. The vertical migration pattern of Lingulodinium polyedra (the dominant species) and their biological modulations to the subsurface nitrate field were quantified. The loss of nitrate in the nitracline was balanced by proportional increases in phytoplankton concentrations, confirming a 50-year-old hypothesis. The swimming ability of the dinoflagellate allows them to outcompete other non-motile phytoplankton during times of high stratification and nutrient limitation.

Finally, an undocumented onshore-directed cross-shore nitrate gradient over the inner shelf of the Southern California Bight was revealed. The nitrate gradient was possibly formed by enhanced vertical nitrate flux due to elevated turbulent diffusivity when isopycnals

constantly impinged on a sloping sea floor. Furthermore, the study demonstrated that near-inertial internal waves were responsible for transporting the onshore nitrate offshore, providing a new mechanism for fueling the offshore primary productivity. These findings highlight the need for new instrumentation to better understand complex coastal biogeochemical dynamics.

INTRODUCTION

Ocean observation

Observations are crucial for gaining an improved understanding of the ocean. New signals in the observational data that cannot be explained by existing knowledge, will lead to new theories and insights into our natural world.

Novel ocean observations rely heavily on implementing advanced observational technologies. Over the past 100 years, ocean observation tools have greatly improved from the traditional mechanical sensors and water samplers, such as Nansen bottles to modern high-frequency electro-mechanical sensors, such as conductivity-temperature-depth (CTD) sensors, acoustical sensors, and optical sensors. Furthermore, ocean observational platforms have upgraded from coastal-scale fishing boats to global-scale research vessels, accompanied by the emergence of autonomous sampling platforms, such as moorings, floats, gliders, and satellites. Implementation of these cutting-edge technologies, through combinations of sensors and platforms, has fundamentally expanded our knowledge of nearly all aspects of oceanography, ranging from physical processes to biogeochemical dynamics.

Generally, there are two primary directions for future ocean observation technology development: 1) reliable higher-resolution temporally and spatially-resolved data collection tools; and 2) quantifications of variables and processes that are impossible to achieve before. For my thesis, I advanced the high-resolution data collection of two important ocean properties, namely, velocity and nitrate, and studied how physical and biogeochemical processes modulate the coastal nitrate field.

High-resolution data collection requires high-resolution sensors deployed on oceanic platforms capable of achieving certain spatial and temporal coverage. The primary oceanic

platform I used is called the Wirewalker (WW), an ocean wave-powered profiler. The WW was developed at Scripps Institution of Oceanography (SIO) about 20 years ago, led by Prof. Robert Pinkel (Rainville and Pinkel 2001). WW uses mechanical rectification of ocean-surface-wave-induced buoy motion to drive itself vertically downward along a wire (Rainville and Pinkel 2001; Pinkel et al. 2011). Upon reaching the bottom of the desired profiling range, the profiling cam is released, and subsequently, the WW ascends to the surface due to its positive buoyancy (Rainville and Pinkel 2001; Pinkel et al. 2011). Mounted with multiple sensors, the WW enables the collection of physical and biogeochemical properties of the upper ocean, including temperature, salinity, density, chlorophyll, optical backscatter, nitrate concentration, and velocity (Lucas et al. 2017). The energy for vertical profiling in the WW system is provided by the ocean waves, which allow for prolonged measurements of the internal wave continuum (Lucas et al. 2017). Typical WW vertical velocity averages 0.5 m s^{-1}, permitting several-hundred-meter profiles to be covered on time scales of tens of minutes continuously over the course of a deployment. Of the variables the WW can measure, reliable ocean velocity and nitrate concentration observations remain elusive goals.

Ocean velocity is one of the most fundamental physical properties of the ocean. Characterization of ocean velocity is crucial for our understanding of the transport of oceanic mass, energy, and momentum. The most widely used instrument for measuring ocean velocities -- the acoustic Doppler current profiler (ADCP) -- utilizes the Doppler frequency shift between transmitted and received acoustic signals scattered by drifting particles to determine the current speed at a set of ranges from the transducer (Pinkel 1980). ADCP is limited by a fundamental trade-off between sensing range and spatial resolution. For example, when transmitting lower-frequency acoustic waves, commercially available ADCPs can gather velocity observations over

longer ranges with coarse range resolution (e.g., a 50 kHz ADCP can cover ~1000 m at ~20 m resolution). On the other hand, when using higher frequency signals, which attenuate quickly, ADCPs achieve observations at shorter ranges with finer range resolution (e.g., a ~1000 kHz ADCP may only reach 20 m, but can do so at ~1 m resolution).

Nitrate is the most common limiting macronutrient for phytoplankton to grow and photosynthesize and thus plays a pivotal role in controlling the primary productivity of the ocean (Howarth 1988). Historically, people needed to collect and freeze water samples, and then analyze nitrate concentration following step-by-step procedures in specially designed lab facilities (e.g., Eppley et al. 1979). This procedure generally takes weeks, which fundamentally prohibits the study of nitrate dynamics over short temporal scales. About 20 years ago, a convenient, relatively small-size, and high-resolution nitrate sensor was invented (Johnson and Coletti 2002) and was further developed and commercialized into SUNA (Submersible Ultraviolet Nitrate Analyzer, Sea-Bird Scientific). SUNA utilizes the absorption spectrum of the water sample in the UV light region to determine nitrate concentration (Johnson and Coletti 2002). It is capable of achieving a sampling rate of ~1 Hz, with an accuracy of 2 mmol N m^{-3}, and a precision of 0.3-2.4 mmol N m^{-3}, depending on the instrument configuration. SUNA has demonstrated the ability to collect reliable long-term fixed-depth nitrate data on traditional moorings (e.g., Sakamoto et al. 2017) as well as vertical profiles of nitrate from floats (e.g., Johnson et al. 2017), expanding our toolbox to unveil small-scale biogeochemical processes.

Dissertation outline

For my first chapter, the objective is to come up with a method to observe oceanic fine-scale velocity with high spatial-temporal resolution and high spatial coverage. We utilized a combination of the WW and a commercially available ADCP. The ADCP was mounted in a down-

looking orientation on the bottom of the WW and profiled through the water column carried by the WW. Using data collected from the attitude heading reference system (AHRS) on the ADCP, we developed a motion-calculation algorithm to estimate the subsurface vehicle motion and consequently subtracted it from the raw velocity measurements. Furthermore, the ~20 m sampling range of the ADCP and vertical motion of the WW enabled the collection of velocity data with a temporal coverage at each depth. Thus, we applied a range-and-time averaging approach -- box averaging -- to minimize errors and surface wave impacts, and to obtain a reliable fine-scale oceanic velocity field. We demonstrated that our method is capable of producing velocity estimates that can characterize the ocean fine-scale velocity field to vertical wavenumbers of 1/3 cycles per meter, over a 100 m vertical range, every few minutes.

For my second chapter, the objective is to test a historical hypothesis that the vertical migration ability of dinoflagellates enables them to outcompete other stationary phytoplankton by swimming upward during the day to photosynthesize and downward at night to access the deep nutrient pool. We collected high-resolution physical and biochemical data using novel sensors (including SUNA) onboard the WW during a harmful algal bloom in the Southern California Bight (SCB) in the spring of 2020. We quantified the vertical migration pattern of *Lingulodinium polyedra* (the dominant phytoplankton species during this bloom), whereby they started downward migration at dusk and reached the nitracline after 18~24 hours of migration with an average speed of ~1.4 m h^{-1}. In the nitracline, these phytoplanktons took up nitrate at a rate of ~6 mmol N m^{-3} day^{-1}, causing a nitrate loss of up to 12 mmol N m^{-3}, ~10 m vertical region over ~3 days. We found that the loss of nitrate in the nitracline was proportionally balanced by the increase in phytoplankton chlorophyll concentrations. These in-situ data provide evidence supporting the hypothesis that vertical migration allows dinoflagellates to acquire nitrate from the deep nutrient

pool and thus fuels the bloom. We also demonstrated that dinoflagellates can temporarily reshape the coastal ocean ecosystem by extending the nitracline downward by ~25 m -- well below the euphotic zone -- with a nitrate depletion up to 14 mmol N m^{-3}. These observations indicate a dramatic biogeochemical consequence of the red tide.

For my third chapter, the objective is to quantify the cross-shore nitrate gradient over the inner continental shelf of SCB and study how this nitrate gradient is modulated by multi-scale physical processes. We presented high-resolution physical and biogeochemical observations collected from three cross-shore mooring arrays, including a 20 m shallow mooring at the nearshore end, a 50 m WW in the middle, and a 100 m deep mooring at the offshore end. We identified a cross-shore along-isopycnal nitrate gradient with an amplitude of 0.75 mmol N m^{-3} km^{-1} increasing onshore. This nitrate gradient was temporally correlated with a downwelling event that gradually propagated onshore and pushed the previously surfaced isopycnal into the bottom boundary layer. We provided evidence suggesting the nitrate source at the onshore end was due to enhanced vertical nitrate flux when the isopycnal rushed along the sloping sea floor driven by energetic internal waves over several days. The turbulent diffusivity in the bottom boundary layer was quantified to be ca. 2.5 - $13*10^{-4}$ m^2 s^{-1}. Furthermore, we identified a ~1 cycle per day nitrate oscillation signal that was suggested to be induced by horizontal advection via near-inertial waves along the isopycnal in the cross-shore direction. This provides a new dynamical mechanism for the onshore region to fuel the offshore primary productivity in the SCB.

CHAPTER 1: FINE-SCALE VELOCITY MEASUREMENT ON THE WIREWALKER WAVE-POWERED PROFILER

Abstract

The Wirewalker (WW) ocean-wave-powered vertical profiling system allows the collection of high-resolution oceanographic data due to its rapid profiling, hydrodynamically quiet operation, and long endurance. We have assessed the potential for measuring fine-scale ocean velocities from the Wirewalker platform using commercially available acoustic velocimeters. Although the vertical profiling speed is relatively steady, platform motion affects the velocity measurements and requires correction. We present an algorithm to correct our velocity estimates using platform motion calculated from the inertial sensors -- accelerometer, gyroscope, and magnetometer -- on a Nortek Signature1000 Acoustic Doppler Current Profiler. This correction, carried out ping-by-ping, was effective in removing the vehicle motion from the measured velocities. The motion-corrected velocities contain contributions from surface wave orbital velocities, especially near the surface, and the background currents. To proceed, we use an averaging approach that leverages both the vertical platform profiling of the system and the ~15-20 m vertical profiling range resolution of the down-looking ADCP to separate the surface wave orbital velocities and the background flow. The former can provide information on the wave conditions. From the latter, we are able to estimate fine-scale velocity and shear with spectral wavenumber roll-off at vertical scales around 3 m, a vertical resolution several times finer than that possible from modern shipboard or fixed ADCPs with similar profiling range, and similar to recent glider measurements. When combined with a continuous time-series of buoy drift calculated from the onboard GPS, a highly resolved total velocity field is obtained, with a unique combination of space and time resolution.

Introduction

In the ocean, processes on vertical scales of several meters or less -- the so-called “fine-scale" -- play an important role in the general circulation by linking internal waves and turbulence. The advent of accurate, high precision conductivity-temperature-depth measurements allows the fine-scale density structure of the ocean to be assessed in a relatively straight-forward manner. Obtaining similarly precise measurements of fine-scale oceanic velocity, on the other hand, remains an elusive goal, especially over large depth ranges in the open ocean. Acquiring these velocity measurements is a critical requirement for understanding and predicting physical problems like boundary layer dynamics (e.g., Shcherbina et al. 2018), internal wave-driven mixing (e.g., Alford 2010), and biophysical interactions (e.g., Garwood et al. 2020, 2021).

The most widely used instrument for measuring ocean velocities -- the acoustic Doppler current profiler (ADCP) -- utilizes the Doppler frequency shift between transmitted and received acoustic signals scattered by drifting particles to determine the current speed at a set of ranges from the transducer (Pinkel 1980). This approach to measuring ocean velocity by a fixed or ship-installed ADCP is characterized by a fundamental trade-off between sensing range and spatial resolution. For example, commercially available ADCPs can use low-frequency transmissions to gather velocity observations over long ranges with coarse range resolution, or use higher frequencies -- which attenuate quickly -- for shorter ranges with finer range resolution. For example, a 50 kHz ADCP can cover ~1000 m at 20 m resolution, while a ~1000 kHz ADCP may only reach 20 m, but can do so at < 1 m resolution.

Thus, primarily due to the range limitation of acoustic instruments for collecting velocity with high spatial resolution, measurements of fine-scale velocity in the open ocean are relatively uncommon. Recently, autonomous vertical profiling platforms like buoyancy-driven gliders and

Lagrangian floats have shown great promise in overcoming this limitation by vertically cycling short-range, high-frequency ADCPs (e.g., Todd et al. 2017; Shcherbina et al. 2018) These approaches provide vertically well-resolved velocities relative to the vehicle, but must surface to acquire the GPS fixes necessary to calculate absolute ocean velocity.

Measuring ocean velocities acoustically from any moving platform is inherently more difficult than measuring them from a fixed location since the platform motion must be removed from the Doppler measurements of velocities to obtain flow speed and direction. Tracking rapid changes in platform motion can be done by the use of an Attitude and Heading Reference System (AHRS) to measure acceleration, angular rate of rotation, and heading relative to Earth's magnetic field using a 3-axis accelerometer, a 3-axis angular rate sensor, and a 3-axis magnetometer, respectively. The extraction of platform motion from velocity measurements via accelerometers, inertial measurement units, and AHRS approaches has been used successfully to improve the precision of velocity and turbulence measurements (e.g., Bluteau et al. 2016; Harding et al. 2017; Kilcher et al. 2017; Zippela et al. 2018). Similar platform motion corrections are also applied to shipboard ADCP systems in use in the global research fleet.

Here, we add to those efforts by providing a methodology to estimate the total and fine-scale velocity from the Wirewalker wave-powered profiling system (Rainville and Pinkel 2001; Pinkel et al. 2011; Lucas et al. 2017) utilizing an AHRS-based ping-by-ping motion correction and a range-and-time averaging approach. These vehicle-relative velocities are then combined with GPS-derived buoy position to determine the total current. Our approach is inspired by techniques used to estimate velocity from shipboard rosette-mounted “lowered” ADCP (LADCP, e.g., Firing and Gordon 1990) and from buoyancy-driven gliders (e.g., Todd et al. 2017).

Previous efforts to measure velocity onboard the Wirewalker

The Wirewalker was developed at Scripps Institution of Oceanography (SIO) and uses mechanical rectification of ocean-surface-wave-induced buoy motion to drive a profiling body vertically downward along a wire (Rainville and Pinkel 2001). Upon reaching the bottom of the desired profiling range, the profiling cam is released, and the vehicle ascends to the surface due to its positive buoyancy. Equipped with a Conductivity-Temperature-Depth sensor (CTD), a fluorescence sensor, a nutrient sensor, and an ADCP, the Wirewalker measures physical properties of the upper ocean, including density, chlorophyll, nitrate concentration, and velocity (Lucas et al. 2017). The energy for vertical profiling in the Wirewalker system is provided by the ocean waves which allows for prolonged measurements of the internal wave continuum. Typical Wirewalker vertical velocity averages 0.5 m/s, permitting several hundred meter profiles to be covered on time-scales of tens of minutes continuously over the course of a deployment (Pinkel et al. 2011).

We have made several attempts to measure velocity from the Wirewalker using commercially available velocity sensors. Most of our early efforts focused on single-point Doppler velocimeters, e.g., the Nortek Aquadopp and Aquadopp High Resolution (HR) systems. These single-point velocimeters produce a velocity estimate at a single range (generally < 1 m from the transducer) or over a very short range interval (HR) several times per second. When mounted on a vertically profiling Wirewalker, time averages in the vertical can be assembled within bin sizes of several meters containing dozens of velocity observations. In this way, estimates of horizontal velocity are produced on vertical profiles (Lucas et al. 2016; Hamann 2019).

We found that this technique -- while yielding acceptable sub-surface velocities below depths of ~100 m -- contains a mix of low-frequency and surface wave orbital velocities at

shallower depths. These are combined with wave-induced motion of the Wirewalker to produce a signal that is challenging to interpret.

In order to address the contamination of the measured velocities by vehicle motion, we gathered information on the translational and rotational motion of the Wirewalker during the free-ascent profile. To do so, we fitted the Wirewalker with a Nortek 1000 kHz Signature ADCP with onboard AHRS sensors, sampling at 16 Hz (Nortek 2011). The Signature has four slanting beams at 25^{o} from vertical and one fifth vertical beam (not used in our experiment). The ADCPs were attached to the Wirewalker in two different orientations and tested to assess the degree to which measurement noise could be reduced by removing the Wirewalker motion on a ping-by-ping basis (Fig. 1.1).

First, the ADCP was mounted in a "horizontal-looking" (90 degrees to the vertical) orientation (Fig. 1.1a). We tested this side-looking configuration in both standard and High-Resolution (HR) mode of Signature1000 on short test deployments in the waters offshore of Southern California. The results of those experiments are not shown here, but they indicated that a motion-compensation side-looking configuration had improved velocity precision relative to a single point current meter at depth, but suffered from the same inability to separate surface wave orbital velocities from background currents.

We next tested a vertically down-looking orientation (Fig. 1.1b) during an Office of Naval Research sponsored cruise in the Northern Indian Ocean (MISO-BOB 2019). With those data, we show that motion correction and a combination of range/depth/time averaging -- which we refer to here as "box" averaging -- is capable of producing velocity measurements with high vertical resolution even in the surface mixed layer.

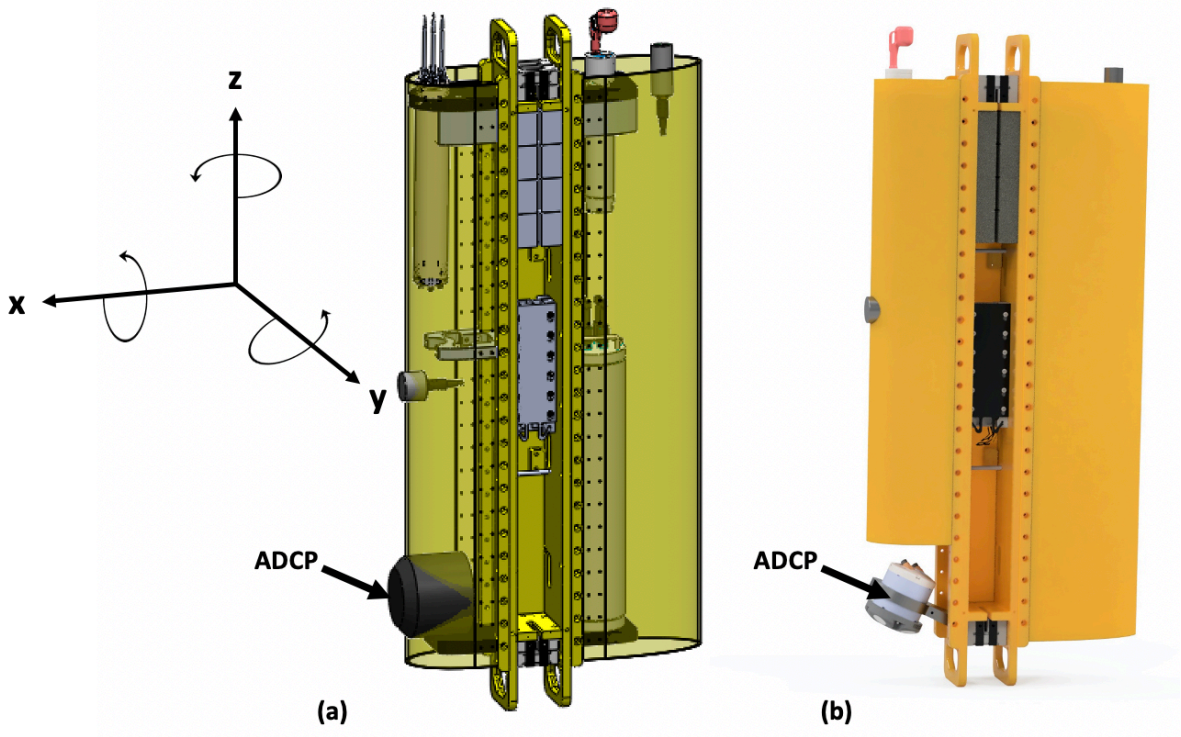

Figure 1.1 Schematic drawing of side-looking ADCP (a) and down-looking ADCP (b) respectively. Here, down-looking orientation is ~20 degrees offset from vertical. The axes notation used throughout this paper is: uppercase (XYZ) referring to ADCP's coordinate system and lower case (xyz) referring to Wirewalker's coordinate system. Here, we define the Wirewalker xyz coordinate system with x positive pointing forward, nominally upstream, y positive pointing nominally cross stream, to the right of x, and z positive pointing up.

In the following, we analyze the Wirewalker motion using the onboard AHRS sensor and present an algorithm to calculate vehicle motion integrated forward from the acceleration measurements to ENU velocities (Section 2). After providing the down-looking ADCP configuration and relative deployment information in Section 3, we then show fine-scale velocity observations estimated after motion correction and a novel depth/range/time average from the down-looking configuration (Section 4) and provide a discussion and conclusion (Sections 5 and 6).

Wirewalker Motion

We gain intuition regarding the Wirewalker motion by examining the accelerometer and gyroscope measurements. As shown in Fig. 1.2, the amplitude of the measured motion is small at depth and increases as the Wirewalker approaches the surface. This increase in acceleration and rotational motion towards the surface matches the theoretical shape of the surface gravity wave orbital velocities in the deep-water approximation, which decays exponentially with depth, indicating a tight relationship between Wirewalker horizontal motion and the surface wave field (compare to the exponential curve shown as dashed lines in Fig. 1.2c). Furthermore, the power spectra in Fig. 1.2 have peaks in the surface wave band (2-25 seconds), which is consistent with the interpretation that the cause of the observed motion is primarily due to surface-wave-induced displacements of the surface buoy and the orbital velocity induced motion of the Wirewalker package.

Next, we calculate the motion of the Wirewalker using a rigid body assumption, allowing the motion to be decomposed into translational and rotational components, represented as $\mathbf{V}_{\text{motion}} = \mathbf{V}_{\text{translation}} + \mathbf{V}_{\text{rotation}}$. The rotational velocity ($\mathbf{V}_{\text{rotation}}$) is calculated as $\mathbf{V}_{\text{rotation}} = \boldsymbol{\omega} \times \mathbf{H}$, where $\boldsymbol{\omega}$ is the angular rate of rotation measured by the gyroscope and $\mathbf{H}$ is the distance between the rotation center and ADCP (~1, 1, 0.4 m, for ω_x, ω_y, and ω_z, respectively, set by the geometry of the Wirewalker). The translational velocity can be calculated as: $\mathbf{V}_{\text{translation}} = \int \mathbf{a}_{dynamic} dt$, where $\mathbf{a}_{dynamic}$ is the dynamic acceleration. As raw acceleration from the accelerometer is measured relative to its own inertial frame at each time, dynamic acceleration relative to the Earth can only be obtained by extracting the acceleration of the inertial frame relative to the Earth, which is called static acceleration here, from the raw data. This static acceleration can be calculated as:

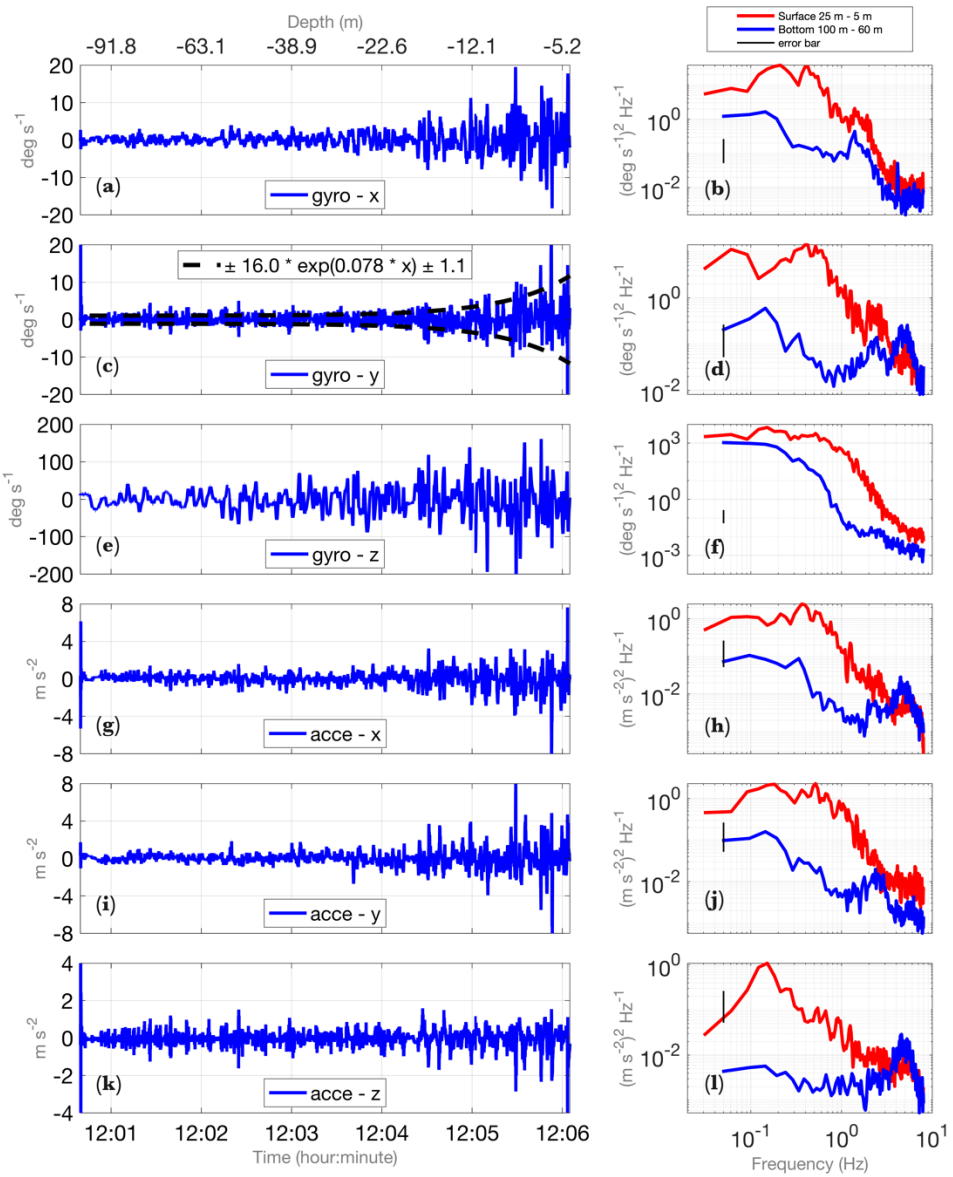

Figure 1.2 AHRS measurements during one Wirewalker profile (the same profile used throughout the paper, collected during the ONR MISOBOB-2019 cruise). A gyroscope records the rotation of the Wirewalker around its x (in a), y (in c), and z (in e) axes respectively and the three-axis accelerometer measures linear acceleration along x (in g), y (in i) and z (in k) axes respectively. Note that all signals presented here have already been transformed from the ADCP coordinate system to Wirewalker coordinate system (Fig. 1.1). For all panels to the left, time is shown in the lower x-axis and the corresponding Wirewalker's vertical location is shown in the upper x-axis. Note that the positive rotating direction is defined by the right-hand rule. Dashed lines in c show the envelope of the signal as a function of depth via least-squares-fitting peaks of the measurement signal with an exponential function. Panels on the right show the spectrum results of the corresponding signal at the surface and bottom region respectively, with thin black lines as error bars.

$$a_{static,X} = sin(\phi)g$$

$$a_{static,Y} = sin(\theta)cos(\phi)g \quad (1)$$

$$a_{static,Z} = cos(\theta)cos(\phi)g,$$

where g is gravitational acceleration, θ is roll angle and ϕ is pitch angle. Thus, the translational motion of the Wirewalker can be calculated from the AHRS system on the Signature1000 using the following steps:

1) Obtain dynamic acceleration

Dynamic acceleration can be obtained by removing static acceleration [Eq. (1)] from raw acceleration which is given below:

$$a_{dynamic,i} = a_i - a_{static,i}, \quad (2)$$

where a_i is measured acceleration and i denotes three different directions, namely *X*, *Y* and *Z*.

2) Determine the frequency band of acceleration

As measured acceleration has a relatively broad frequency band, a coherence analysis between the AHRS-measured platform acceleration and the time derivative of ADCP-estimated water velocity (ADCP-derived acceleration) is applied to identify the frequency band where acceleration and velocity are in phase (Fig. 1.3). From Fig. 1.3b, the ADCP-derived acceleration and AHRS-measured acceleration have significant coherence from 0.1 Hz to nearly 1.2 Hz, which means that ADCP velocity estimate is strongly influenced by the instrument's motion in this frequency band. It is also important to mention that the decreasing of coherence between ADCP-derived velocity and AHRS-measured acceleration beyond 1.2 Hz does not necessarily indicate that measured velocity is no longer contaminated by the platform motion at the high-frequency region, since the decreased coherence primarily arises from the ADCP-derived acceleration

reaching its noise floor due to the uncertainty per ping characteristics of the ADCP (as shown in Fig. 1.3a).

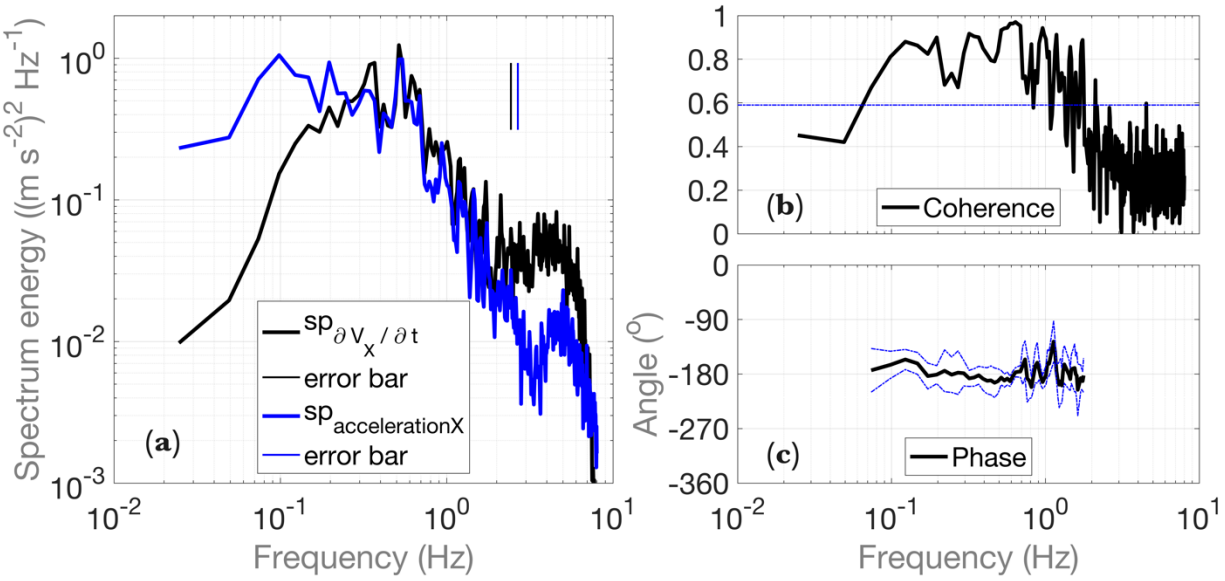

Figure 1.3 Coherence between $\partial V_x/\partial t$ and $acce_X$ from the AHRS. Velocity and acceleration data used in this example plot are from the same profile used throughout the rest of the paper from the MISOBOB 2019 cruise. V_x is the raw range-averaged X-ward velocity and the partial derivative is simply calculated by a first-order differentiation. The spectrum is given in (a), with estimated coherence in (b), and phase in (c). Note that phase is shown only where coherence is above the uncertainty level. Here, the velocity is quality-controlled by extracting data that have less than 50% correlation between the transmitted acoustic signal and received acoustic signal, and then range-averaged to obtain a time series for one Wirewalker profile. Spectra of velocity and acceleration are calculated by dividing the data into 646 points per group (about 12.5 m in depth) with 50% overlap and then applying a Hanning window. Dashed lines in (b) and (c) denote the uncertainty level.

3) Transfer acceleration to a fixed coordinate system

Since we aim to integrate the acceleration measurements forward to estimate the time-dependent platform motion, we first must establish a fixed coordinate system. The most convenient is Earth coordinates, East/North/Up. Otherwise, as the Wirewalker rotates in the water, the direction of x-y-z axes is constantly changing and integration of acceleration will be meaningless. For this transformation, Euler angles (pitch, roll, and heading), provided by the ADCP AHRS are

required. In matrix form, the transformation is (Nortek 2020, Guerra and Thomson 2017, Guerra 2021).

$$\begin{bmatrix} a_{ENU,E} \\ a_{ENU,N} \\ a_{ENU,U} \end{bmatrix} =$$

$$\begin{bmatrix} cos\psi cos\phi & -cos\psi sin\phi sin\theta + sin\psi cos\theta & -cos\psi sin\phi cos\theta - sin\psi sin\phi \\ -sin\psi cos\phi & sin\psi sin\phi sin\theta + cos\psi cos\theta & sin\psi sin\phi cos\theta - cos\psi sin\phi \\ sin\phi & cos\phi sin\theta & cos\phi cos\theta \end{bmatrix} \begin{bmatrix} a_{dynamic,X} \\ a_{dynamic,Y} \\ a_{dynamic,Z} \end{bmatrix}, (3)$$

Where θ is roll angle, ϕ is pitch angle, ψ is heading angle, $a_{dynamic,i}$ are dynamic accelerations in ADCP's XYZ axes, and $a_{ENU,j}$ are transferred accelerations, where j indicates three different components, namely, East-West, North-South, and Up-Down.

4) Bandpass acceleration

To perform the integration, it is advantageous to narrow the bandwidth of the acceleration estimates. Based on the coherence analysis (Fig. 1.3), the frequency band of 'Wirewalker motion-related' acceleration is estimated. Then, a_{ENU} are bandpassed using a first-order Butterworth filter with cutoff frequencies of 0.1 Hz and 1.2 Hz. After filtering, the mean of the acceleration data is removed.

5) Integrate acceleration in time

The Wirewalker translational velocities ($\mathbf{V}_{\text{translation}}$) are obtained by integrating filtered acceleration in time in the Earth coordinate system. The Wirewalker platform motion at each time can then be removed from each ADCP velocity estimate to yield a motion-corrected ADCP velocity product.

Down-looking ADCP configuration

When mounted on a surface buoy, ADCPs are often configured to collect bursts of time-continuous data at each sampled range, allowing for averages to be computed over minutes. In

such an average, the surface wave orbital velocity contribution is expected to be small, leaving the low-frequency current. A vertically moving vehicle, on the other hand, only dwells at any specific depth for a short time. A profiling Wirewalker might only spend 2-3 seconds within one 1 meter vertical bin. Thus a single-point measurement of velocity will only provide a few seconds of observations at any depth, precluding the ability to make an average where the contribution of the surface waves is small.

When fitted with an up- or down-looking ADCP, the “dwell time” within any 1 meter vertical bin becomes a function of both the Wirewalker's vertical speed and acoustic profiling range of the instrument. Since the Signature1000 has a ~20 m range, and the Wirewalker profiles at a vertical speed of ~0.5 m/s, we are able to collect time series of many tens of seconds within 1 m depth bins over an arbitrary depth range. These time series, containing dozens to hundreds of pings in each box, allow us to both lower measurement uncertainty through averaging, and to separate the surface wave orbital velocities and the background flow.

Below we present observations collected over the course of an Office of Naval Research funded campaign to the Bay of Bengal (the Monsoon Intraseasonal Oscillation - Bay of Bengal (MISO-BOB) Departmental Research Initiative). There, we fielded three drifting buoy systems. Developed in collaboration the Woods Hole Oceanographic Institution (WHOI), the Drogued Buoy Air-Sea Interaction System (D-BASIS) combines a WHOI air-sea flux buoy, a SIO Wirewalker profiler equipped with CTD, bio-optical and irradiance sensors, and a down-looking Nortek Signature1000 with AHRS. The D-BASIS is drogued at depth, where the flow is sluggish, and can be deployed on long-term drifts at a fraction of the cost of a traditional deep-sea mooring. The combination of research-quality air/sea fluxes and rapid profiles of the upper ocean with high vertical resolution allows for the physics of ocean boundary layer response to atmospheric forcing

to be elucidated in detail. Such observations are critical to improved forecasting of the ocean and atmosphere.

We show observations from a single D-BASIS system, MISO-3. The Nortek Signature1000 was configured to sample with 4 slanted beams at a 16 Hz rate, with a 0.25 m cell size, a 0.1 m blanking distance from the transducer, and at maximum transmit power. This combination yielded 87 cells (0.1 to 21.6 m range), sampled continuously over the course of the deployment. MISO-3 was deployed in the vicinity of 16º30'N, 84º$45'E on July 11, 2019 and recovered on July 28, 2019. The sea-state and winds were generally moderate over the course of the first half of the deployment. After mid-deployment, several calm, clear days were followed by a series of passing fronts and wind-speeds increasing to >10 m/s. The increase in winds during the second half of the deployment led to an elevated sea-state, with waves exceeding 2 meters in amplitude.

Data analysis procedures for fine-scale velocity measurements

The approach to the data analysis procedure is shown schematically in the flow chart in Fig. 1.4 (box I), with an equivalent velocity decomposition in Eq. 4. In Eq. 4, the observed velocity ($\mathbf{V}_{OBS}$) is composed of the ocean background velocity independent of surface wave orbital velocities ($\mathbf{V}_{INT}$), Wirewalker motion ($\mathbf{V}_{Wirewalker}$), residual surface wave orbital velocity ($\mathbf{V}_{SW}$), the drift velocity of the Wirewalker system ($\mathbf{V}_{Buoy}$), and noise ($\mathbf{V}_{Noise}$):

$$\mathbf{V}_{OBS} = \mathbf{V}_{INT} + \mathbf{V}_{Wirewalker} + \mathbf{V}_{SW} + \mathbf{V}_{Buoy} + \mathbf{V}_{Noise}. \quad (4)$$

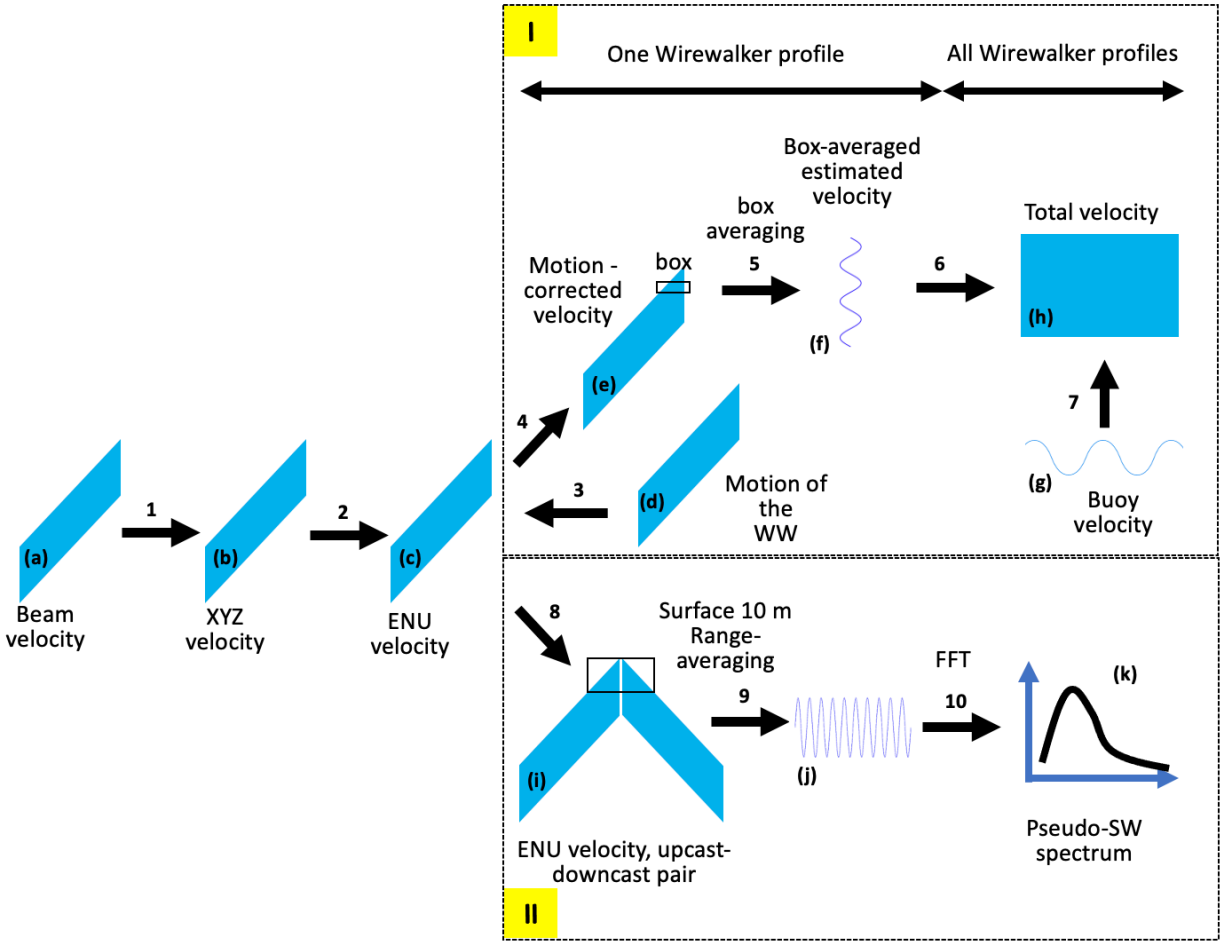

Figure 1.4 Schematic demonstrating the sequence of data processing using velocity data collected by a down-looking ADCP to obtain fine-scale low-frequency flows (I) and pseudo-surface wave velocity spectrum (II). The velocity product at each step is indicated by a letter while the associated data processing step is given by the number.

The step-by-step description of Fig. 1.4 is as follows:

a. Transform beam velocity to XYZ velocity, step 1 in Fig. 1.4 (box I)

The ADCP is configured to sample in beam coordinates, which requires transformation to a Cartesian (XYZ) coordinate system relative to the ADCP (and thus the Wirewalker). A convenient choice is a right-hand frame of reference with the positive X axis in the direction of the projection of Beam 1 on the transducer plane, positive Y axis in the direction of the projection

of Beam 4 on the transducer plane, and positive Z axis in the direction normal to the transducer plane.

The transfer matrix is (Nortek 2020, Guerra and Thomson 2017, Guerra 2021)

$$\begin{bmatrix} V_X \\ V_Y \\ V_Z \end{bmatrix} = \begin{bmatrix} \frac{1}{2sin\alpha} & 0 & -\frac{1}{2sin\alpha} & 0 \\ 0 & -\frac{1}{2sin\alpha} & 0 & \frac{1}{2sin\alpha} \\ \frac{1}{4cos\alpha} & \frac{1}{4cos\alpha} & \frac{1}{4cos\alpha} & \frac{1}{4cos\alpha} \end{bmatrix} \begin{bmatrix} V_{B1} \\ V_{B2} \\ V_{B3} \\ V_{B4} \end{bmatrix}, \quad (5)$$

where V_X, V_Y, and V_Z are *X, Y,* and *Z* velocities, V_{B1}, V_{B2}, V_{B3}, and V_{B4} are Beam velocities, and α is the beam angle (25 degrees for Signature1000). Sample XYZ velocity fields are shown in Fig. 1.5a-c.

b. Transform XYZ velocity to ENU velocity, step 2 in Fig. 1.4 (box I)

XYZ coordinate system is relative to the ADCP, which is a moving object. To study velocity data free from platform's movement, we require a fixed coordinate system (e.g., "Earth" coordinates). Therefore, XYZ velocities are further transformed into ENU velocities following Eq. 3. Sample ENU velocity plots are shown in Fig. 1.5d-f.

c. Extract Wirewalker motion from velocity measurement, step 3/4 in Fig. 1.4 (box I)

To show the relationship between the strong, oscillating velocity signal and platform motion, we compare the range-averaged raw ENU velocity at each time and the Wirewalker translational motion, $\mathbf{V}_{\text{translation}}$, calculated above (step 5 in section 2) in Fig. 1.6. During a typical upcast, the angular rate of rotation ranges from 1 °/s at the bottom of these profiles (100 m), where the influence of the surface wave field is small, to 10 °/s at the surface (Fig. 1.2c). The rotational velocity ranges from 0.0175 m/s to 0.1745 m/s, while the translational velocity can reach up to 1.8 m/s (blue lines in Fig. 1.6). Since the rotational velocity is relatively small, we have neglected this component. In what follows, $\mathbf{V}_{\text{Wirewalker}} = \mathbf{V}_{\text{translation}}$. The implications of this assumption are revisited in the Discussion.

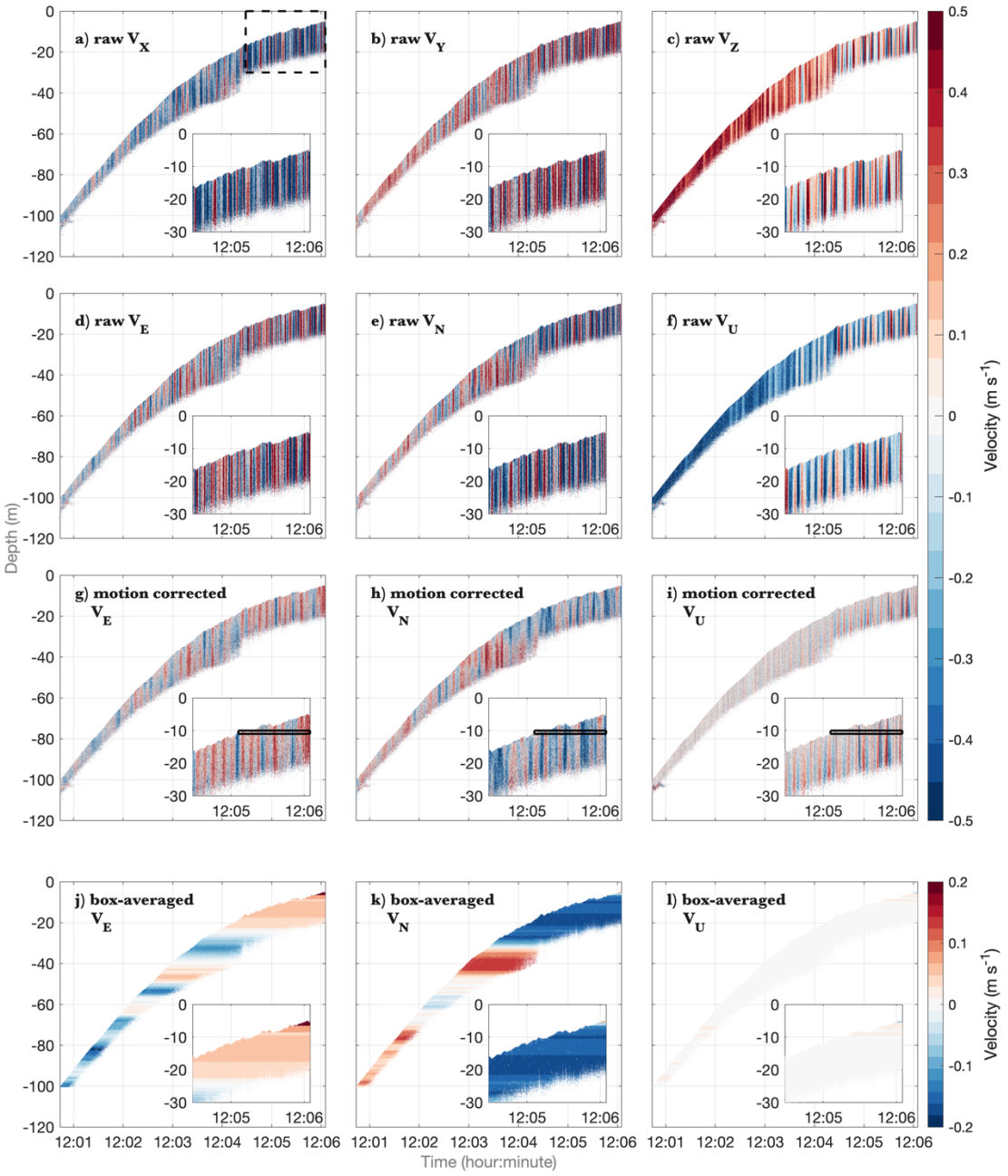

Figure 1.5 Velocity plots showing different processing stages for one Wirewalker profile. (a), (b) and (c) are XYZ velocities for X direction, Y direction, and Z direction respectively. (d), (e) and (f) are ENU velocities for East-West, North-South, and Up-Down direction respectively. (g), (h) and (i) are motion-corrected velocities for East-West, North-South, and Up-Down direction respectively. (j), (k) and (i) are box-averaged velocities for East-West, North-South, and Up-Down direction respectively. The second axis in each panel is the zoomed-in view of the data in the same dashed box shown in (a). Also, the black box in the second axis of (g), (h), and (i) represents the `1-m box' for box-averaging.

From Fig. 1.6, we see that the raw XYZ and ENU velocity are significantly correlated with the Wirewalker motion. The averaged coherence for the East-West velocity is 0.97 between 0.1 Hz and 1.2 Hz at a phase around 0 degrees; similarly, the averaged coherence for North-South velocity is 0.96 at a phase around 0 degrees. This coherence occurs at each measurement range, as would be expected if it arose from translation of the measurement platform.

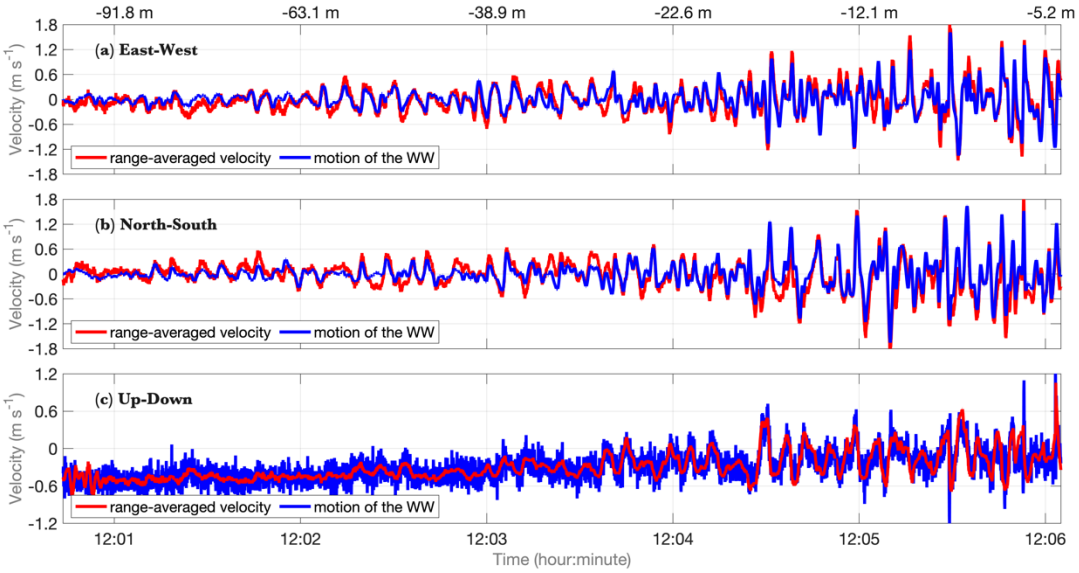

Figure 1.6 Range-averaged raw ENU velocity and Wirewalker motion velocity for one Wirewalker profile. Here, Wirewalker motion velocity has been multiplied by -1 for a clear comparison. Note that for the vertical component, Wirewalker motion is simply calculated by time differentiation of measured pressure (dp/dt), as this is a more direct measurement of vertical motion instead of integration of z component acceleration. The second axis on the top represents the vertical location of the Wirewalker at the corresponding time.

For each velocity component, the motion of the Wirewalker agrees well, but not perfectly, with the range-averaged raw ENU velocity. This shows that the Wirewalker motion estimation from the AHRS is effective and that the 'vertical stripes' in the raw velocity data are correlated with platform motion. Motion-corrected velocity profiles are shown in Fig. 1.5g-i.

d. Box averaging technique, step 5 in Fig. 1.4 (box I)

Due to the vertical profiling of the Wirewalker, the z position of each velocity measurement in time changes, producing a sliding window with a length determined by the profiling range of the ADCP, and where the dwell-time at any depth is a function of the ADCP's range and the vertical speed of the platform. This "dwell" duration can be approximated by $T = R/V_{Wirewalker,z}$, where R is the profiling range of the ADCP and $V_{Wirewalker,z}$ is the Wirewalker vertical speed.

In order to produce a profile of ocean velocities over the length of each Wirewalker profile, we utilize a "box-averaging" approach, where time-series of velocity are produced for a particular depth bin width from the motion-corrected velocities. These "time-series" within each depth bin can be produced with duration of several to many surface wave periods (tens of seconds to minutes), and can be averaged in time to reduce the contribution for the residual surface wave field to the velocity estimate within each depth bin:

$$\mathbf{V}_{box-average}(z_i) = \frac{1}{N_i}\sum_{n=1}^{N_i} \mathbf{V}_{\mathrm{mc}}(\hat{z}_n, t_n), \tag{6}$$

where $\mathbf{V}_{\mathrm{mc}}$ is motion-corrected velocity, i represents each depth bin, N_i is the total number of velocity measurements in each depth bin, and subscript n denotes each velocity measurement in each bin. The bin width in the vertical is inversely related to the precision of the resulting velocity estimate since a larger bin includes more individual measurements.

The effect of each processing step outlined above can be seen in comparison of the time-series for selected depth bins (Fig. 1.7b-e). Spikes in the raw data associated with vehicle's motion are effectively reduced by the motion correction. The number of measurement samples within a 1-m vertical bin is depth-dependent, increasing from 1000 to 6000 from 100 m depth to 20 m depth, where the maximum acoustic scattering is found for this particular profile. Thereafter, the number

of samples gradually decreases as the Wirewalker approaches the surface. At a minimum of 1000 samples, time-series of about 20 seconds are produced in each depth "box".

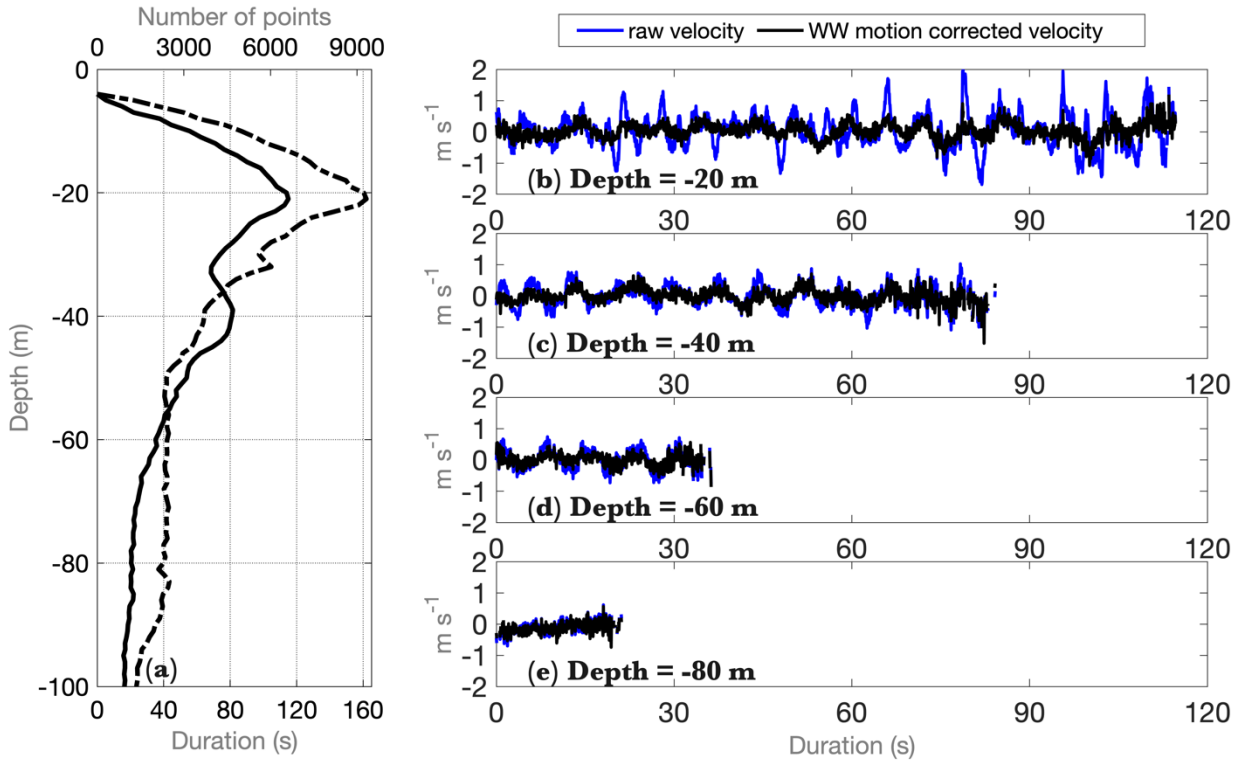

Figure 1.7 (a) Dwell duration (bottom x axis) and the number of independent velocity measurements (top x axis) sampled for each 1-m box. The solid black line corresponds to the same profile used throughout the paper characterized by weak acoustic scattering strength and the dash-dotted black line is obtained from another profile with strong acoustic scattering strength. (b), (c), (d), and (e) show the depth-averaged Eastward velocities in the 1-m box at four different depths (marked by dotted horizontal lines in (a)) of two velocity products, corresponding to the solid black line in (a).

Fig. 1.8 shows the frequency spectrum of the time series inside each box for raw and motion-corrected Eastward velocity and motion-corrected velocity using a 1-m vertical bin. Besides the noticeable energy decrease induced by the motion correction until 1-2 Hz where noise starts to dominate, these spectra show that the surface wave time-scales are still energetic even after motion correction, as indicated by the energy peaks in the 0.1 Hz - 0.2 Hz frequency band (thick black lines in Fig. 1.8a-d).

To provide a quantitative assessment of the trade-off between the vertical spacing of the resulting velocity estimate and the precision of the estimate within each bin, we compute the vertical wavenumber spectrum using the vertical profiles of the horizontal velocity obtained for various box sizes. Results (not shown here) show that spectrum with varying box sizes have almost the same shape and noise starts to dominate beyond 0.33 cpm (an example is shown in Fig. 1.10). Therefore, we use a vertical bin width of 1 m in what follows.

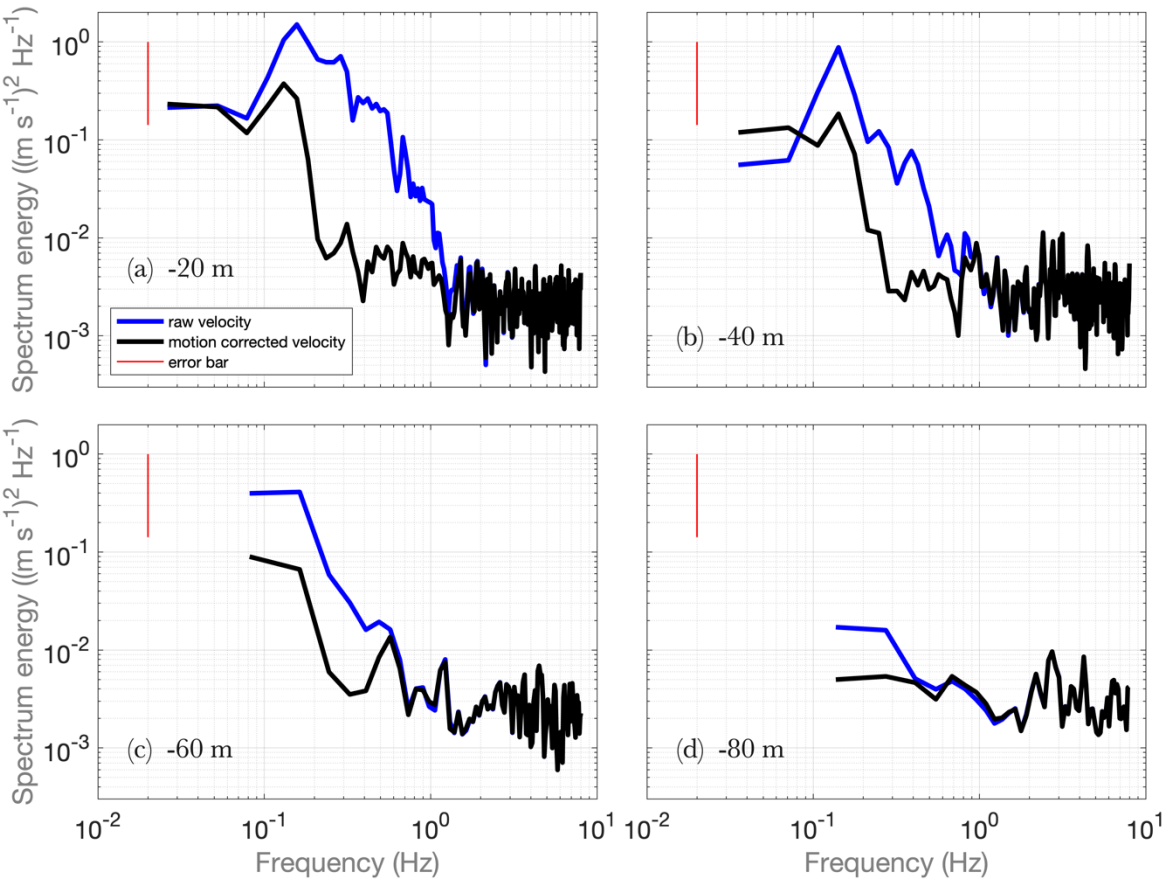

Figure 1.8 Spectrum results of the time series inside the 1-m box for four different depths of two velocity products [corresponding to (b)-(e) in Fig. 1.7].

e. Total velocity field, step 6/7 in Fig. 1.4 (box I)

The total reconstructed velocity field comes from the sum of the reconstructed box-averaged velocity, which is depth-dependent, and the buoy drift velocity, which is depth-uniform. The total velocity field is shown in Fig. 1.9a/c for the MISO-3 deployment.

We estimate the precision of the total velocity field by calculating the standard error of the mean (SEM, the standard deviation of the mean of multiple sample means). It is expressed as:

$$SEM(i) = \frac{\sigma_i}{\sqrt{N_i}}, \tag{7}$$

where i represents boxes at different depths, σ is the standard deviation of the time series of depth-averaged motion corrected velocity in each box, and N is the number of the independent ADCP pings in each box. The SEM value ranges between 0.006 m/s, where N is large, to 0.01 m/s, where N is small, such as the bottom and surface region of the Wirewalker profile.

Discussion

a. Fine-scale velocity measurements from the Wirewalker profiler

The motion correction implemented here would provide an improved knowledge of buoy or mooring motion relative to previous systems that did not carry AHRS measurements, and so could be used to improve velocity precision from ADCPs fixed on buoys or moorings. However, velocity measurements made from a fixed depth come with the implicit trade-off between the range of depths that can be covered and the resolution in the vertical that can be achieved. Many applications require knowledge of finer vertical scales than can be achieved from a fixed ADCP over ranges where that variability must be known. For example, the wind can trigger a near-inertial response in the ocean that transports energy from the atmosphere into the ocean interior. Because of the physics of this response, the near-inertial internal wave that affects this transport has a small vertical wavelength, typically with a maximum energy at a vertical wavenumber cutoff of 0.1 cpm or higher (Pinkel 1983; Pinkel and Anderson 1997). Fixed or commercial shipboard ADCPs with

vertical ranges of >100 m struggle to achieve the necessary vertical resolution. Those with ranges of several hundred meters or more are typically lower frequency and have less vertical resolution, often missing this important signal entirely.

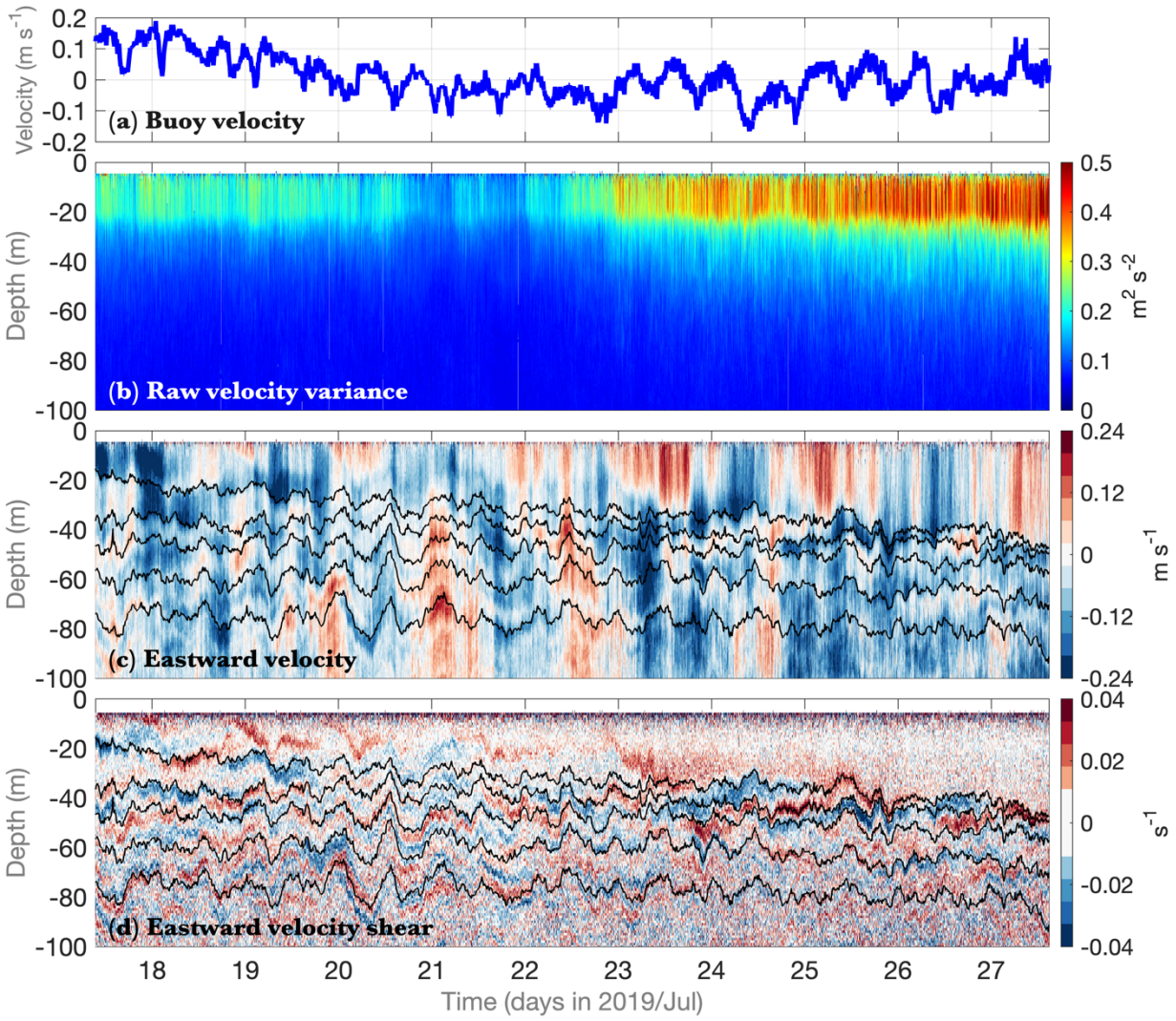

Figure 1.9 (a) The buoy drifting velocity. (b)The velocity variance inside each 1-m box using raw Eastward velocity. (c) The Eastward velocity estimated after motion correction and box averaging. (d) The Eastward velocity shear, which is calculated from vertical differentiation of velocity in (c). The vertical resolution is 1 m. The time resolution is not uniform but has an average resolution of 5 minutes per profile. The total duration of this measurement is 16.8 days, but about 10 days of data are shown here. Black lines in (b) and (c) are isopycnals with values from 1020.7 kg/m^3 to 1023.9 kg/m^3 with a 0.8 kg/m^3 interval.

At some trade-off in time resolution, a short-range, high frequency ADCP can be moved vertically through the ocean to provide highly vertically resolved velocities over large depth ranges. This has been accomplished with buoyancy gliders (Todd et al. 2017) and Lagrangian floats (Shcherbina et al. 2018). However, those platforms can only determine their path-mean velocity based on GPS fixes during surfacing -- which, in the case of a typical glider mission, might be only once every 6 hours. Here, we add to that technical capacity by demonstrating that a similar approach can also be implemented for the Wirewalker ocean wave-powered profiler. Velocity with high vertical resolution relative to the drifting profiler is combined with the drift velocity calculated from continuously tracked surface buoy to reconstruct the full velocity field over the profiling ranges on time-scales of minutes.

The presence of a surface buoy comes with other trade-offs. Surface orbital wave-induced horizontal displacements of the buoy are transmitted to the profiling vehicle via the tensioned profiling wire. In general, these "buoy-motion" displacements of the vehicle are different from the *in situ* wave orbital velocities, which decay exponentially with depth. Removal of this motion by the onboard accelerometer and gyroscope leads to a motion corrected time-series of velocity ($\mathbf{V}_{\mathrm{mc}}$) that is composed of wave-orbital and background velocities ($\mathbf{V}_{\mathrm{mc}} = \mathbf{V}_{\boldsymbol{SW}} + \mathbf{V}_{\boldsymbol{INT}}$). The time-average $<\mathbf{V}_{\mathrm{mc}}>$ is approximately equal to $<\mathbf{V}_{\boldsymbol{INT}}>$ since $<\mathbf{V}_{\boldsymbol{SW}}> \rightarrow 0$ as the time over which the average is made extends to many surface wave periods. At depths and times where surface waves induce strong orbital velocities, the dwell time must be several tens of seconds at least to effectively separate the orbital velocities from the background flow.

The dwell time at any depth is a function of the vertical speed of the Wirewalker and the realized range of the ADCP. In regions or times where the acoustic scattering strength is weak (e.g., at 80 m depth for the solid black line in Fig. 1.7a), the realized range of the ADCP may drop

by more than half of its total average. When the ADCP's realized range is at a minimum, the dwell time can be reduced to 30 seconds or less, complicating efforts to separate the orbital from the background velocities. In the data presented here, minimum scattering strength was found below 80 m, and varied in time with the migration of the deep scattering layer (comparison between the solid black line and the dash-dotted black line in Fig. 1.7a). The scattering conditions will vary from region to region, and from open to coastal oceans, depending on the biological activity. In general, scattering is weakest at depths below 100 m, where orbital velocities are weak for most wave and swell conditions. Further improvement over the time averaging approach used here might also be achieved with a model based on surface wave physics and constrained by the Wirewalker velocity observations, in order to yield an improved separation of the wave orbital velocities. There are of course other reasons why a more sophisticated approach might be useful, including the characterization of the directional wave spectrum.

Our approach to obtain ocean velocity (i.e., $\mathbf{V}_{INT}$) can be assessed with a test case: what is the effective vertical resolution of the reconstructed velocity shear profiles (d/dz velocity)? Velocity shear for an open ocean, drifting Wirewalker deployment in the Bay of Bengal is shown in Fig. 1.9d, along with the depth of selected isopycnals estimated from onboard CTD observations. In the figure, velocities are estimated over 1 m vertical bins (0.5 cpm vertical wavenumber Nyquist frequency) over the 100 m profiling range of the Wirewalker.

The qualitative correspondence between the time evolution of the isopycnals and the time evolution of the bands of vertical shear in Fig. 1.9 is consistent with our expectation that the high-mode shear of near-inertial waves is displaced vertically by passing internal waves just as density surfaces are (e.g., Alford et al. 2016; Le Boyer et al. 2020). As in Fig. 1.10, both the vertical wavenumber spectrum of horizontal velocity and vertical shear show slopes that are in agreement

with internal wave theory, k^{-3} and k^{-1}, respectively (e.g., Duda and Cox 1989). Our observations are capable of resolving the ocean shear field down to a cut-off wavenumber of 0.33 cpm, at which point the variance of the ocean signal is smaller than the precision of the velocity observations and the spectrum becomes white (Fig. 1.10b).

In order to provide a point of comparison, velocity observations collected from R/V Sally Ride's RDI 300 kHz ADCP during the same time period within 100 km of the drifting Wirewalker were analyzed (black line in Fig. 1.10). This direct comparison shows the improvement in vertical resolution relative to the ship-board ADCP, which is barely capable of resolving the vertical wavenumber shear maximum at roughly 10 m scales. This is probably principally due to ship motion. Since most of the shear variance in the Wirewalker time-series exists at roughly 0.06 cpm, and a profile was collected over the entire 100 m every 5 minutes, the Wirewalker observations are capable of providing a robust and well-resolved picture of the vertical structure and time-evolution of near-inertial wave-induced shear from days to minutes in a way that shipboard measurement cannot. It is thought that these high vertical wavenumber fluctuations drive much of the turbulence and mixing in the ocean interior.

There are limitations to this approach for measuring the ocean fine-scale velocity variability, and several sampling strategies can be explored. For example, ADCP frequency, cell size, sampling bandwidth, and profiler speed, as well as practical considerations like memory and power limitations, all can be optimized based on the desired resolution in the vertical and the expected surface wave state.

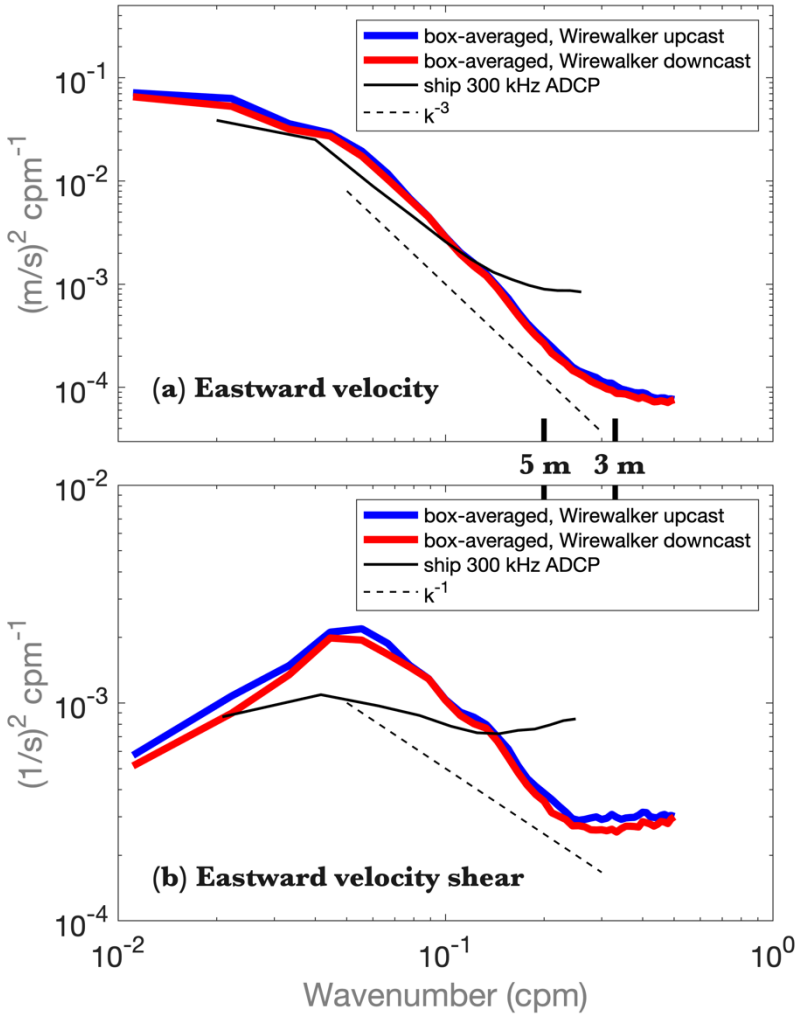

Figure 1.10 (a) The vertical wavenumber spectrum for horizontal velocities with the dashed line showing the k^{-3} slope. (b) The vertical wavenumber spectrum for estimated horizontal velocity shear, with the dashed line showing the k^{-1} slope. Ship ADCP data were collected by a 300 kHz RDI ADCP mounted on the bottom of the ship. Wirewalker spectrum is averaged across available 2294 profiles with a depth range from 6 m to 100 m. While ship ADCP spectrum is averaged across 18339 pings with a depth range from 10 m to 60 m. Texts in between these two panels show wavelength values corresponding to wavenumbers.

Furthermore, one of the major assumptions applied here is that the Wirewalker's rotational motion is neglected. However, under certain conditions, the rotational motion could become important and should be included in the motion calculation. This correction is left for future work.

b. Surface wave orbital velocities and ocean mixed layer velocities from the Wirewalker Profiler

To show the potential of the WW/ADCP combination to quantify surface waves (see schematics in Fig. 1.4 box II), we calculate a range-averaged velocity at each time from the Wirewalker velocities before motion correction. This time-series is examined over the upper ten meters of the water column during the ascent and subsequent descent of each profile. Frequency spectra can be calculated for each profile over the entire surface wave band (Fig. 1.11) The time-average of 3 weeks of these profiles shows the domain of spectral power in the wind-wave band (between 5-10 sec period, Fig. 1.11a). The variance over the surface-wave band can be estimated as the integral of the frequency spectra from 2-20 sec period, and is presented as a time-series in Fig. 1.11b. Since the average spectrum is dominated by the wind-wave band, it is not surprising to see the close correspondence of wave-band variance and the wind speed measured by a meteorological package on the surface buoy.

Ultimately, these data could be used with array approaches to estimate important aspects of the surface wave field, like its directional spectrum. When combined with displacement of the surface buoy, this would create a profiling system that could also work as a wave buoy. Likewise, detailed information regarding the surface wave field could be input into physics-based models to more effectively extract the orbital velocities from the ocean currents being measured. Hybrid data/model extraction of the surface wave orbital velocity signal might allow precise enough measurements to observe subtle dynamics like wave-induced Stokes drift, Langmuir circulations, and other important processes in the upper ocean and ocean mixed layer.

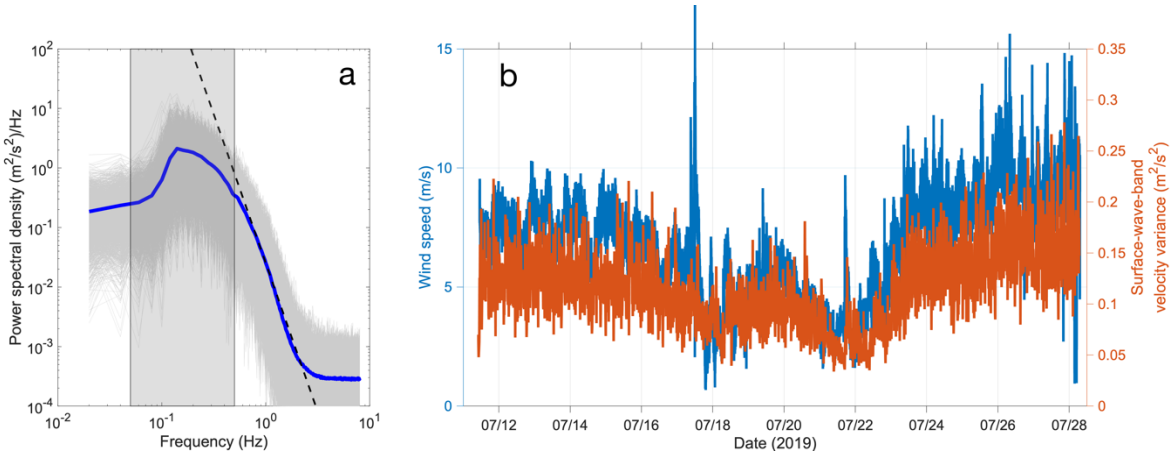

Figure 1.11 Surface wave orbital velocities measured from the Wirewalker platform. (a) Average (blue line) and individual frequency spectra (gray lines) from transducer depths < 10 m (2245 profiles). A dashed line corresponding to f^{-5} is shown for reference. (b) A comparison of the variance in the surface wave band and the collocated wind-speed measured from a WHOI meteorological system installed on the surface buoy.

Conclusion

We present an algorithm to obtain ocean velocities from a vertical profiling vehicle below a surface buoy. The methodology requires a up- or down-looking high frequency ADCP and a concurrent estimate of platform motion in 3 dimensions and time. Using a test case, we show that a Nortek Signature1000 with AHRS, configured to sample at 16 Hz over a range of ~20 m, mounted on a Wirewalker profiler moving vertically at 0.3 to 0.5 m/s is capable of producing velocity estimates that can characterize the ocean fine-scale velocity field to vertical wavenumbers of 1/3 cycles per meter, over a 100 m vertical range, every few minutes. The MATLAB code for this algorithm, along with raw velocity data collected from one Wirewalker upcast, can be found in the Supplemental Material.

The primary challenge is that, unlike a Lagrangian float, the design of the Wirewalker is such that it is in a quasi-Eulerian frame of reference relative to surface waves. Due to this fact,

even after motion-correction, the velocity measured at a single point still has a surface wave signature.

With a vertical profiling “window”, where simultaneous measurements of velocity are collected across a range of depths from a vertically moving platform, a motion-corrected up- or down-looking ADCP alleviates this problem, giving time aperture at all depths. This allows the surface wave orbital velocities and the background flow to be separated. The technique reported here builds on previous efforts to measure velocities from autonomous platforms and by ships using “lowered ADCP” techniques. Improvement of ocean velocity estimation from autonomous platforms of all kinds is a crucial observational tool for understanding and predicting the physical state of the ocean.

Chapter 1, in full, is a reprint of the material as it appears in: Zheng, B., Lucas, A.J., Pinkel, R., Le Boyer, A. (2022). Fine-Scale Velocity Measurement on the Wirewalker Wave-Powered Profiler. *Journal of Atmospheric and Oceanic Technology*, 39(2), 133–147. The dissertation author was the primary investigator and author of this paper.

CHAPTER 2 DINOFLAGELLATE VERTICAL MIGRATION FUELS AN INTENSE RED TIDE

Abstract

Harmful algal blooms (HABs) are globally increasing economic, health, and ecosystem threats. In spite of the relatively frequent occurrence of HABs, the mechanisms responsible for their initiation and exceptional abundance remain imperfectly understood. A 50-year-old hypothesis posits that dense dinoflagellate blooms derive from motility: swimming upward during the day to photosynthesize and downward at night to access the deep nutrient pool. This allows dinoflagellates to outgrow their nonmotile competitors. We tested this hypothesis using *in situ* data from an autonomous, ocean-wave-powered vertical profiling system. We showed that the dinoflagellate *Lingulodinium polyedra*'s vertical migration led to depletion of the deep nitrate pool during a 2020 red tide HAB event. Downward migration began at dusk, with the maximum migration depth determined by local nitrate concentrations. Losses of nitrate at depth were balanced by proportional increases in phytoplankton chlorophyll concentrations and suspended particle load, conclusively linking vertical migration to the access and assimilation of deep nitrate in the ocean environment. Vertical migration during the red tide created distinctly anomalous biogeochemical conditions compared to 70 years of climatological data, demonstrating the capacity of these events to temporarily reshape the coastal ocean's ecosystem and biogeochemistry. Advances in the understanding of the physiological, behavioral, and metabolic dynamics of HAB-forming organisms from cutting-edge observational techniques will improve our ability to forecast HABs and mitigate their consequences in the future.

Significance statement

Extremely dense harmful algal blooms (HABs) are an increasing problem globally. How microscopic, single-celled organisms can reach such high abundances is still poorly understood.

Over 50 years ago it was postulated that HABs formed by daily vertical migrations of motile organisms allowed them to out-compete non-motile species for light and nutrients. We tested this hypothesis using innovative *in situ* observations during a dense bloom. The organisms swam downward at night into the deep nutrient pool, and upward during the day to photosynthesize. Decreases of nutrients in deep waters were proportional to increases in organism abundance, directly linking organism behavioral and metabolic activities. Our data support the hypothesis that vertical migration behavior is central to forming extreme abundances during HABs.

Introduction

Harmful algal blooms (HABs) are a global problem, impacting human health, ecosystem function, and water quality. HAB outbreaks are estimated to cost tens of millions of dollars annually in the United States alone (Ritzman et al. 2018; Anderson et al. 2021). Major strides have been made in elucidating the biochemical pathways for toxin production; developing monitoring, tracking, and response strategies in key locations; and improving modeling capacity (Franks 2018; Brunson et al. 2018; Ralston and Moore 2020). However, the biotic and abiotic factors that lead to extreme biomass density of HABs are not yet fully understood, complicating efforts to forecast their occurrence and impact (Anderson et al. 2012, 2015; Kenitz et al. 2023).

Dinoflagellate blooms often occur during strongly stratified ocean conditions (Spilling et al. 2018). Nutrient concentrations in the upper, relatively warm, sunlit waters become depleted through uptake by the phytoplankton community. These upper waters are separated from the deeper, cold, dark, and nutrient-rich waters by a strong density gradient that inhibits the upward physical transport of nutrients. Many HAB-forming dinoflagellate species -- like *Lingulodinium polyedra* (or formerly *Lingulodinium polyedrum; Gonyaulax polyedra*) -- are active swimmers (Lewis and Hallett 1997; Berdalet et al. 2014; Jeong et al. 2015). Early field and laboratory

observations documented dinoflagellate diel vertical migrations (DVMs) in which organisms accumulated near the surface during daylight hours and swam to depth at night (Hasle 1950; Kamykowski and Zentara 1977; Heaney and Eppley 1981). Based on observational evidence provided by Holmes et al. (1967), Eppley et al. (1968) were the first to hypothesize that this migration behavior allowed dinoflagellates to form dense blooms by gaining access to light at the surface during the day, and nutrients, especially nitrogen, at depth during the night -- a singular competitive advantage over stationary photoautotrophic organisms during periods of strong, vertical stratification.

In the 50 years since Eppley et al. (1968) was published, laboratory experiments have supported the DVM-bloom hypothesis, demonstrating that dinoflagellates can vertically migrate and that their migrations depend on light, nutrient distributions, stratification, and turbulence (Eppley et al. 1968; Kamykowski 1981; Peacock and Kudela 2014; Sengupta et al. 2017). However, despite extensive laboratory research, the DVM-bloom hypothesis has never been conclusively tested in the field.

Field confirmation of the DVM-bloom hypothesis requires evidence that the dinoflagellates vertically migrate, that the dinoflagellates take up nutrients from below the euphotic zone during this migration, and that dinoflagellate abundances increase in proportion to the nutrient uptake. The lack of conclusive field evidence of the DVM-bloom hypothesis is primarily due to two impediments: 1) the need for concurrent *in situ* measurements of biological, physical, nutrient, and light conditions, and 2) the requirement for those data to be collected with adequate resolution in time and space to separate variability due to physical forcings (e.g., currents, internal waves) from variability mediated by biological processes. Here, we use data acquired by

an autonomous profiler to provide field evidence testing -- and supporting -- the DVM-bloom hypothesis (Eppley et al. 1968).

Blooms of the dinoflagellate *L. polyedra* have been fairly common in the Southern California Bight (SCB) for at least 120 years, often growing to cell density high enough to change the color of the water during the day (hence the term "red tide") and generate spectacular bioluminescence at night (Torrey 1902; Allen 1938, 1941, 1943, 1946). An unusually intense *L. polyedra* red tide in the SCB in the spring of 2020 (Fig. 2.1a) lasted from early April to late May, and covered the entire SCB and most of coastal northern Baja California waters. At its peak, the bloom reached nine million cells per liter at the Scripps Institution of Oceanography (SIO) Pier, with a chlorophyll-a (Chl-a) concentration there of 897 mg m^{-3} on April 27 (Kahru et al. 2021). These are the highest values of Chl-a ever measured at Scripps Pier in nearly 40 years of monitoring, and represent roughly three orders of magnitude higher Chl-a than the average value found in the region (Kahru et al. 2021).

Satellite-detected Chl-a concentrations were >50 mg m^{-3} (>50 times pre-bloom values) in early May (Fig. 2.1a), and near-surface images collected by an Imaging FlowCytobot (IFCB, see Methods) at the Del Mar (DM) mooring (see Fig. 2.1b) showed that *L. polyedra* was the most abundant microbe in the sampled size range. During this time Scripps Pier *L. polyedra* cell counts regularly exceeded 1 million cells per liter, with near-surface Chl-a concentrations more than 90 mg m^{-3} (Kahru et al. 2021). The decay of the bloom in early May led to local anoxia and extensive fish and crustacean mortality in the region.

Depth-time-resolved measurements during the red tide

To investigate the interplay of biogeochemical patterns, organismal behavior, and physical dynamics during the *L. polyedra* bloom, we deployed a Wirewalker (WW) ocean-wave-powered

profiling autonomous mooring adjacent to the DM mooring, ~4 km offshore coastal San Diego (Fig. 2.1a, Methods, Pinkel et al. 2011; Lucas et al. 2017). The WW payload consisted of an integrated suite of sensors to simultaneously measure *in situ* nitrate, multi-spectral irradiance, bio-optical water properties, and hydrographic properties. The WW mooring yielded full-depth (100 m) profiles of light, nitrate concentration, Chl-a fluorescence, optical backscatter, temperature, salinity, and density at 1 m vertical resolution every 15 mins for a period of three weeks (Methods). These observations allowed us to quantify the relationships between dinoflagellate vertical migration, light, and nitrate concentration. Our analyses revealed the cyclic downward vertical migration of dinoflagellates at night, coincident with the loss of nitrate at depth, and proportional increases in the vertically integrated Chl-a and turbidity of the bloom. Toward the end of our data record, the deep nitrate pool was so depleted that the dinoflagellate became less apparent, and the bloom began to dissipate.

The 2020 bloom event began during unusual conditions in Southern California coastal waters. Anomalous rainfall in March and April was followed by a prolonged sunny and calm period through mid-May -- an uncommon springtime combination (*SI Appendix*, Fig. 2.S1). The resulting co-occurrence of record heating and intense freshwater input led to record-high sea surface temperatures (>26°C, data not shown, https://cdip.ucsd.edu/), and strong subsurface stratification (Fig. 2.1 cd) -- conditions that are known to favor dinoflagellate bloom initiation (Smayda 2002; Spilling et al. 2018).

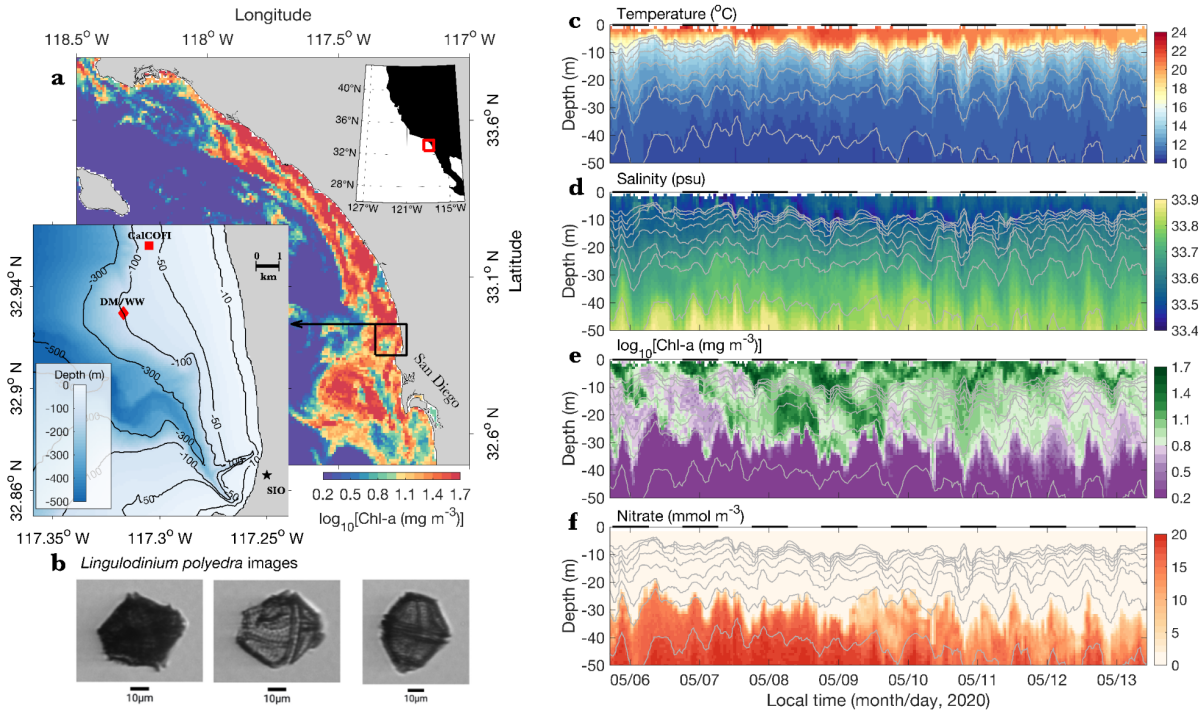

Figure 2.1 a) Visible Infrared Imaging Radiometer Suite (VIIRS) - Suomi National Polar-Orbiting Partnership (NPP) 1-day composite satellite chlorophyll-a (Chl-a) image at Southern California Bight (SCB, corresponding to the red box in the upper right inset panel) on May 6, 2020. The lower left inset panel shows the zoom-in bathymetric map of the study area (corresponding to the black box in the main panel), with the Del Mar mooring (DM) and the Wirewalker (WW) location marked by the red diamond on the 100 m isobath, and the California Cooperative Oceanic Fisheries Investigations (CalCOFI) station (Line: 93.3, Station: 26.7) marked by the red square. b) Images of *Lingulodinium polyedra* captured by the Imaging FlowCytobot (IFCB) on the DM on May 7, 2020. c–f) WW-measured temperature, salinity, Chl-a concentration, and nitrate concentration respectively, with isopycnals contoured as gray lines, ranging from 1024.35 kg m^{-3} to 1025.75 kg m^{-3}, with an increment of 0.2 kg m^{-3}. Black bars on the upper boundary of each panel indicate nighttime. Note that only 50 m depth and 7 days of data from the full record are shown here.

Vertical migration of dinoflagellates

In the WW time series, periodically elevated Chl-a concentrations were observed down to ca. 30-40 m depth, tens of meters deeper than the measured euphotic zone (Fig. 2.2, Fig. 2.S3), with patches of high Chl-a moving vertically across isopycnal surfaces with a near-daily rhythm (Fig. 2.1e). A daily rhythm was also apparent in the near-surface IFCB *L. polyedra* cell counts, directly linking the Chl-a Wirewalker measurements with *L. polyedra* abundance (Fig. 2.2a). Over

a week, nitrate became depleted at depth where Chl-a concentrations were high, leading to the nitracline deepening by more than 10 m (Fig. 2.1f) -- an abnormal situation for these coastal waters (see below; Lucas et al. 2011).

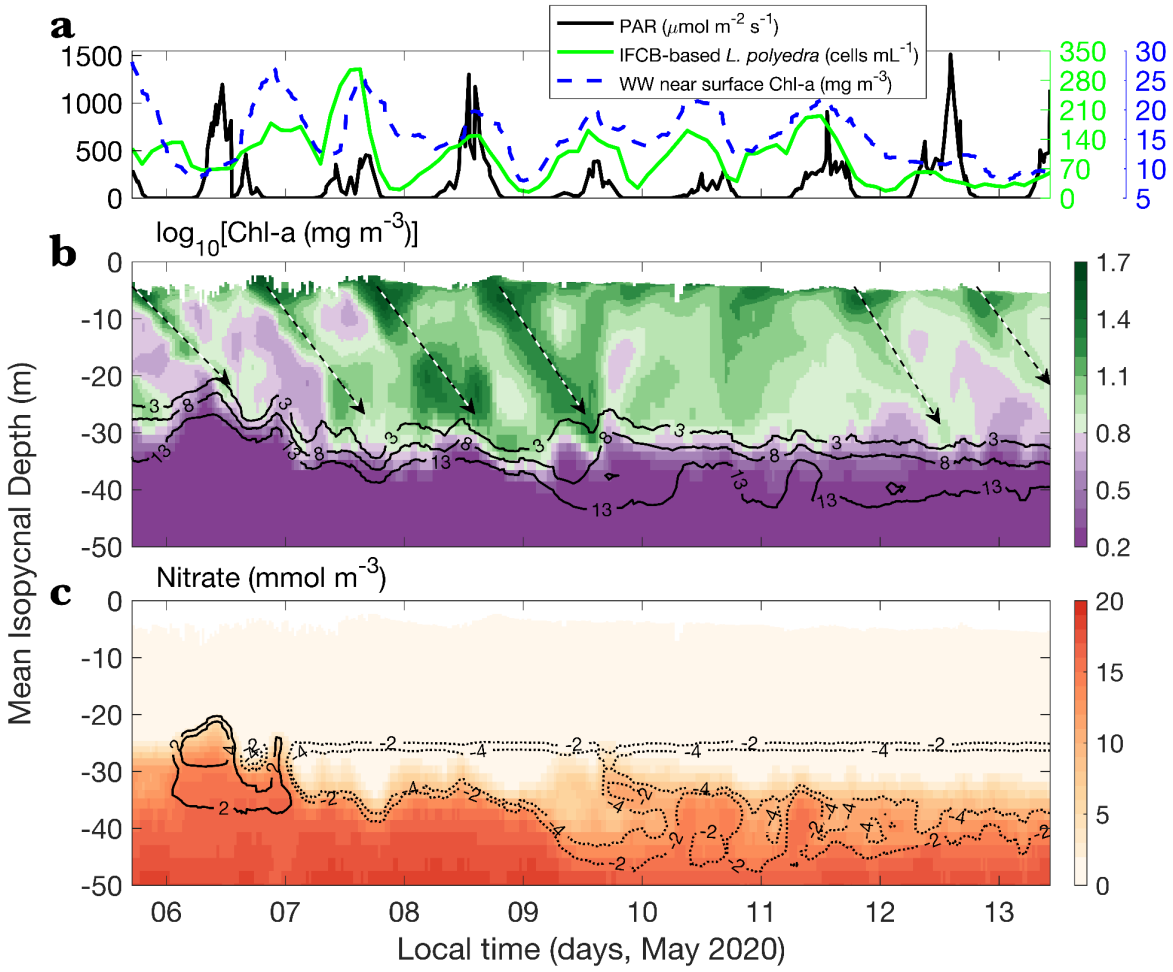

Figure 2.2 Biogeochemical observations. a) left y axis: near-surface photosynthetically available radiation (PAR) estimated from the subsurface irradiance measurements on the WW profiler at 2 m depth. Right y axis: IFCB-based *Lingulodinium polyedra* cell concentration and WW-measured near-surface chlorophyll concentration, respectively. b) and c) along-isopycnal Chl-a, and nitrate concentration from the WW, respectively. The black contours in b are iso-nitrate lines with values of 3 mmol m^{-3}, 8 mmol m^{-3}, and 13 mmol m^{-3} respectively, and the black-white arrows represent the migration paths. The contours in c are nitrate anomalies referenced to the first profile during this period, with positive anomalies in black solid lines and negative anomalies in black dotted lines. Note that the x-axis here is the local time, and the y-axis is the mean depth for each isopycnal (see *SI Appendix*, section 5).

Vertical motions from internal waves (IWs) -- waves analogous to surface waves, but propagating along density surfaces in the ocean interior -- caused ~20 m vertical fluctuations (peak-to-trough amplitude) of the Chl-a, nitrate, and density distributions (Fig. 2.1 c-f). Plotting the data in an isopycnal vertical coordinate removes these vertical motions (Fig. 2.2, *SI Appendix*, section 5). Hereinafter, all data are mapped onto isopycnals and plotted against the mean depths of the isopycnals as the vertical coordinate (*SI Appendix*, section 5). This transformation makes it clear that coherent patches of high Chl-a moved downward from the surface, across isopycnals, to >30 m depth with a ~daily periodicity (Fig. 2.2b). This descent of Chl-a was the most obvious when PAR was relatively high (Fig. 2.2ab). Given the dominance of Chl-a by *L. polyedra* during the bloom and the clear in-phase correspondence between IFCB-based *L. polyedra* cell concentration and WW-measured Chl-a (Fig. 2.2a), these Chl-a patches were likely layers of *L. polyedra* migrating vertically.

The *L. polyedra* migration pattern began with the organisms starting their descent from the surface around sunset (6:00 pm local time; Fig. 2.2a), moving downward at ~380 μm s^{-1} -- about 1.4 m h^{-1} -- often slowing at depth during the subsequent daylight hours. The dense dinoflagellate aggregations arrived at the maximum migration depth (30-40 m) after ~18-24 hours of downward swimming (Fig. 2.2b). These swimming speeds closely match laboratory measurements of *L. polyedra* (100-400 μm s^{-1}; Hand et al. 1965; Eppley et al. 1968; Mayali et al. 2008), and are ten times greater than their sinking speeds (~35 μm s^{-1}; Holmes et al. 1967). On cloudy days with less incoming solar radiation (May 9 and May 10, 2020, Fig. 2.2a), the vertical migration is much less apparent, suggesting that the intensity of daily solar radiation is an important trigger for vertical migration.

Sub-euphotic zone nitrate loss

The downward migration of the dinoflagellates terminated at the depth of the nitracline (strongest vertical gradient in nitrate concentration), where nitrate increased from undetectable levels to >10 mmol m^{-3} over only 2-3 m (Fig. 2.2b). At the beginning of our measurements, the nitracline occurred at a mean-isopycnal depth of ~30 m (Fig. 2.2c). Sub-euphotic zone nitrate concentrations then decreased, resulting in a deepening of the nitracline from an isopycnal depth of ~30 m to ~40 m over a few days. Eventually, nitrate concentrations become undetectable at the maximum migration depth, far below the euphotic zone (Fig. 2.2c contours; Methods).

The loss of sub-euphotic zone nitrate is apparent by comparing historical nitrate and temperature data and data gathered by the WW during the 2020 bloom. Measurements collected over 70 years (CalCOFI program, 1951-2020, Methods) 5 km from the study site show the nitrate-temperature relationship to be extremely stable over time (Fig. 2.3), with a climatological relationship between the nitracline and the 14 °C isotherm (also in Lucas et al. 2011b). Our WW observations revealed a clear deficit of nitrate relative to those climatological values between temperatures of 11 ^{o}C to 14 ^{o}C during the bloom (Fig. 2.3). In the deeper, cold waters (<11 ^{o}C), the nitrate concentrations during the *L. polyedra* bloom were consistent with climatological values, suggesting that in the waters below the maximum migration depth of the dinoflagellates conditions were typical for the area.

The nitrate deficit layer was roughly 25 m in vertical extent, extending from the base of the euphotic zone at ~15 m depth down to ~40 m depth. The maximum nitrate deficit for a given temperature was 14 mmol N m^{-3} relative to climatology (Fig. 2.3), reflecting a profound change in the distribution of inorganic nutrients during the bloom.

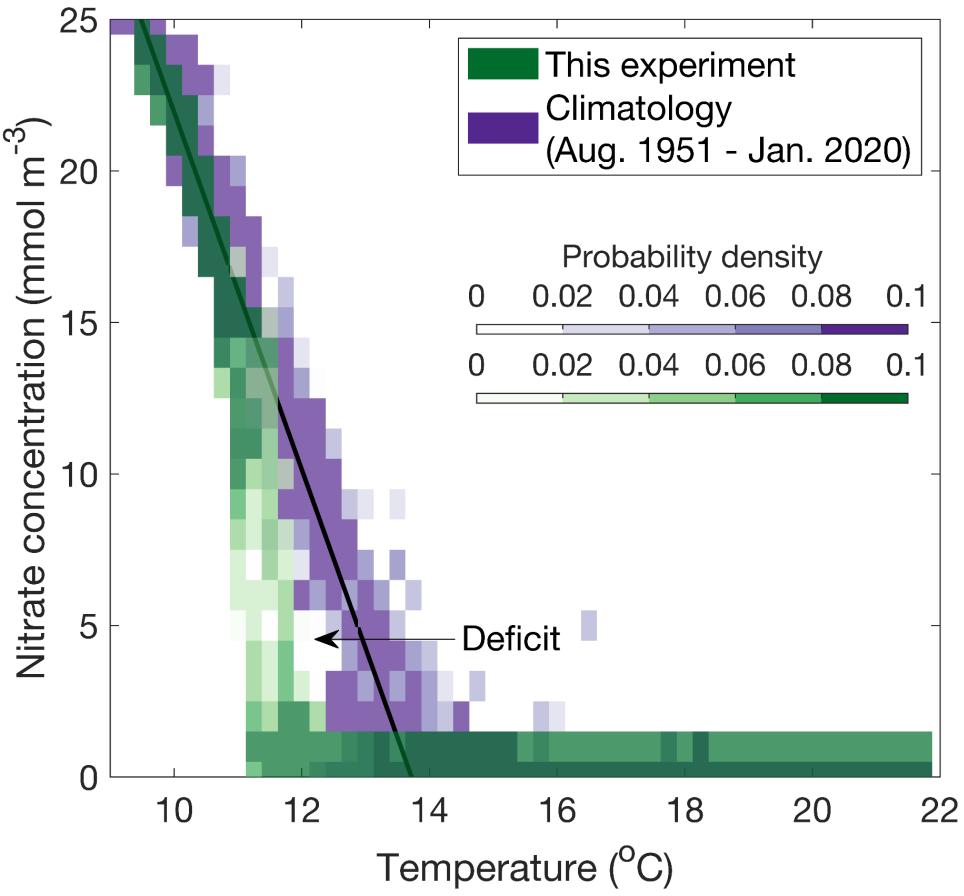

Figure 2.3 Nitrate-Temperature relationship. The combined probability density function (PDF) of nitrate for each 0.25 ºC temperature bin with data from this study (Wirewalker measurements) in green, and climatological data (70 years of CalCOFI bottle samples, line 93.3, station 26.7) in purple. The black solid line represents the least-squares fit to the climatology PDF for temperatures <14 °C, with the equation as: Nitrate = -5.9T+80.94 (T<14 ºC).

Relating the nitrate deficit to vertical migration and phytoplankton growth

We hypothesized that the sub-euphotic zone nitrate deficit was created through nitrate uptake by the downward-migrating dinoflagellates. To test this, we quantified the amount and rate of nitrate loss due to biological uptake, independent of fluctuations driven by physical forcings, such as horizontal and vertical advection of nitrate gradients due to currents and internal waves, respectively.

Transformation to an isopycnal coordinate reference frame removes vertical fluctuations due to internal waves as described above. To remove nitrate fluctuations driven by currents acting on existing environmental nitrate gradients horizontally, we tracked nitrate changes in individual water masses defined by their temperature and salinity properties (*SI Appendix*, Section 7). The oscillating horizontal currents during the WW deployment caused individual water masses to appear multiple times on an isopycnal at the mooring, allowing us to track nitrate changes separately for each water mass as a function of depth and time. This technique largely removed the effects of horizontal advection of nitrate variability at the mooring location (see Fig. 2.2c contours), allowing us to obtain estimates of the depth- and time-dependent biologically-driven loss rates of nitrate. It also allowed us to obtain error estimates for our calculations (*SI Appendix*, Eqs. 9,10,12,14,15).

Successive nitrate measurements in the same water masses gave estimates of the biological nitrate loss rates, ρ_{NO3} (mmol N m^{-3} day^{-1}; *SI Appendix*, Section 8). During a representative 2.5 days, from local noon on May 6th to local midnight on May 8th, estimated nitrate loss rates had a mode of ~6 mmol N m^{-3} day^{-1} in the nitracline. The depth-integrated average nitrate loss rate was 31 +/- 4 mmol N m^{-2} day^{-1} (434 +/- 56 mg N m^{-2} day^{-1}), which is 10 times the nitrogen supply rate over the inner shelf of SCB (Lucas et al. 2011b), and 20 times the vertical nitrate flux rate based on the Biologically Effective Upwelling Transport Index (BEUTI) at the sample time (Methods) -- emphasizing an enormously high nitrate demand during the red tide that cannot be met by typical physical nutrient delivery mechanisms. Integrating ρ_{NO3} in time generated estimates of the amount of nitrate taken up by the dinoflagellates, N_{loss} (mmol N m^{-3}) (*SI Appendix*, Section 8, Fig. 2.S8). N_{loss} ranged from 0 to 12 mmol N m^{-3} in a ~10-13 m thick layer below the euphotic zone (Fig. 2.4a).

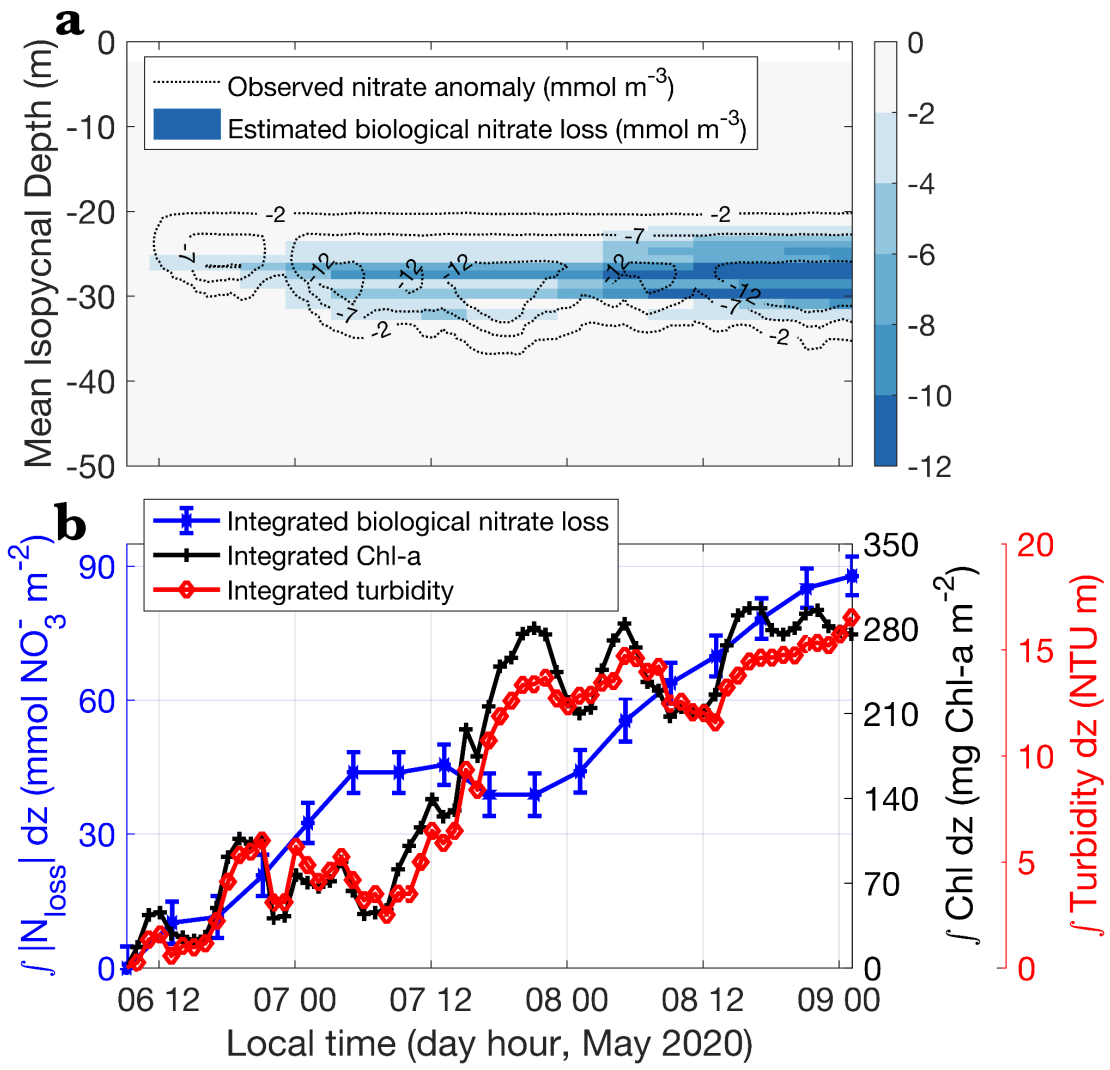

Figure 2.4 Variability in nitrate concentration at depth due to dinoflagellate migrations. a) Estimated biologically induced nitrate loss (color) and observed nitrate anomaly (contours) referenced to the first profile during this period. b) Time series of depth-integrated (0-33 m) absolute biologically induced nitrate loss (the blue line with star markers), Chl-a concentration (the black line with plus markers), and turbidity (the red line with diamond markers). Error bars represent error estimations following the standard error propagation procedures (see *SI Appendix*).

Fluctuations in the layer of nitrate loss (Fig. 2.4a) coincided in time and space with the maximum migration depths of *L. polyedra* (Fig. 2.2b). Furthermore, the calculated nitrate loss rates are consistent with nitrate uptake rates reported from lab experiments with *L. polyedra* (1 - 4

mmol N m^{-3} day^{-1}; Eppley and Harrison 1975; Harrison 1976), and the estimated average N:Chl-a ratio of 5.3 is within the expected range for *L. polyedra* (Prezelin et al. 1986). Importantly, the time series of depth-integrated nitrate loss, $\int N_{loss}(z,t)\ dz$, was significantly correlated with the time series of increases in both depth-integrated Chl-a concentration ($R = 0.81$, $P < 0.0001$) and depth-integrated turbidity measured at 532 nm ($R = 0.82$, $P < 0.0001$) (Fig. 2.4b) -- directly linking loss of nitrate and gain of Chl-a organic particle loads. The consistency of estimated nitrate loss rates with *L. polyedra*'s nitrate uptake rates, and the correlations of nitrate loss with increases in both Chl-a and turbidity, provide strong support for the hypothesis that the nitrate loss was caused by the uptake of nitrate by *L. polyedra* migrating vertically into the sub-euphotic zone nitrate pool. This nitrate uptake depleted the sub-euphotic zone nitrate concentrations and deepened the nitracline (Fig. 2.4a). Since the measured descent rates of the bloom allowed for ~35 m d^{-1} vertical travel, we suggest that the deepening of the nitracline beyond the reach of the dinoflagellates during a daily migration period contributed to the eventual demise of the bloom.

Summary

Eppley et al. (1968) hypothesized that dense HABs can form by dinoflagellates migrating upward during the day to photosynthesize, and downward at night to take up nitrate and other nutrients from the pool below the euphotic zone. Despite laboratory experiments supporting this DVM-bloom hypothesis, a comprehensive test of this hypothesis in the field was lacking. Using a multi-sensor autonomous profiling mooring deployed during a dense red tide in Southern California, we showed that the bloom-forming dinoflagellates vertically migrated, that they took up nutrients from below the euphotic zone during the deep phase of the migration, and that dinoflagellate abundances subsequently increased in proportion to the nutrient uptake. These

observations confirm that vertical migration played a key role in maintaining the extreme biomass of the bloom.

Vertical migration allows dinoflagellates to acquire an essential nutrient from the deep inorganic nutrient pool below the surface euphotic zone. This swimming-mediated nutrient-retrieval ability enables motile dinoflagellates to overcome the oppositely directed gradients of available light and nutrients, and thus provides them a competitive advantage over non-motile species in strongly stratified conditions. In the case reported here, the nitracline was forced to a depth far below the euphotic zone, suggesting that non-motile phytoplankton, such as the typically dominant diatom species, would be starved of inorganic nutrients at depths with sufficient sunlight to photosynthesize and grow. The dense, prolonged bloom we observed produced historically anomalous subsurface nutrient distributions, showing the potential of HABs to reshape the environmental character of the coastal ocean. The continued development of autonomous systems equipped with high-resolution physical and biogeochemical sensors will advance our understanding of the interplay between environmental conditions and the behavior and metabolic needs of bloom-forming organisms. Including these biophysical feedbacks in numerical models is necessary to improve our ability to forecast harmful algal blooms in the future.

Methods

Our data came from a moored ocean-wave-powered Wirewalker (WW) profiler, the long-term Del Mar Mooring (DM), the California Cooperative Oceanic Fisheries Investigations (CalCOFI) program, and the Southern California Coastal Observing System (SCCOOS). The Wirewalker is an autonomous vertical profiling system that allows the collection of high-resolution upper-ocean physical and biogeochemical properties (Rainville and Pinkel 2001; Pinkel et al. 2011; Lucas et al. 2017). The WW was equipped with a conductivity-temperature-depth (CTD)

sensor (RBR Concerto), nitrate sensor (SUNA V2), Chl-a fluorescence and optical backscatter sensor (SBE ECOPuck), and irradiance sensor (SBE OCR-504). The SUNA (Submersible Ultraviolet Nitrate Analyzer, Sea-Bird Scientific) estimates nitrate concentration (unit: μM, 1 μM = 1 mmol m^{-3}) based on the absorption spectrum of the water sample in the UV light region (Johnson and Coletti 2002). Data analysis procedures for raw nitrate data quality control, non-photochemical quenching correction for fluorescence, calculation of PAR, and estimation of turbidity are presented in the Supplementary Information (*SI Appendix,* Sections 2-4). SUNA was configured to sample with a duty cycle of 20 minutes per hour with a 1 Hz sampling rate. All other sensors onboard the WW had a sampling frequency of 6 Hz. Over the three-week period from April 29, 2020 to May 21, 2020, the final gridded WW data had 1 m vertical resolution and ~15 min temporal resolution, determined by the sampling rate of SUNA and vertical speed of the WW, respectively.

The Del Mar Mooring (Fig. 2.1a) is a full water column physical-biogeochemical mooring maintained by the Ocean Time-Series Group at the Scripps Institution of Oceanography, continuously measuring ocean temperature, salinity, currents, oxygen concentration, fluorescence, and nutrients. Phytoplankton images (Fig. 2.1b) were captured at approximately 4 m depth by an Imaging FlowCytobot (IFCB, Olson and Sosik 2007; Sosik and Olson 2007) -- an automated underwater imaging system that captures high-resolution images of suspended particles, including *L. polyedra*, with size ranges from <10 to 150 μm. Phytoplankton in each IFCB sample are identified to species or genus level using image classification approaches; Kahru et al. (2021) examined the daily average abundance of *L. polyedra* inferred from the IFCB and found correspondence with nearby microscope counts and satellite-measured chlorophyll during this red tide.

The CalCOFI is a long-term ocean monitoring program that has collected full water-column samples at specific stations off the coast of California since 1949 (quarterly since 1984). We used data collected at the innermost station on Line 93.3, located at 32.956 ºN 117.305 ºW, ~5 km from the Del Mar mooring location.

The CalCOFI and Wirewalker nitrate vs. temperature PDFs (Fig. 2.3) were calculated using nitrate data in 0.25 ºC temperature bins and 1 mmol m^{-3} nitrate bins.

To convert from depth to isopycnal coordinates, raw physical and biogeochemical variables from each individual WW profile were interpolated onto uniformly gridded density bins (density interval of 0.02 kg m^{-3}) (*SI Appendix*, Fig. 2.S4 and 2.S5). Mean isopycnal depths were calculated as the time-averaged interpolated depth for each gridded density bin over the course of the study period (see *SI Appendix* Section 5).

To remove the effects of horizontal along-isopycnal advection from biological processes, for each isopycnal, data were binned by their level of spice (Temperature/Salinity properties; Flament 2002) with a 0.005 kg m^{-3} interval. Points in the same spice bin on an isopycnal were assumed to be the same water mass (*SI Appendix*, Fig. 2.S7). The rate of change of nitrate (ρ_{NO3}, units: mmol N m^{-3} day^{-1}) was estimated from nitrate concentration changes within each individual water mass by first fitting an exponential function to pairs of nitrate measurements separated by a time interval Δt (determined by the reappearance of a particular water mass at the mooring): $N(t + \Delta t) = N(t)e^{r\Delta t}$. These fits gave estimates of r -- the nitrate-specific rate of change (units: day^{-1}). The predicted biologically driven nitrate loss was then calculated by temporally iterating r over an uniform time interval δt (details in *SI Appendix*, Fig. 2.S8). The nitrate loss rate ρ_{NO3} was simply a temporal differentiation of the predicted nitrate loss (*SI Appendix*, Fig. 2.S8). The

associated error for each estimated quantity followed standard error propagation procedures (*SI Appendix*).

The biologically effective upwelling transport index (BEUTI) is an estimate of the vertical nitrate flux to the surface mixed layer (Jacox et al. 2018). Averaged BEUTI over the study period at 33 ^{o}N is 1.363 mmol N m^{-1} s^{-1}, which can be converted to an estimated nitrate flux of 1.6 mmol N m^{-2} day^{-1} after averaging over a cross-shore distance of 75 km.

Supplementary Information (SI):

1. Precipitation

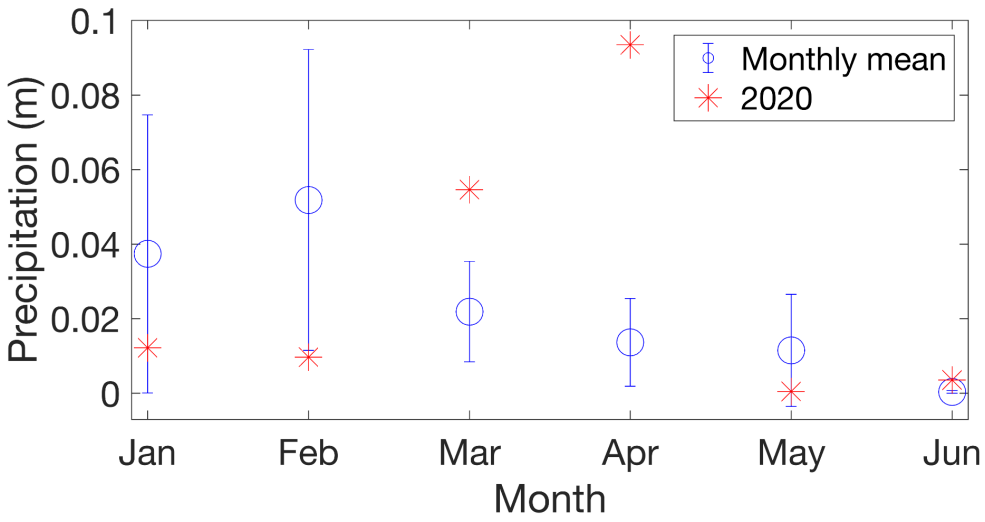

Fig. 2.S1 monthly mean (from 2000 to 2019) vs. 2020 precipitation in San Diego. The error bar is one standard deviation. Data from the National Weather Service.

2. Nitrate data quality control

Building on previous quality control procedures for SUNA measurements (e.g., Lilly et al. 2019; Johnson et al. 2021), here we report the nitrate data quality control process for data acquired from the Wirewalker (WW) SUNA V2 combination (Fig. 2.S2 and text below):

- Step 1: The SUNA was configured to have a duty cycle of 20 minutes per hour with a sampling frequency of ca. 1 Hz. Raw nitrate data (unit: µM; 1 µM = 1 mmol m^{-3}) was

recorded in the unit as a function of time. The 95% confidence limit of raw nitrate data (determined by calculating the probability density function of nitrate data within a 0.5 ^{o}C range) was 1 mmol m^{-3} (about 2 standard deviations). This value was used in subsequent error calculations.

- Step 2: The raw nitrate data contained outliers, such as unexpected zeros or extreme values (about 5% of the total amount of the data). These points were removed.
- Step 3: The SUNA V2 pump stream was oriented with the intake facing in an upwards direction. For this reason, measurements collected during the upward, free-ascent travel of the Wirewalker were used in this analysis.
- Step 4: The nitrate data exhibited a temporal drift – increasing ca. 3 mmol m^{-3} over 8 days consistently across all depths (Fig. 2.S2a). This consistency indicates this temporal drift is an instrument error and thus needs to be accounted for. The minimum nitrate value within each duty cycle was first selected and then a low-pass filter with a cut-off frequency of 0.5 cpd was applied to the time series formed by these selected points to obtain a smoothed baseline. Assuming that the actual minimum nitrate concentration was consistently 0 over the course of the deployment, this baseline was subtracted from the upcast data to bring the minimum values back to 0, as shown in Fig. 2.S2b.
- Step 5: The nitrate-temperature relationship using the temporal-drift-corrected nitrate data showed a positive relationship between nitrate and temperature above 12 ^{o}C (Fig. 2.S2d, also shown as the non-monotonic vertical nitrate gradient near the ocean surface in Fig. 2.S2b). This positive relationship is not real. Previous literature (e.g., Sakamoto et al. 2009) has also shown a temperature-dependent response of the nitrate sensor. This temperature effect was corrected by first fitting a linear function to temperature and nitrate data in the

temperature range where nitrate is expected to be 0 (here above 12 ºC), and then subtracting this linear function from the data. The result is shown in Fig. S2c-d, where nitrate is consistently 0 above a particular temperature threshold, as expected from previous data (e.g., Lucas et al. 2011b).

- Step 6: Given the ca. 1 Hz sampling rate of SUNA, and an average vertical speed of 0.3 m s^{-1} for WW, nitrate data for each WW profile were gridded into uniform 1-m depth bins from the surface down to 100 m depth.

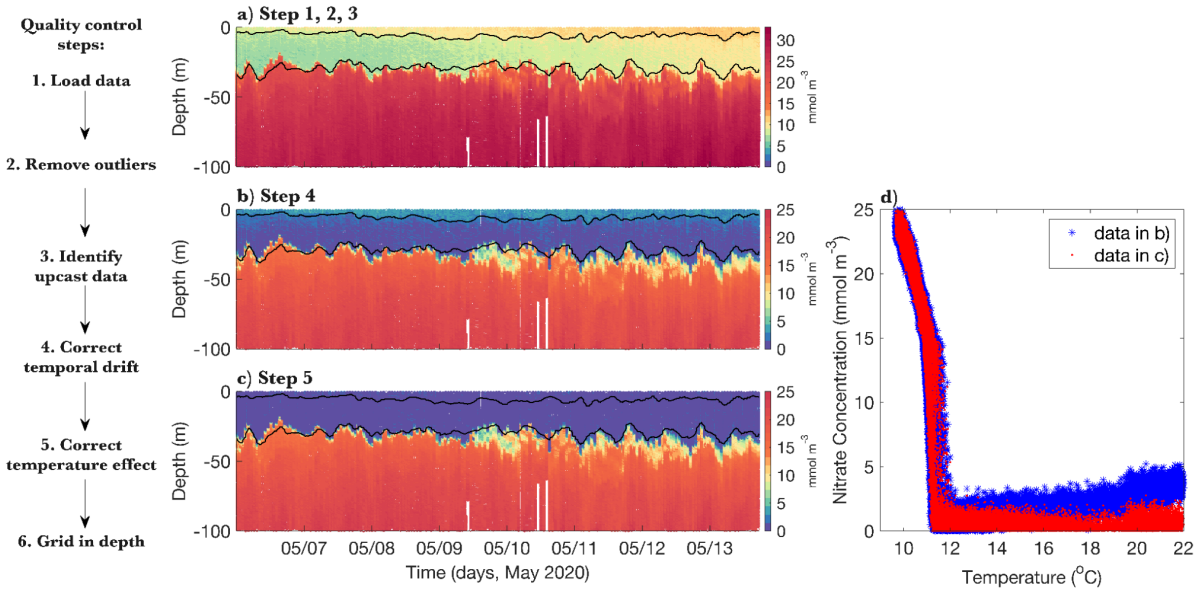

Figure 2.S2 Nitrate data quality control procedures. Texts on the left outline the steps for nitrate data quality control. a-c) The results after specific step(s) have been applied to the nitrate data, with nitrate plotted in color as a function of depth and time. The two black lines are two isopycnals plotted for reference. Note that the colorbar range is different in a, compared to b and c, but the colormap is the same from 0-25 mmol m^{-3} for all panels. d) The nitrate-temperature relationship based on data before (blue stars) and after (red dots) implementing the temperature correction.

3. Chlorophyll fluorescence (ChlF) data analysis

Non-photochemical quenching (NPQ) is a photoprotective mechanism that suppresses fluorescence under high irradiance. Hence, *in situ* fluorescence data need to be corrected as NPQ-

induced fluctuations do not represent real changes in biomass. Adapted from other NPQ correction methods applied to a diversity of profiling platforms, including the Wirewalker (e.g., Davis et al. 2008; Todd et al. 2009; Schlosser et al. 2023) we estimated NPQ by first calculating the correlation coefficient between ChlF and PAR using all the data between the surface and 4 m in a two-day window. If the correlation coefficient was less than -0.1, the NPQ value for the full water column would be calculated as a linear function of PAR with the transfer function coefficients estimated from the linear fit of ChlF and PAR in the upper 4 m. The same process was applied incrementally to the whole data set using a 0.1-day offset. The final NPQ value was the average across all the increments that contained that time point. The NPQ-corrected ChlF data was obtained by adding the NPQ correction to the raw ChlF data.

ChlF was initially recorded in units of relative fluorescence units (RFU). To convert ChlF into the more common chlorophyll-a (Chl-a) concentrations (unit: mg m^{-3}), the linear fit was calculated between the WW 31-33 m depth-averaged ChlF time series (points) and the nearby Del Mar Mooring 32 m calibrated Chl-a time series (mg m^{-3}) (correlation coefficient of 0.91, plot not shown here). This regression was used to estimate a conversion function for Chl-a from points to mg m^{-3}:

$$Chla = 0.05 * (ChlF - 44.95), \quad (1)$$

where $Chla$ represents Chl-a in units of mg m^{-3} and $ChlF$ represents ChlF in RFU. Eq.1 was applied to all the NPQ-corrected ChlF measurements.

4. The light field, with optical backscatter

The photosynthetically available radiation (PAR) was estimated by integrating the observed irradiance at wavelengths of 380 nm, 412 nm, 490 nm, and 532 nm and then

interpolating/extrapolating to the range between 400 nm to 700 nm (i.e., the full PAR range). The equation is:

$$PAR(z,t) = \sum_{n=1}^{4} I_n(z,t)\,\Delta\lambda \times \frac{700-400}{532-380} \times 0.046, \quad (2)$$

where I is the measured irradiance in units of $\mu W\ cm^{-2}\ nm^{-1}$, n represents each wavelength, $\Delta\lambda$ is the wavelength interval size, and 0.046 is for conversion from $\mu W\ cm^{-2}$ to $\mu mol\ m^{-2}\ s^{-1}$. Fig. 2.S3a shows that even though the surface PAR had some spikes, the shortwave radiation (measured independently at the Scripps Pier) was about two to ten times larger than surface PAR -- suggesting that about 50%-90% of the input solar energy was absorbed in the surface 3 m. Below the ocean surface, PAR was modeled as decaying exponentially in depth:

$$I(z) = I_0 e^{kz}, \quad (3)$$

where I_0 is the PAR value at the ocean surface, k is the diffuse attenuation coefficient of irradiance, and z is depth. For each WW profile, k can be estimated from linear fits of $ln[I(z)]$ vs. depth, giving values between 0.08 m^{-1} and 0.6 m^{-1}. The euphotic depth (Z_{eu}), defined as the depth where PAR is 1% of its surface value, was estimated from:

$$Z_{eu} = \frac{ln(0.01)}{k}. \quad (4)$$

A larger absolute Z_{eu} means that the water is clearer, with a deeper penetration of light. A positive correlation between Z_{eu} and upper ocean (0-30 m) phytoplankton biomass (or particle load) (Fig. 2.S3b) demonstrates that the subsurface light field was strongly modulated by upper ocean biological properties during the red tide: that is, the irradiance was attenuated by the dense phytoplankton community in addition to the expected decay of light in clear water.

Turbidity (suspended particle load) was estimated from the optical backscatter data using the instrument's factory calibration:

$$Turbidity = 0.0061 * (OBS - 50), \quad (5)$$

where $Turbidity$ is in units of NTU (Nephelometric Turbidity Units), and OBS is the measured optical backscatter at 532 nm. Fig. S3d showed similar spatial-temporal patterns as Chl-a (Fig. 2.1e), indicating that the suspended particles in the upper ocean were dominated by phytoplanktons during the observational period. Note that we use turbidity as a relative measure, and the sensor is assumed to be stable in time.

5. Depth-to-isopycnal coordinate transformation

Raw data were recorded as a function of depth (pressure) and time, as seen in Fig. 2.1c-f. Within a depth range, raw measurements have variations both along and cross the isopycnals as a function of time. An example of nitrate concentrations in T/S space (Fig. 2.S4) shows both a general trend of decreasing nitrate with decreasing density (i.e., cross-isopycnal variability), and variations of nitrate over time at the same density value (i.e., along-isopycnal variability). When internal waves were present, cross-isopycnal variability appears as temporal changes of nitrate (and other variables like temperature and salinity) in the depth coordinate system driven by vertical heaving of isopycnals. This complicates calculations of temporal change at any depth, especially for dynamically passive but biologically active tracers such as nitrate. Transforming from depth coordinates to isopycnal coordinates will remove the vertical displacements created by internal waves, decoupling the fluctuations induced by vertical displacements of isopycnals from those caused by biological uptake and horizontal (along-isopycnal) gradients.

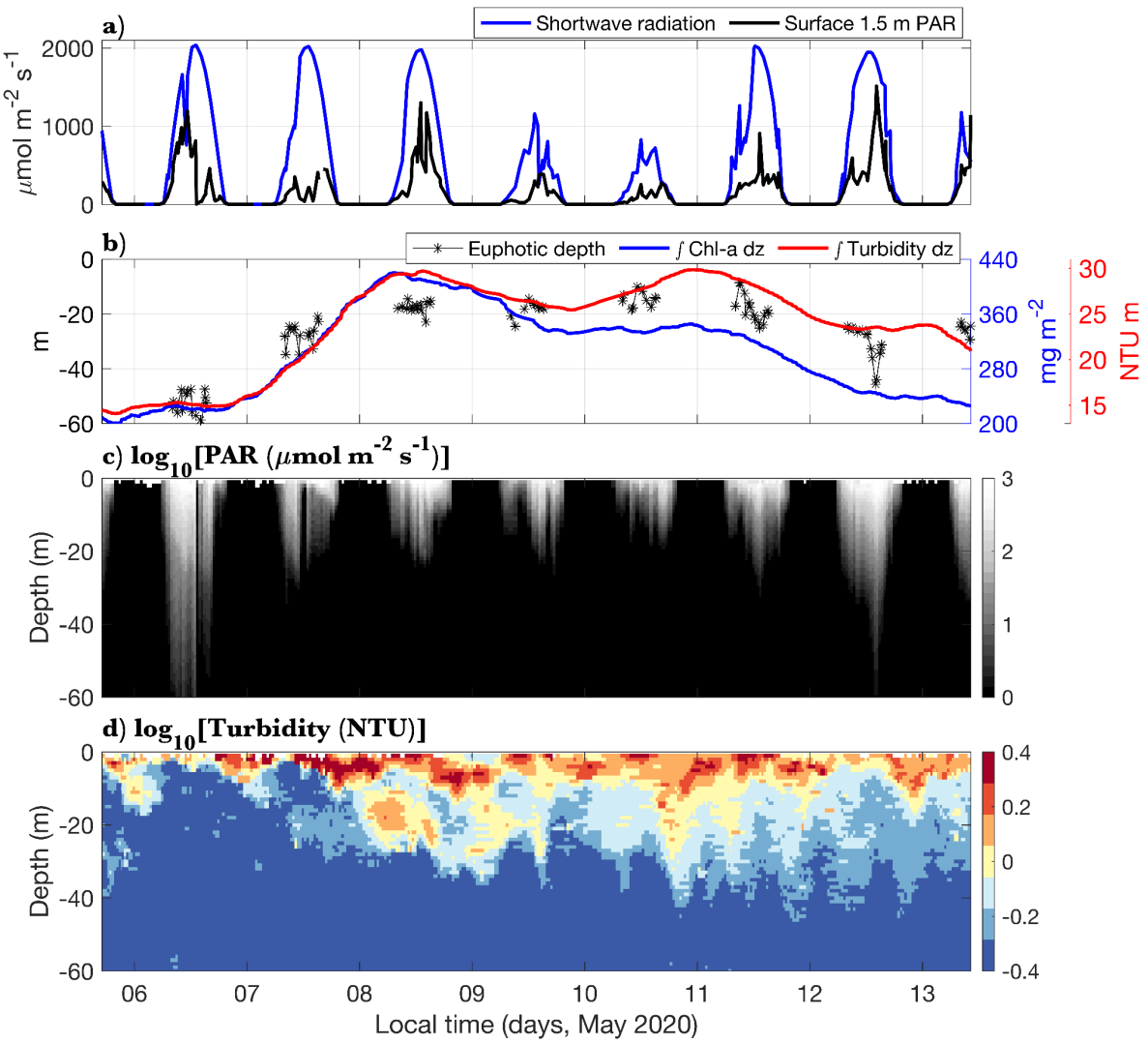

Figure 2.S3 Irradiance and turbidity. a) Shortwave radiation (400 nm - 700 nm range) measured at the Scripps Pier (blue line) and surface 3 m depth-averaged PAR estimated from the irradiance measurements from the Wirewalker (black line). b) Estimated euphotic depth (black stars), and 0-30 m depth-integrated Chl-a and turbidity in blue and red respectively. Note that the Chl-a and turbidity time series went through a 24-h running mean filter to smooth out short-time-scale variabilities. c-d) PAR and turbidity from the WW as a function of time and depth, respectively. Note that only the upper 60 m of data are shown here.

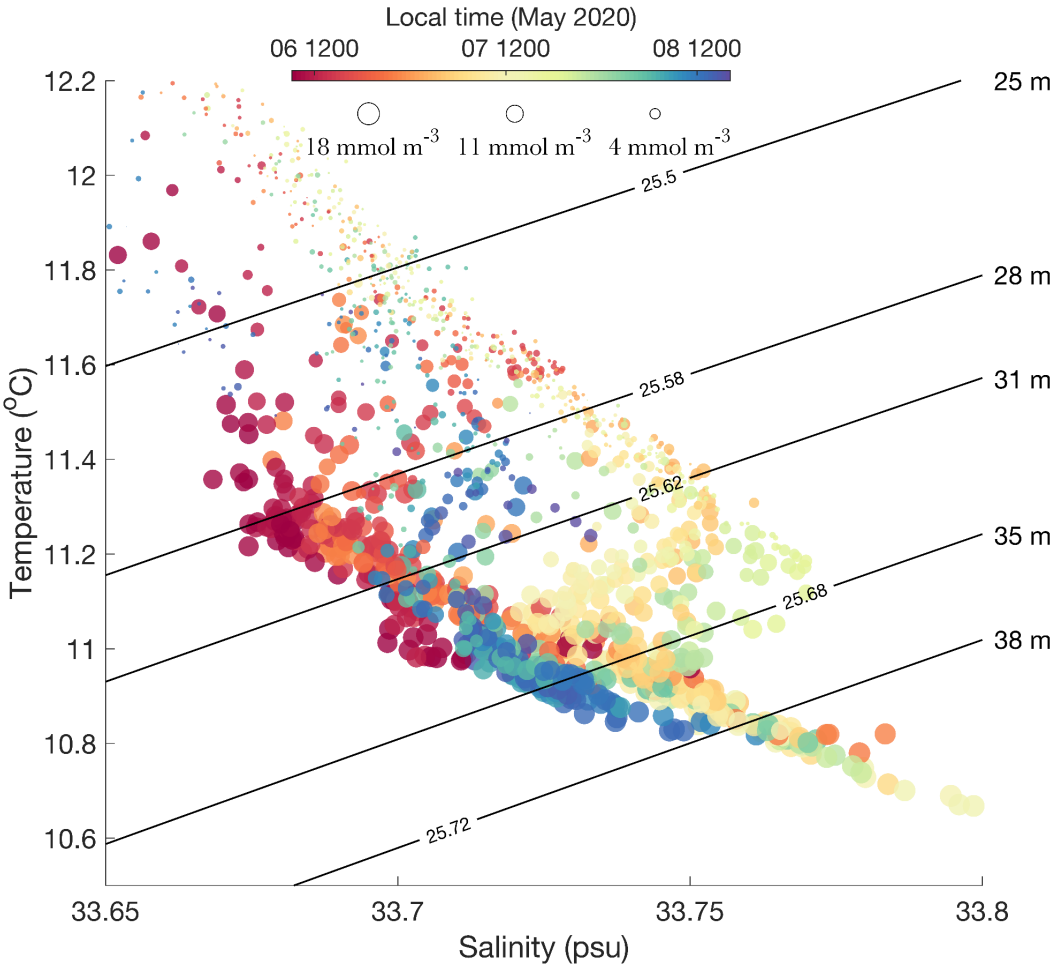

Figure 2.S4 Temperature and salinity characteristics of data (T/S diagram) from the Wirewalker acquired during a 2-day window between 22 and 35 m depth. Data points are colored by time, and point size is proportional to nitrate concentration. The black lines are five isopycnals, with their corresponding mean isopycnal depths denoted at the right-hand end of the curve. Note that there is a variation of T, S, and nitrate along some isopycnals.

The depth-to-isopycnal coordinate transformation was executed by interpolating raw physical and biogeochemical variables from each individual WW profile onto uniformly-gridded density bins (here, the density interval was set to be 0.02 kg m^{-3}). Similarly, raw pressure measurements were also interpolated to give the instantaneous depths of each density bin for each profile. The mean isopycnal depth was calculated as the time-averaged interpolated depth for each gridded density bin over the course of the study period. As the mean isopycnal depth accounts for

the different vertical spacings between different density layers, it provides a more realistic representation of the vertical distribution of density layers than using density as the y axis.

This different spacing of density bins in depth also leads to different numbers of raw measurement points in each gridded density bin, which results in different errors associated with the transformed values. To estimate the errors, the standard error of the mean (SEM; the standard deviation of the mean of multiple samples means) was calculated for each density bin:

$$SEM = \frac{\sigma}{\sqrt{n}}, \tag{6}$$

where σ is the standard deviation of the raw measurements, and n is the number of points within each density bin. An example of the coordinate transformation result is shown in Fig. 2.S5, where vertical displacements of the isopycnals disappear after applying the depth-to-isopycnal transformation. While temperature and salinity are relatively constant along isopycnals (Fig. 2.S5b,d), the along-isopycnal nitrate displays considerable variability (Fig. 2.S5f).

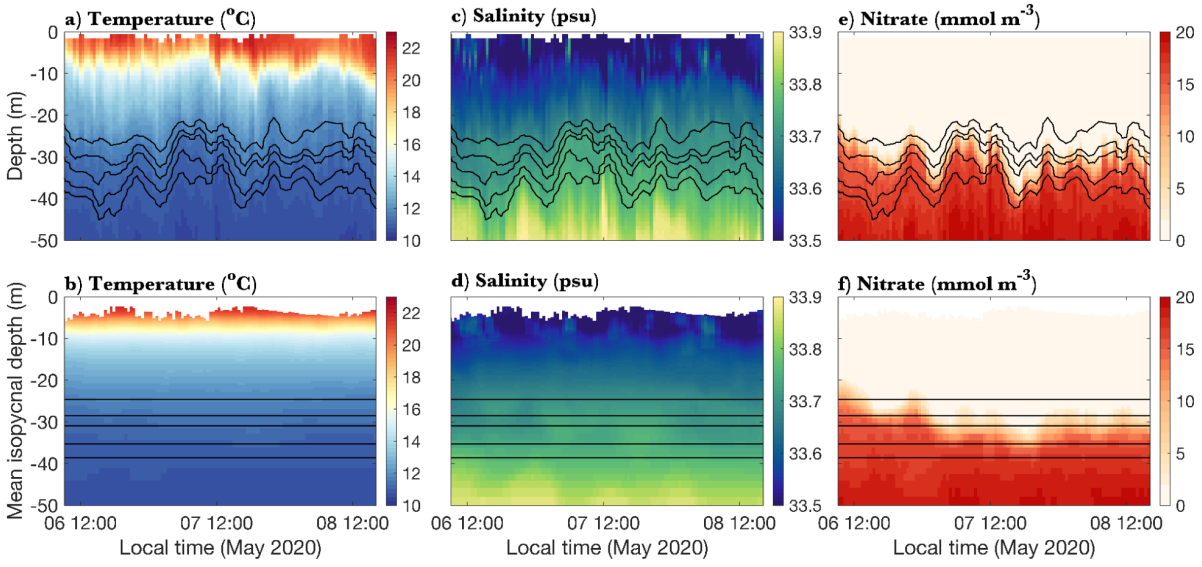

Figure 2.S5 Examples of the depth-to-isopycnal coordinate transformation. a/c/e) Observed temperature, salinity, and nitrate as a function of depth and time. Black lines show isopycnals with values of 1025.5 kg m^{-3}, 1025.58 kg m^{-3}, 1025.62 kg m^{-3}, 1025.68 kg m^{-3}, and 1025.72 kg m^{-3} respectively. b/d/f) Temperature, salinity, and nitrate as a function of gridded density bin (plotted as their mean depths) and time, with black lines representing the same densities as the upper panels.

6. Along-isopycnal velocities

As Eulerian measurements (fixed point mooring), the along-isopycnal WW time series for each variable contains temporal gradients driven by horizontal advection of existing spatial gradients. As seen in Fig. 2.S6c, from noon 05/06 to 05/08, the along-isopycnal nitrate and horizontal velocities (southeast-ward current corresponding to decreasing of nitrate) were correlated, suggesting that changes in the along-isopycnal nitrate were partially driven by horizontal advection. Crucially, the advective signal will confound estimates of biologically driven nitrate rates of change, and thus must be accounted for. The detailed procedures are shown below.

7. Temperature/Salinity (T/S) binning

To separate the effects of horizontal advection from biological activities in the along-isopycnal nitrate time series, we applied a Temperature/Salinity binning method, which utilized spiciness as a tracer to follow the same water parcel (defined by the same spiciness) in time. Spiciness is a quantity related to Temperature/Salinity variations on a density layer: more positive means warmer and saltier water (spicier), while less positive means cooler and fresher water (mintier) (Flament 2002). Thus, temporal changes of nitrate concentration driven only by biological processes can be calculated by using nitrate measurements within each water mass. An example of how this method was performed is shown in Fig. 2.S7. Along each isopycnal, data points were rearranged into evenly-spaced spiciness bins (interval of 0.005 kg m^{-3}). Points in the same spiciness bin were assumed to represent the same water mass. Note that the number of data points in each spiciness bin will vary.

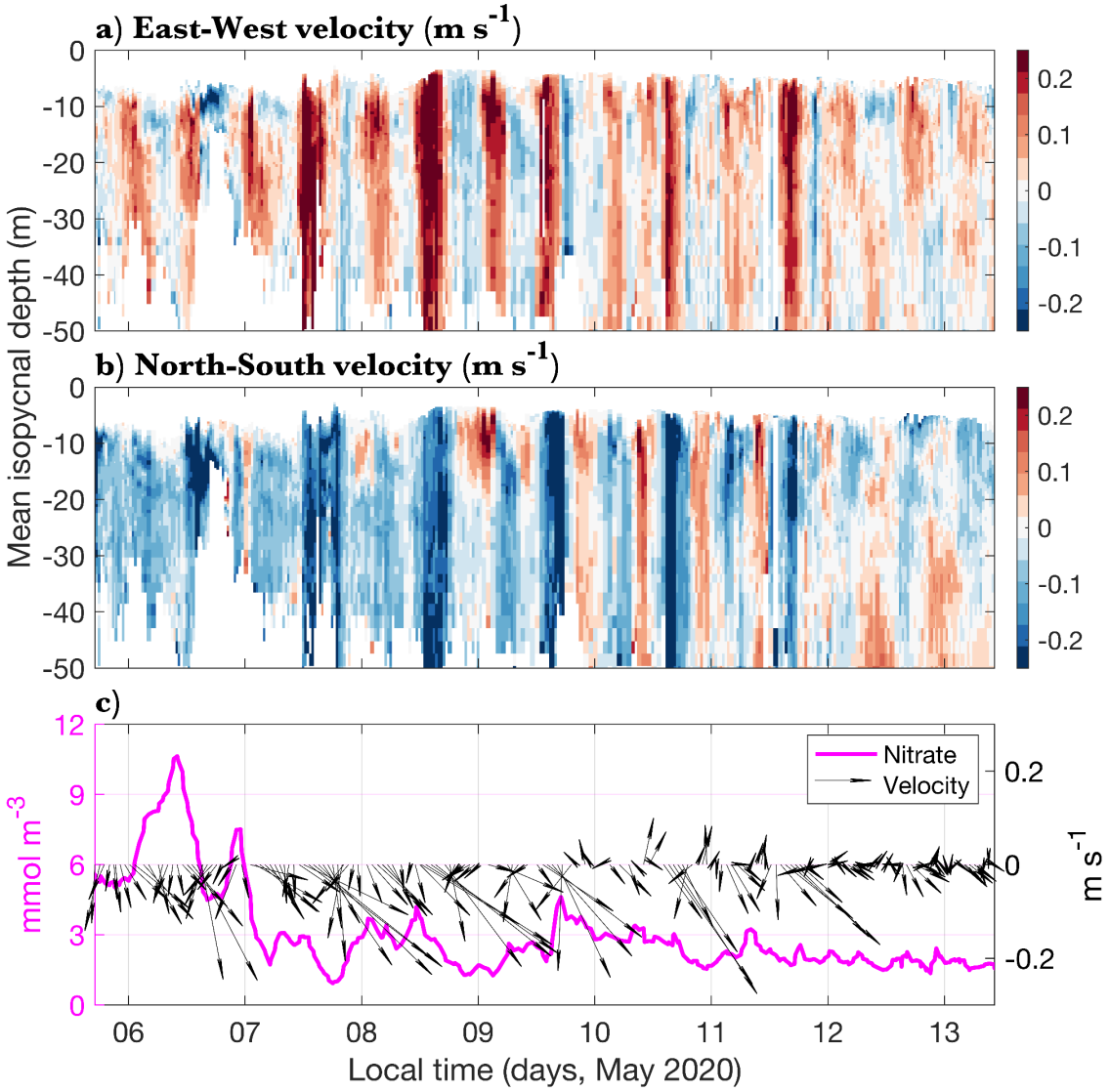

Figure 2.S6 a-b) Along-isopycnal East-West velocity and North-South velocity respectively. c) 20-35 m depth-averaged nitrate in magenta, with black arrows showing the direction and the magnitude of the velocity, with up and right indicating the northward and eastward direction, respectively. Note the correlations of nitrate fluctuations with velocity fluctuations, consistent with horizontal advection of existing horizontal (along-isopycnal) gradients of nitrate.

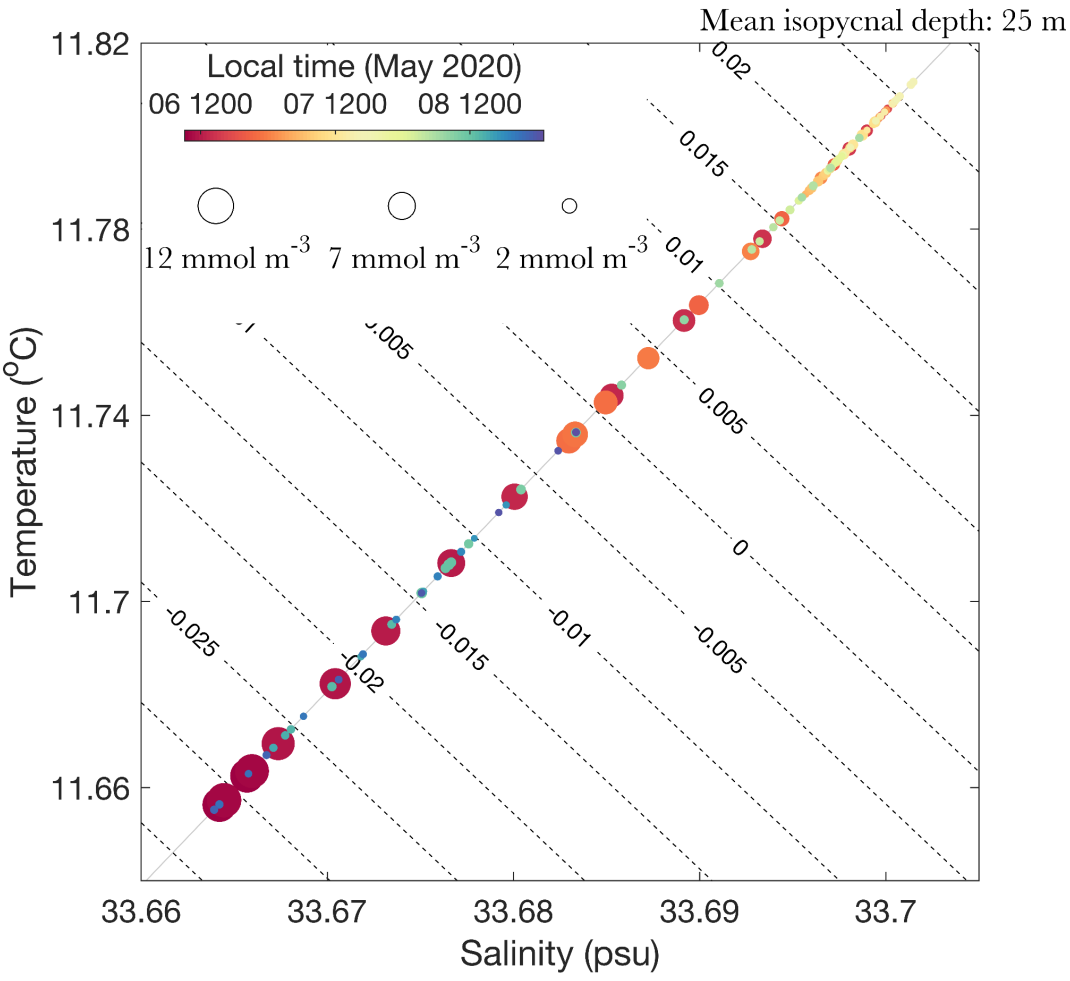

Figure 2.S7 An example of T/S binning by spiciness on isopycnal 1025.5 kg m^{-3}. Color represents time, and symbol size represents nitrate concentration. The grey line shows the isopycnal. The black dashed lines are spiciness anomaly contours (spiciness minus the spiciness calculated from the mean T/S on this isopycnal) with an interval of 0.005 kg m^{-3}.

8. Estimation of nitrate rate of change

Rates of change of nitrate, ρ_{NO3} (unit: mmol N m^{-3} day^{-1}), quantify how fast nitrate changes over time, and are estimated from the specific nitrate rate of change, r (unit: day^{-1}), following the procedures described below.

After the T/S binning, within each water parcel, nitrate can be modeled as changing exponentially over time (similar to Cullen 1985). The equation for the temporal evolution of nitrate can be expressed as:

$$N(t) = N_0 e^{rt}, \quad (7)$$

where N_0 is the initial nitrate concentration, and t is time (days). Using consecutive points in each spiciness bin (i.e., each water mass), r was estimated as:

$$r(i) = \frac{1}{t(i+1)-t(i)} * ln\left(\frac{N(i+1)}{N(i)}\right), \quad (8)$$

where N is the measured nitrate concentration, and i represents the time index of the data. The error for r was calculated as:

$$r_E(i) = \frac{1}{t(i+1)-t(i)} * \sqrt{\left(\frac{SEM(i)}{N(i)}\right)^2 + \left(\frac{SEM(i+1)}{N(i+1)}\right)^2}. \quad (9)$$

An example is shown in Fig. S8a. Note that this exponential fitting was only applied when the absolute difference between two points was larger than 2 mmol m^{-3} (2 times raw nitrate data's confidence limit) -- ensuring a statistically significant estimate of r that can be further interpreted as biological processes. Due to this criterion, some estimates of r were undefined. Overall, the probability density functions (PDFs) of the estimated r (Fig. 2.S8d) show a clear distribution of the majority of the data being negative, consistent with the observations of nitrate loss over time. Furthermore, estimates of r give a distinct mode value of -1 day^{-1} (Fig. 2.S8d), indicating that the loss rate of nitrate is relatively constant among different water parcels, across different isopycnals, and over time. Although experiments were done under different conditions (lab vs. nature), and with different species (*Heterocapsa niei* vs. *Lingulodinium polyedra*), our estimated r is consistent with the values reported in Cullen (1985).

A temporal integration of the estimated $r(z,t)$ was performed to estimate the changes in the nitrate field driven only by biological activities -- that is, without the effects of advection. Due to the fact that estimates of r had uneven time intervals along each isopycnal (primarily due to the inconsistent presence of different water masses at the WW), a rebinning in time was executed by setting a uniform time bin of 4 hours, and choosing the median r value within each 4-hour window to be the rebinned r, denoted as r_{bin}. Its error is:

$$r_{bin,E} = \frac{1}{m} * \sqrt{\sum_{i=1}^{m}(r_E(i))^2}, \tag{10}$$

where m is the number of estimates of r in each time bin. Even though the time resolution of the nitrate estimates decreased after this rebinning process, there were two distinct advantages: 1) the process generated a uniform time interval for further nitrate calculations; 2) the process compensated for non-significant values previously excluded in the estimates of r.

The predicted biologically-mediated nitrate concentration, N_{pred} was calculated using the estimates of r along each isopycnal as:

$$N_{pred}(i+1) = N_{pred}(i)e^{r_{bin}(i)*\Delta t}, \tag{11}$$

where Δt is the time interval between estimates of r (4 hours), i represents the index of the data, and the initial value is taken from the first profile shown in Fig. 2.2c from the observations. The error associated with the predicted nitrate is estimated as:

$$N_{pred,E}(i+1) = \sqrt{(e^{r_{bin}(i)*\Delta t} * N_{pred,E}(i))^2 + (N_{pred}(i) * \Delta t * e^{r_{bin}(i)*\Delta t} * r_{bin,E}(i))^2}. \tag{12}$$

N_{pred} is shown in Fig. 2.S8b, with signatures of clear deepening of nitrate contours in time, and also decreasing of nitrate along isopycnals in time between 20 m and 33 m. These

patterns are consistent with the observations (Fig. 2.2c), but have had advection-associated fluctuations removed.

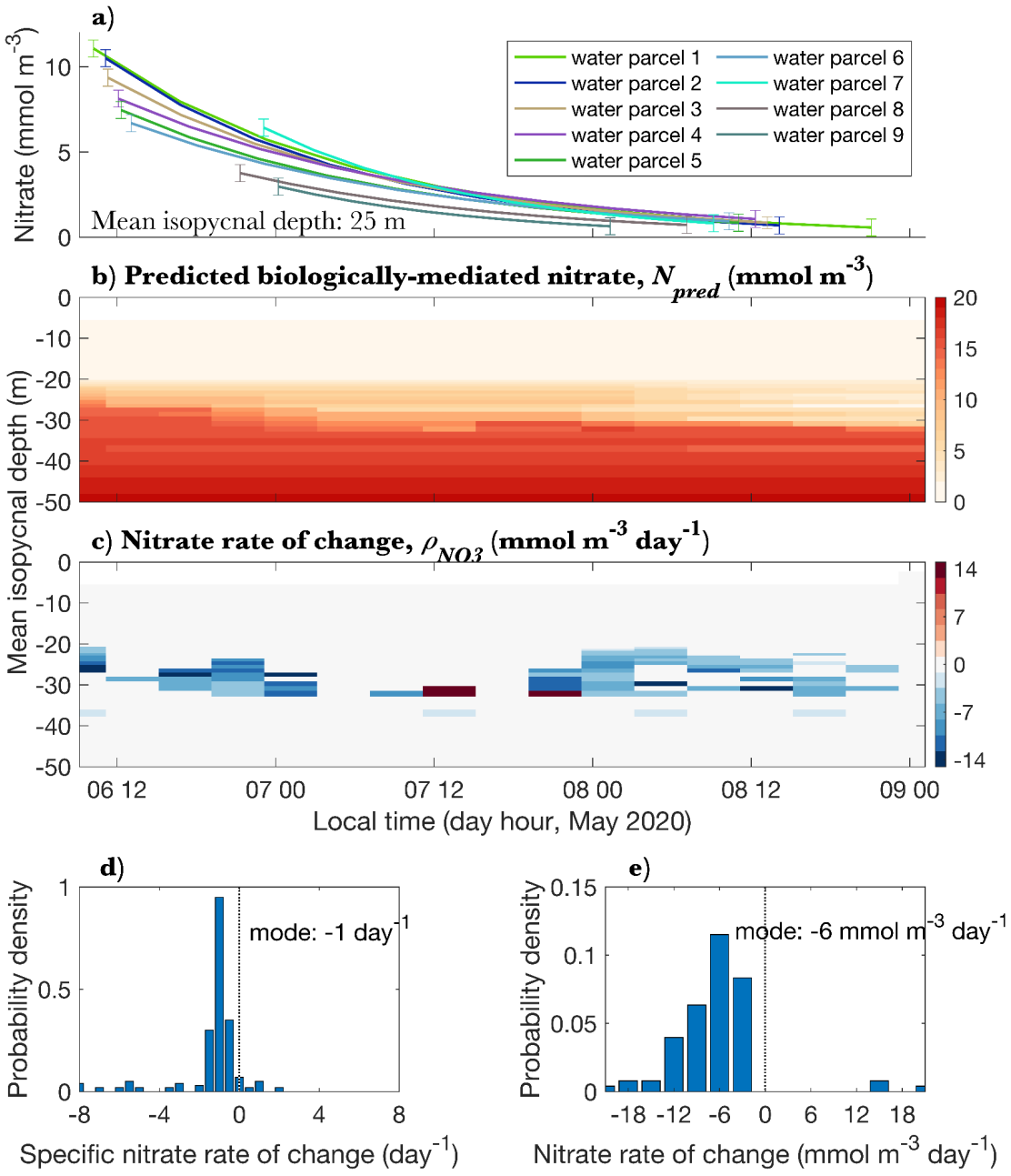

Figure 2.S8 Estimation of the nitrate rates of change. a) To estimate r, exponential curves were fit to the data points for each water parcel on an isopycnal determined by the T/S binning. b, c) The predicted nitrate field, and estimated nitrate rate of change ρ_{NO3}, respectively. d,e) The probability density functions of r and ρ_{NO3}, respectively.

To estimate the rate of change of nitrate, ρ_{NO3}, a linear differentiation in time was applied to the predicted nitrate concentrations (Fig. 2.S8b) along each isopycnal:

$$\rho_{NO3}(i) = \frac{d\,N_{pred}(i)}{dt} = \frac{N_{pred}(i)*[e^{r_{bin}(i)*\Delta t}-1]}{\Delta t}. \quad (13)$$

The associated error was estimated by:

$$\rho_{NO3,E} = \sqrt{(\frac{[e^{r_{bin}*\Delta t}-1]}{\Delta t} * N_{pred,E})^2 + (N_{pred} * e^{r_{bin}*\Delta t} * r_{bin,E})^2}. \quad (14)$$

A modal value of -6 mmol m^{-3} day^{-1} was obtained from the PDF of ρ_{NO3} (Fig. 2.S8e), which is consistent with previous literature (1 - 4 mmol m^{-3} day^{-1}: Eppley and Harrison 1975; Harrison 1976, with *L. polyedra* concentrations of 10^5 cells per liter). The estimated nitrate loss (N_{loss}) was simply obtained by integrating ρ_{NO3} in time with a zero initial value, and had the same error bars as $N_{pred,E}$. Generally, the error bars for depth integrals, E_D, can be expressed as:

$$E_D = \sqrt{\sum_{i=1}^{Q}(dz(i) * m(i))^2}\,, \quad (15)$$

where Q is the number of density layers, dz is the depth difference between each layer, and m is the error bar of the integrated variable.

In all, these approaches allow us to accurately decouple vertical and horizontal advection signals from biologically driven changes of the nitrate field -- even though we had only a single mooring and so could not directly estimate horizontal spatial gradients. The results reproduce the expected features of the data, further supporting the feasibility of this T/S binning method; this method could potentially be applied to other research problems in similar situations.

Finally, to emphasize how important it is to remove horizontal advection when estimating nitrate uptake rate, we compare the depth-integrated nitrate loss calculated from the raw observational nitrate data to the "de-advected" nitrate data (N_{pred}) (Fig. 2.S9). This comparison shows clearly that there are large excursions in nitrate concentration in the raw nitrate data (the

blue curve), which are not seen in the "de-advected" data (red line). Our calculations show that these fluctuations were driven by horizontal advection of horizontal, along-isopycnal gradients of nitrate.

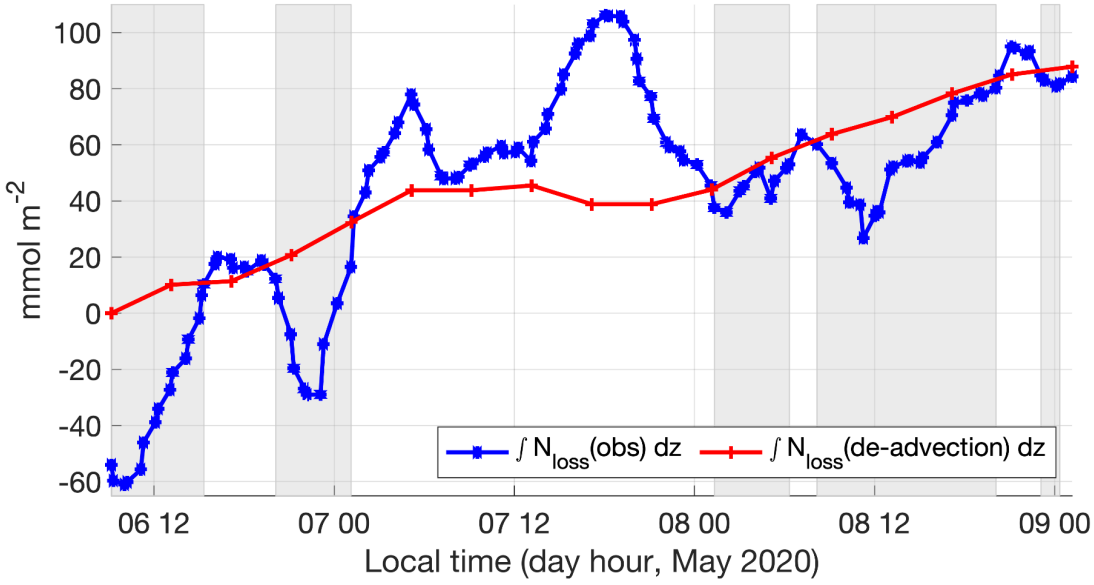

Figure 2.S9 Comparison between depth-integrated nitrate loss based on the raw observed nitrate data (blue line), and the de-advected nitrate data (red line). Grey areas represent periods when the blue line is less than the red line, indicating nitrate decreased due to advection, not biological uptake.

Chapter 2, in part, has been submitted for publication of the material as it may appear in *Proceedings of the National Academy of Sciences of the United States of America*, Zheng, B., Lucas, A.J., Franks, P.J.S., Schlosser, T., Anderson, C., Send, U., Davis, K., Barton, A. (2023). The dissertation author was the primary researcher and author of this paper.

CHAPTER 3 MULTISCALE PHYSICAL CONTROL OF CROSS-SHORE NITRATE GRADIENT OVER THE INNER CONTINENTAL SHELF

Abstract

As a crucial macronutrient for the growth and photosynthesis of phytoplankton, nitrate often limits primary productivity in the ocean. Thus characterizing nitrate dynamics and studying its constraining processes are of primary importance in advancing our understanding of oceanic ecosystem function. In this manuscript, we investigated cross-shore nitrate dynamics over multiple temporal scales, ranging from hours to days, using high-resolution physical and biogeochemical observations from three state-of-the-art moorings located in the Southern California Bight (SCB). Our findings revealed a previously undocumented onshore-directed cross-shore nitrate gradient with the highest values at the depth of the nitracline on the inshore end of the domain. We suggest that this nitrate gradient is induced by enhanced vertical nitrate flux where isopycnals intercept the turbulent bottom boundary layer (BBL). The energy for this dissipation is apparently provided by the internal wave field. Using our measurements of the time variability of nitrate, salinity, and velocity shear and stratification, we provided a constraint on the mixing rate across the nitracline in the BBL, which on average leads to an estimate of the turbulent diffusivity as approximately 2.5 - 13*10^{-4} m^2 s^{-1}. The inshore nitrate was advected offshore with a near-daily rhythm, which we suggest is induced by cross-shore advection of the recently mixed bottom boundary layer water by near-inertial waves (NIWs), which are common in the area, driven by the local diurnal sea breeze as observed. Together, these findings highlight the complex interplay of air-sea-land dynamics in modulating coastal nitrate distribution and transport, which calls attention for further in-depth observational studies as well as improvements for their representations in ecological models.

Introduction

More than 75% of the world's ocean is oligotrophic, meaning that the sunlit surface area has limited nutrient supplies to support photosynthesis by marine autotrophs (Lewis et al. 1986). Among all the limiting macronutrients, nitrate is the most common constraint on primary production (Dugdale and Goering 1967; Falkowski et al. 1998; De Baar 1994; Simpson and Sharples 2012). The primary productivity rate is ecologically important as it sets the export rate of organic carbon out of the surface euphotic layer -- a primary mechanism for the ocean to uptake carbon dioxide (Lewis et al. 1986; Guidi et al. 2016). Consequently, understanding the dynamics of nitrate, including its source, distribution, and the interplay between physical and biochemical processes, is essential to address many fundamental oceanic problems such as characterizing local primary productivity (Lucas et al. 2011), studying the dynamics of harmful algal blooms (Zheng et al. 2023), and predicting future climate (Lewis et al. 1986).

Coastal California, especially the Southern California Bight (SCB), has a narrow continental shelf with relatively high biological productivity (Smith and Eppley 1982; Lucas et al. 2011). This productivity has been suggested to be controlled by the supply of nitrate to the sunlit euphotic zone (Moberg 1928; Eppley et al. 1979). The nitrate delivery pathway contains many physical processes, including wind-driven upwelling (e.g., Wilkerson and Dugdale 1987; Roemmich 1989), internal-tide-driven cross-shore nitrate flux (Lucas et al. 2011), and vertical turbulent flux at the nitracline (e.g., Li et al. 2012). Furthermore, anthropogenic nitrate input was suggested to drive increased biological productivity both in the observational study (Howard et al. 2014) and numerical model (Kessouri et al. 2021). Recent research has shown that the nitrate field in the SCB is subject to multi-spatial-temporal scale forcings, including inter-annual climate

variabilities (e.g., El Nino, Lilly et al. 2019a) and weekly events (e.g., harmful algal bloom, Zheng et al. 2023), which have a direct impact on local primary productivity.

Although previous research has significantly advanced our understanding of the ecological role and importance of nitrate in coastal areas, there is a surprising lack of studies quantifying cross-shore nitrate gradients and understanding associated interplays between physical and biogeochemical mechanisms over the continental shelf of the SCB. This lack of information hinders our understanding of coastal nitrate dynamics and the accuracy of relevant prediction models. Conducting field observations presents a major challenge, primarily due to several complicating factors. These factors include the need for concurrent *in situ* measurements of biological, physical, nutrient, and light conditions, the need for those data to have horizontal spatial coverage, and the requirement for those data to be collected with adequate resolution in time and vertical space.

To better understand the relationship between biogeochemical patterns and physical processes in cross-shore nitrate transport, our project aims to quantify the cross-shore nitrate gradient and explore the factors that influence it. To achieve this, we deployed a Wirewalker wave-powered profiling mooring off the coast of San Diego, California during the winter of 2020-2021 (see Fig. 3.1). This advanced system provided comprehensive data, including full-depth profiles of light, nitrate concentration, Chlorophyll fluorescence and optical backscatter, temperature, salinity, and density, every 5 minutes for a period of two months, with a vertical resolution of 1 meter (see Method for more information).

Combining data from the Wirewalker with measurements from a nearby long-term deep water mooring (the Del Mar mooring) and a shallow water mooring (the Mini mooring) equipped with full-depth fixed temperature sensors and a nitrate sensor at 20 meters depth (see Fig. 3.1 and

Method for more information), we were able to quantify an along-isopycnal cross-shore nitrate gradient and analyze its dynamics associated with both physical and biogeochemical processes.

In what following, we uncover an onshore-directed cross-shore nitrate gradient that extends along the isopycnals. The amplitude of this gradient is approximately 0.75 mmol m^{-3} km^{-1}. We find that this nitrate gradient emerged temporally in correlation with a downwelling event that pushed the previously near-surface isopycnal into the bottom boundary layer on the onshore side. Subsequently, the on-isopycnal nitrate increased. As a result, nitrate appeared on isotherms/isopycnals that previously had undetectable nitrate concentrations. During this time, the wind reached its peak, and the dominant velocity pattern in the water column changed from M2 internal tides to near-inertial waves. These near-inertial waves transported nitrate along the isopycnals between onshore and offshore at a frequency of approximately 1 cpd, providing a new scenario in which the onshore region can serve as a nitrate source to fuel offshore primary productivity. These observations not only reveal and quantify a previously undocumented cross-shore nitrate gradient but also demonstrate the role of wind-driven near-inertial waves in nitrate transport across the inner shelf of SCB. It is clear that the nitrate field over the shallow continental shelf is subject to be modulated by multiscale physical forcings that involve complex air-sea-land interactions, which have both direct and indirect impacts on the local phytoplankton community.

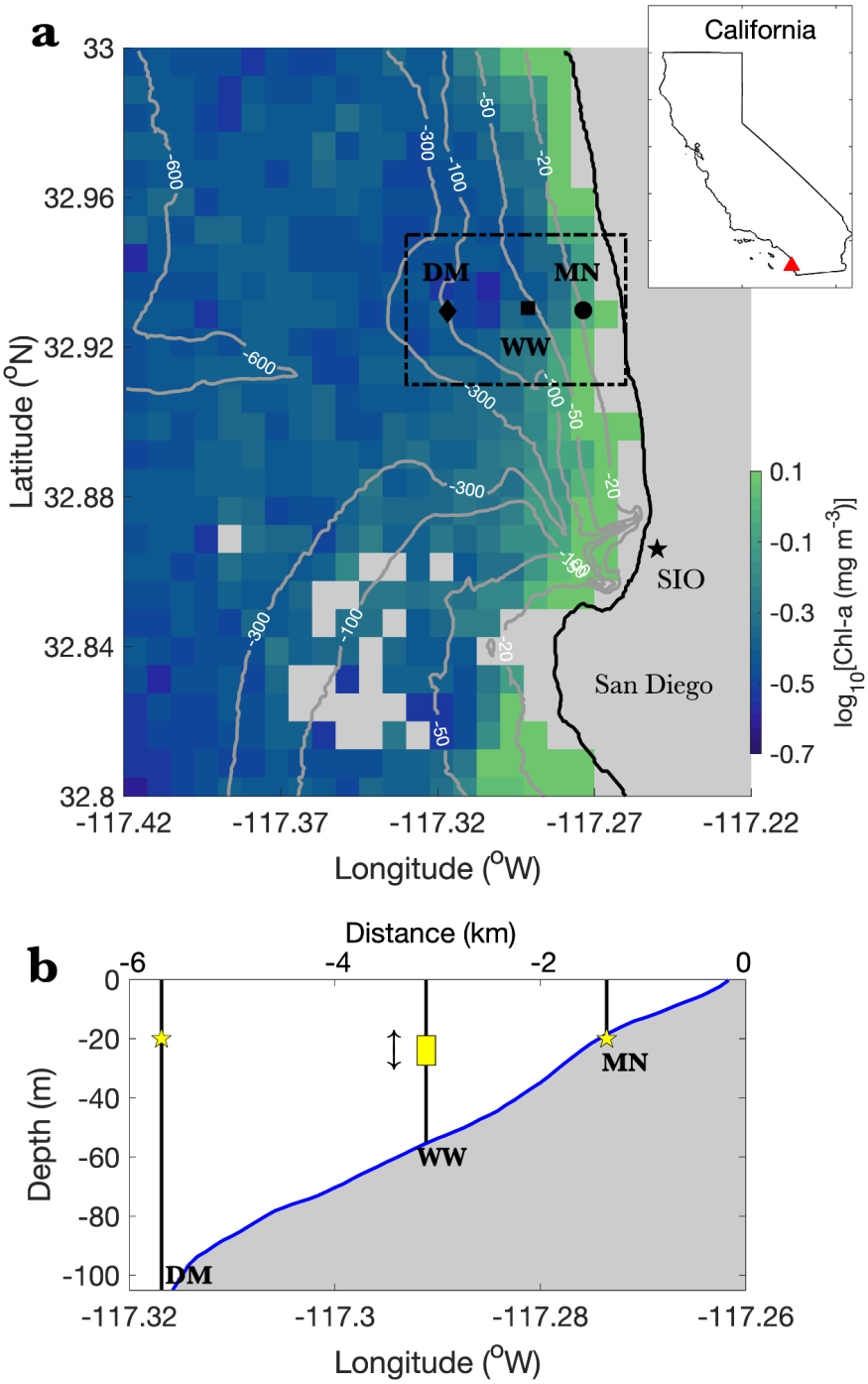

Figure 3.1 Deployment map. a) Visible Infrared Imaging Radiometer Suite (VIIRS) 1-day composite satellite sea surface Chlorophyll-a (Chl-a) at San Diego coast (corresponding to the red triangle in the upper right insert panel) on Nov. 25, 2020. The Del Mar mooring (DM), the Wirewalker (WW), and the Mini mooring (MN) are marked by the black diamond, the black square, and the black circle, respectively. Grey lines are bathymetry contours. b) Cross-shore view of the three moorings, with two fixed-depth SUNAs marked by the yellow pentagrams, and one profile SUNA on the Wirewalker platform.

Methods

Mooring setups

To collect high-spatial-temporal-resolution physical and biogeochemical data, we deployed two full-water-column moorings: the Wirewalker profiler and the Mini mooring. These two moorings were positioned inshore of a long-term coastal mooring known as the Del Mar mooring, with an approximate 2 km separation among them in the cross-shore direction (Fig. 3.1). The Del Mar mooring (DM) was located on the most offshore end of the morning line and is maintained by the Ocean Time-Series Group at the Scripps Institution of Oceanography. Equipped with a down-looking acoustic Doppler current profiler (ADCP), nine fixed-depth conductivity-temperature-depth sensors (CTDs), a fixed-depth Submersible Ultraviolet Nitrate Analyzer (SUNA) nitrate sensor (at 20 m), two Chlorophyll-a fluorescence sensors, and three oxygen sensors, the DM was a full water column physical-biogeochemical mooring. The middle mooring, the Wirewalker (WW), was an ocean wave-powered autonomous profiler that collected high-resolution upper-ocean physical and biogeochemical properties (Rainville and Pinkel 2001; Pinkel et al. 2011; Lucas et al. 2017). For this project, the WW was equipped with a CTD, SUNA nitrate sensor, Chlorophyll-a fluorescence and optical backscatter sensor, and irradiance sensor. Due to power considerations, SUNA was configured to sample on a duty cycle of 25 minutes per hour with a 1 Hz sampling frequency. All other variables were continuously sampled at 4 Hz. The gridded WW data had a temporal and vertical resolution of approximately 5.6 minutes per profile and 1 m, respectively, as determined by the vertical speed of the WW and the sampling rate of SUNA. The most inshore mooring, the Mini mooring (MN), was equipped with a CTD on the ocean surface, nine temperature sensors spanning from near surface to the bottom, a SUNA, and an up-looking ADCP on the seafloor. Both SUNAs on the DM and the MN were configured to

have a duty cycle of 1 minute per half an hour with a 1 Hz sampling rate. Fig. 3.1 shows the positions of the three moorings at 100 m, 50 m, and 20 m isobaths, respectively.

Nitrate data quality control

Quality control procedures for raw nitrate data are developed separately for the fixed-depth and profiling SUNAs.

For the fixed-depth SUNA, we followed the nitrate quality control procedures in Lilly et al. (2019). After loading raw nitrate data (Fig. 3.2a), we excluded outliers and took the median value within each duty cycle to achieve statistical liability (Fig. 3.2b). Next, we removed the sensor drift by subtracting a baseline that was determined along the lower edge of the nitrate time series (Fig. 3.2cd). This baseline can often be non-linear. Finally, the baseline-corrected nitrate data were compared to the calibration curves obtained from the pre-deployment and post-deployment laboratory casts to check sensor accuracy. Additional adjustments were applied if there were obvious discrepancies between the corrected data and the calibrations.

For the profiling SUNA, the nitrate quality control procedures were almost the same as those for the fixed-depth SUNA, except that there was no median value selection within each duty cycle due to the fact that the vertical location of the profiling SUNA was constantly changing. More details on nitrate quality control for the profiling SUNA can be found in Zheng et al. (2023).

The associated error bar was estimated by calculating the 95% confidence interval (2 standard deviations) of raw nitrate data within a 0.5 ^{o}C temperature range.

Overall, these procedures represent our best attempt to calibrate SUNAs. Thus the remaining difference in nitrate signals across different sensors are believed to be independent of the sensor's cross-calibration issues.

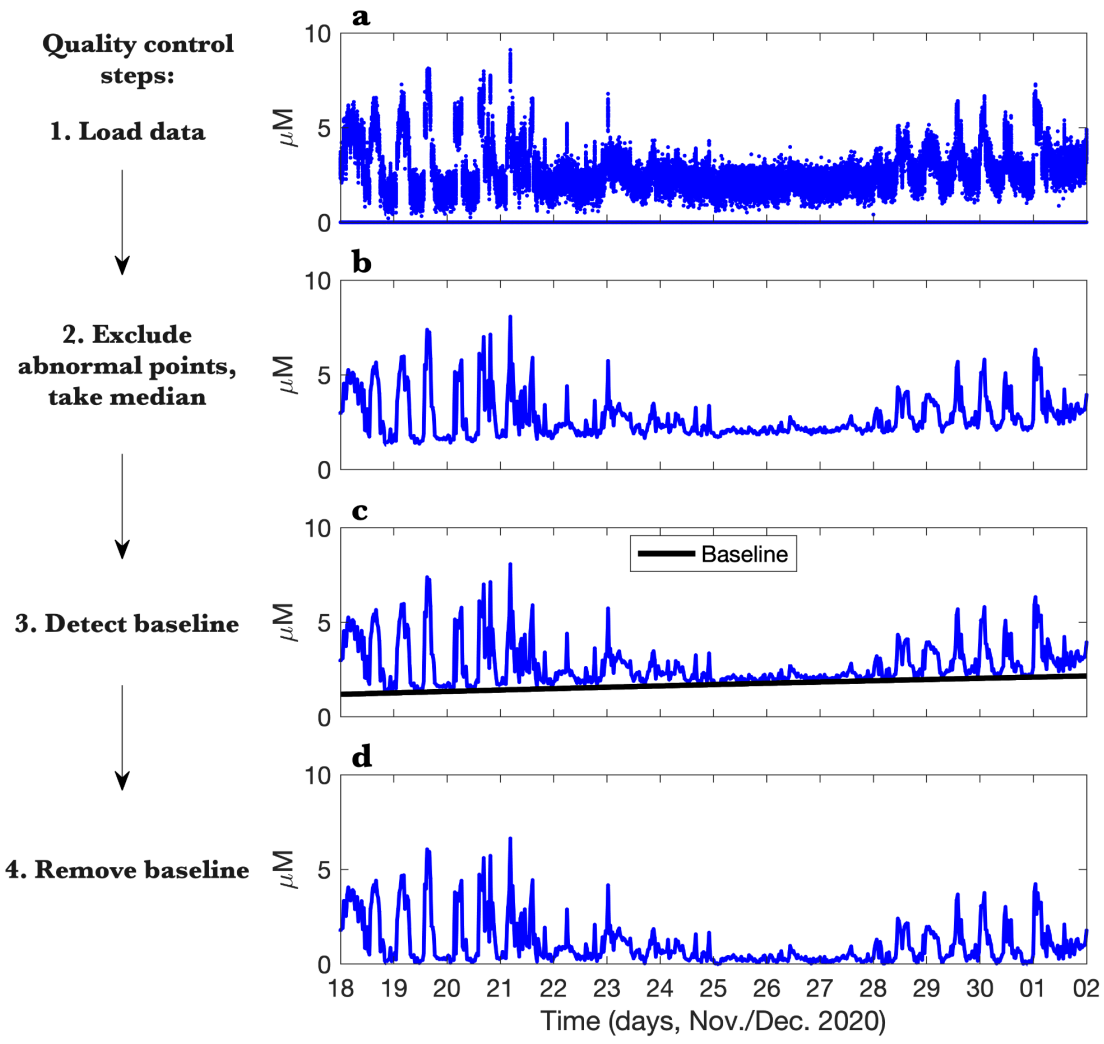

Figure 3.2 Quality control procedures for fixed-depth SUNA.

Depth-to-isopycnal coordinate transformation

This coordinate transformation was performed by interpolating raw physical and biogeochemical data (as a function of pressure) from each WW profile onto uniformly-gridded density bins (here, the density interval was set to be 0.02 kg m^{-3}). Likewise, interpolating raw pressure measurements provided instantaneous depths of uniformly-gridded density bins for each WW profile. To resemble the different vertical spacings between isopycnals (in other words, stratification) in the raw data, we plotted the converted along-isopycnal variables as a function of

mean isopycnal depth, which was calculated as the time-averaged interpolated pressure value for each density bin over the study period.

Turbulent diffusivity parameterizations

Following the Osborn-Cox parameterization (Osborn 1980), a balance of turbulent kinetic energy (TKE) between shear production, buoyancy production, and energy dissipation by viscous friction (ε), leads to an estimation of diffusivity (K_z), $K_z = \Gamma(\varepsilon/N^2)$, where, Γ is the constant mixing efficiency, taken as 0.2, and N^2 is the time-averaged buoyancy frequency. Here, we applied a parameterization method, the MacKinnon-Gregg (MG) parameterization (MacKinnon and Gregg 2005), to estimate ε and subsequently obtain K_z. The overarching idea behind this method is assuming that the turbulent dissipation rate was controlled by wave-wave interaction processes, which can be scaled as: $\varepsilon_{MG} = \varepsilon_0 \frac{S}{S_0} \frac{N}{N_0}$, where S and N are low-frequency, low-mode shear, and stratification respectively, $S_0 = N_0 = 3$ cph, and ε_0 = 1.1*10^{-9} W kg^{-1}. The feasibility of this method in quantifying the turbulent parameters has been tested in multiple locations (e.g., the New England Shelf in MacKinnon and Gregg 2005; the SCB, Omand et al. 2012).

Progressive vector diagram (PVD)

Progressive vector diagram calculation takes the point measurements of the velocity time series as inputs and then backtracks the particle trajectories (e.g., Carlson et al. 2010). One major assumption is that the velocity field is spatially uniform at one depth over the study domain and period, and hence PVD works better when the horizontal shear is small. The equation is:

$$X(i+1) = X(i) - U(i) * \Delta t, \quad (1)$$

where, X represents particle location, U represents velocity, Δt is the time difference between points, and i is the index. When the time series of the corresponding tracer is available, PVD can produce an estimated spatial pattern of the tracer.

Errors associated with the spatial separation between nitrate data and velocity data

The PVD-estimated spatial gradient of the tracer possibly contains errors when velocity data and the corresponding tracer are from two spatially-separated locations, for example, DM and WW. This error can come from spatial variations in the velocity field. To quantify this error, we estimated the velocity difference at the Del Mar mooring (U_{DM}) and the Wirewalker (U_{WW}). Following a 2-D linear internal wave theory, the velocity is formulated as:

$$u(x,z,t) = A_{max}\psi(z)sin(kx - \omega t), \tag{2}$$

where, A_{max} is maximum velocity amplitude in $m\,s^{-1}$, $\psi(z)$ represents a vertical structure function, dimensionless, varying between 0 and 1, k and ω are the horizontal wavenumber and wave dominant frequency, in units of m^{-1} and s^{-1}, respectively. k and ω are connected by the dispersion relationship:

$$\omega^2 = f^2 + \frac{N^2k^2}{m^2}, \tag{3}$$

where, N is the buoyancy frequency, m is the vertical wavenumber. k of $1.5 * 10^{-4}\,m^{-1}$ is obtained, with inputs from a combination of realistic parameters and a mode 3 vertical structure, based on hydrographic observations from the WW ($\omega = 0.807 * 10^{-4}\,s^{-1}$, $f = 0.792 * 10^{-4}\,s^{-1}$, $m = 0.0942\,m^{-1}$, and $N = 10^{-2}\,s^{-1}$). This estimated horizontal wavenumber, along with the 2 km spatial separation between the Del Mar mooring and the Wirewalker, leads to a 0.2 $rads$ (root mean square value) phase difference between U_{DM} and U_{WW}, and thus an average ~20% error when using U_{DM} to represent U_{WW}. Following the standard error propagation procedures (e.g., Taylor 1997), the error in velocity leads to an error in the PVD-estimated particle track, which can be expressed as:

$$\delta X(i+1) = \sqrt{(\delta X(i))^2 + (\Delta t * U(i) * 0.21)^2}, \tag{4}$$

where, $\delta X(i)$ is the error for the i-th particle position, and 0.21 is the percentage error calculated above.

Results

During the two-week observation period, the CTD measurements showed significant spatial and temporal hydrographic variability of the subsurface water column. Besides the persistent internal waves, there was an evident event of isopycnal-deepening (later referred to as "downwelling") whereby a warm and salty water mass gradually displaced the surface water mass (with an inshore propagation speed of approximately 2 km per day) and caused the previously surfaced isopycnal to deepen by approximately 10-20 m (as shown in Fig. 3.3). The downwelling was consistent in the cross-shore direction, as seen from the similar temperature pattern across different panels in Fig. 3.3. After four days of development (from November 22 to November 26), the downwelling relaxed, with isopycnals gradually returning to their initial positions (as illustrated in Fig. 3.3). Notably, for the Mini mooring, a previously near-surface density layer (bounded by σ_0 24.6 and 24.84 kg m^{-3}, indicated by black lines in Fig. 3.3c) gradually approached the bottom boundary layer and reached the sea floor, resulting in a decrease in density at the sea floor. Since the water column in the SCB was strongly temperature-stratified (with modest vertical salinity variations) during the sampling period, there was a corresponding increase in near-bottom temperature by approximately 2 ^{o}C, with isotherm layers between 13.5 ^{o}C and 15.5 ^{o}C consistently intercepting the sea floor at the Mini mooring during the downwelling (after approximately November 23, as depicted in Fig. 3.3d). These isotherm layers were estimated to run-up and run-down a distance of approximately 700 m (1400 m in total) along the sloping sea floor -- nearly half the distance from the Mini mooring to the coast -- every 12 hours, driven by energetic internal waves.

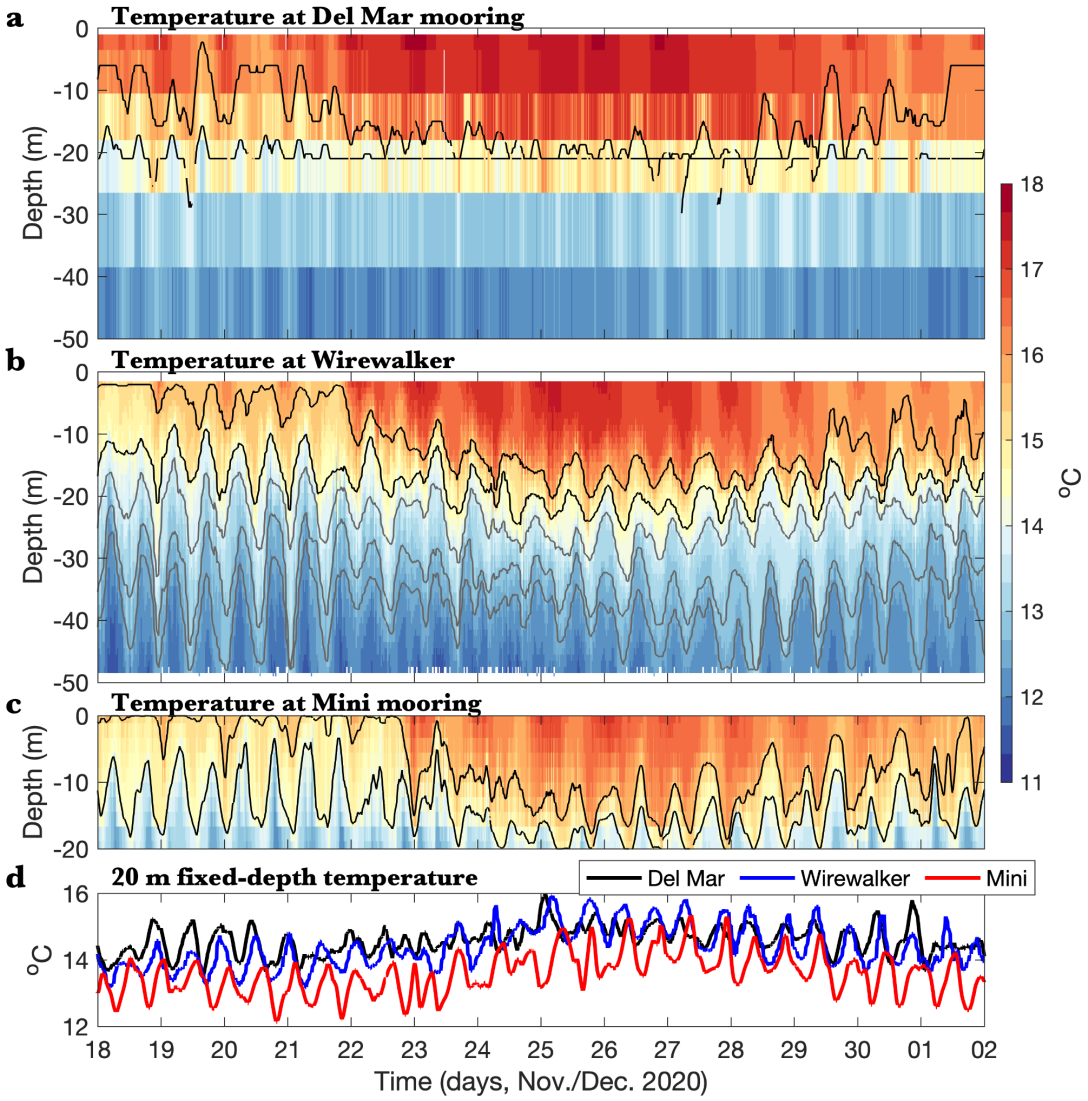

Figure 3.3 Subsurface temperature measurements at the Del Mar mooring (a), Wirewalker (b), and Mini mooring (c), respectively. Contour lines in each panel are isopycnals, with σ_0 values of 24.6 kg m^{-3} (black), 24.84 kg m^{-3} (black), 25 kg m^{-3} (grey), 25.2 kg m^{-3} (grey), and 25.4 kg m^{-3} (grey), respectively. d) temperature time series at 20 m depth from three moorings.

The downwelling also altered the biogeochemical properties of the water column, as shown in Fig. 3.4. The phytoplankton community deepened from the surface 0-15 m to the subsurface 12-22 m, forming a subsurface chlorophyll (Chl-a) maximum layer that followed the vertical isopycnal motions. A decrease in Chl-a concentration over time was observed. Similarly, the

nitracline (proxied by the 24.84 kg m^{-3} isopycnal, the deeper black solid line in Fig. 3.4bc) moved down by a few meters, accompanied by an increase in nitrate above the previous nitracline after the onset of the downwelling (Fig. 3.4c). At a fixed depth of 20 m, the nitrate records showed a consistent decrease in amplitude after the initiation of the downwelling and a gradual increase after the downwelling relaxed (Fig. 3.4d). Overall, the nitrate concentration was higher onshore at 20 m over the two-week observation period.

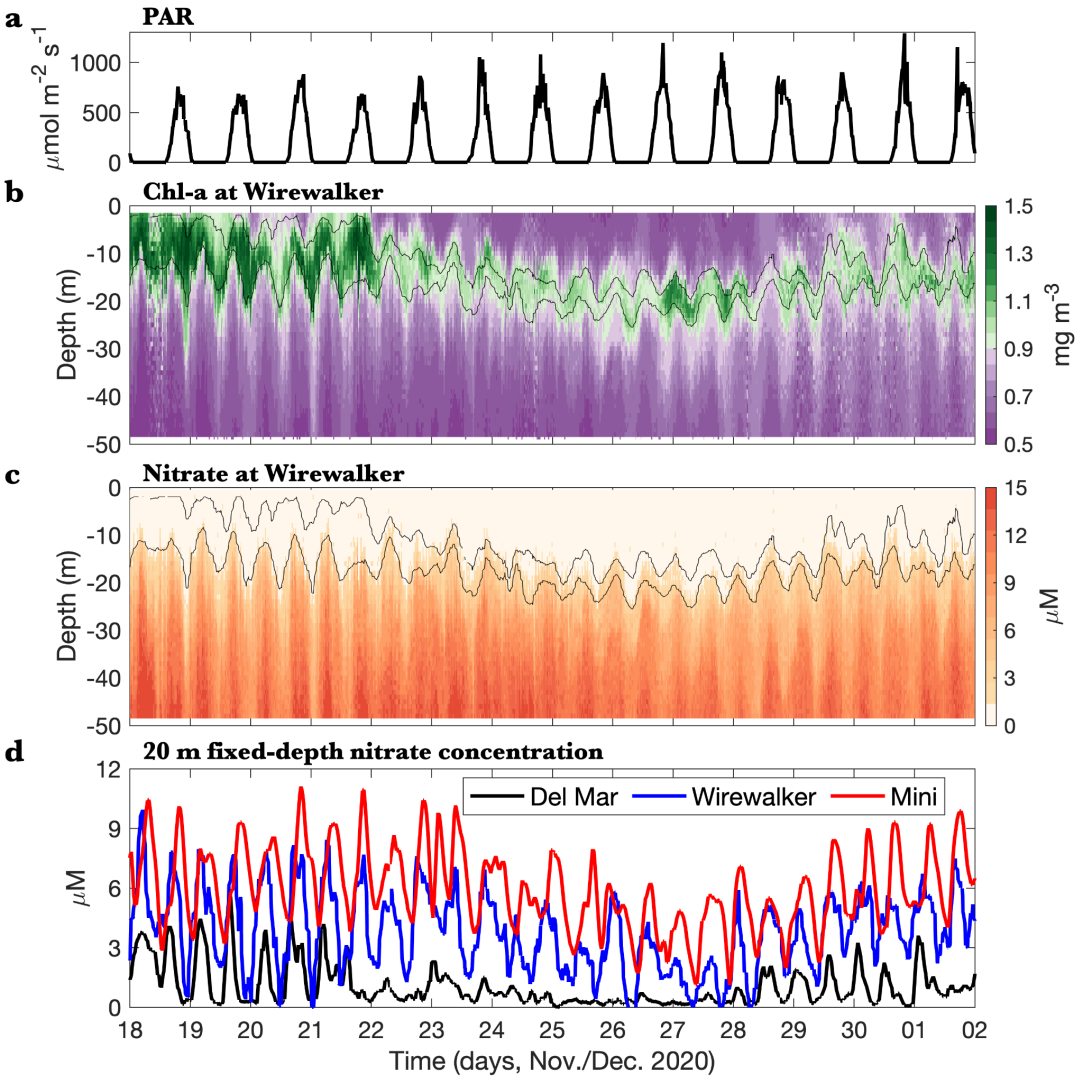

Figure 3.4 Biogeochemical observations. a,b,c) surface 2-m averaged PAR, Chl-a concentration, and nitrate concentration measured by the Wirewalker, respectively. Contour lines in b,c are isopycnals with σ_0 values of 24.6 and 24.84 kg m^{-3}. d) nitrate time series at 20 m depth from three moorings.

To distinguish between variability due to vertical isopycnal excursions induced by internal waves and downwelling from those that develop on-isopycnal, a depth-to-isopycnal coordinate transformation was applied to all physical and biogeochemical variables (see Methods). Here we focus on a specific isopycnal layer -- σ_0 24.6 kg m^{-3} to 24.84 kg m^{-3}, representing a temperature range from 14.5 ^oC to 15.6 ^oC. This layer is of biochemical significance because it contains most of the phytoplankton community in the water column (Fig. 3.4b) and is right above the previous nitracline (Fig. 3.4c), allowing us to characterize nitrate changes in the surface mixed layer before and after the downwelling.

The along-isopycnal Chl-a decreased by approximately 30%, accompanied by a corresponding decrease of about 30% in photosynthetically available radiation (PAR)(Fig. 3.5ab). On the other hand, along-isopycnal nitrate concentration, measured by the WW, increased from statistically undetectable to detectable after Nov. 22 and then gradually decreased after Nov. 26 (Fig. 3.5c), partially in phase with the development and relaxation of the downwelling (Fig. 3.3). Although the along-isopycnal Mini mooring and Del Mar mooring nitrate measurements were sometimes discontinuous due to the isopycnal layer not always appearing at fixed sensor locations, they showed consistent temporal evolutions bounding the upper and lower limits of the WW nitrate data, respectively. On average, a cross-shore along-isopycnal nitrate gradient of approximately 0.75 mmol N m^{-3} km^{-1} is estimated, increasing onshore during the persistence of the downwelling, which lasted several days. On a shorter timescale, WW along-isopycnal nitrate data showed an oscillating signal at a frequency of approximately 1 cpd from Nov. 22 to Nov. 28 (Fig. 3.5c). These observations reveal a highly dynamic nitrate field that evolves on multiple temporal scales ranging from hours to days.

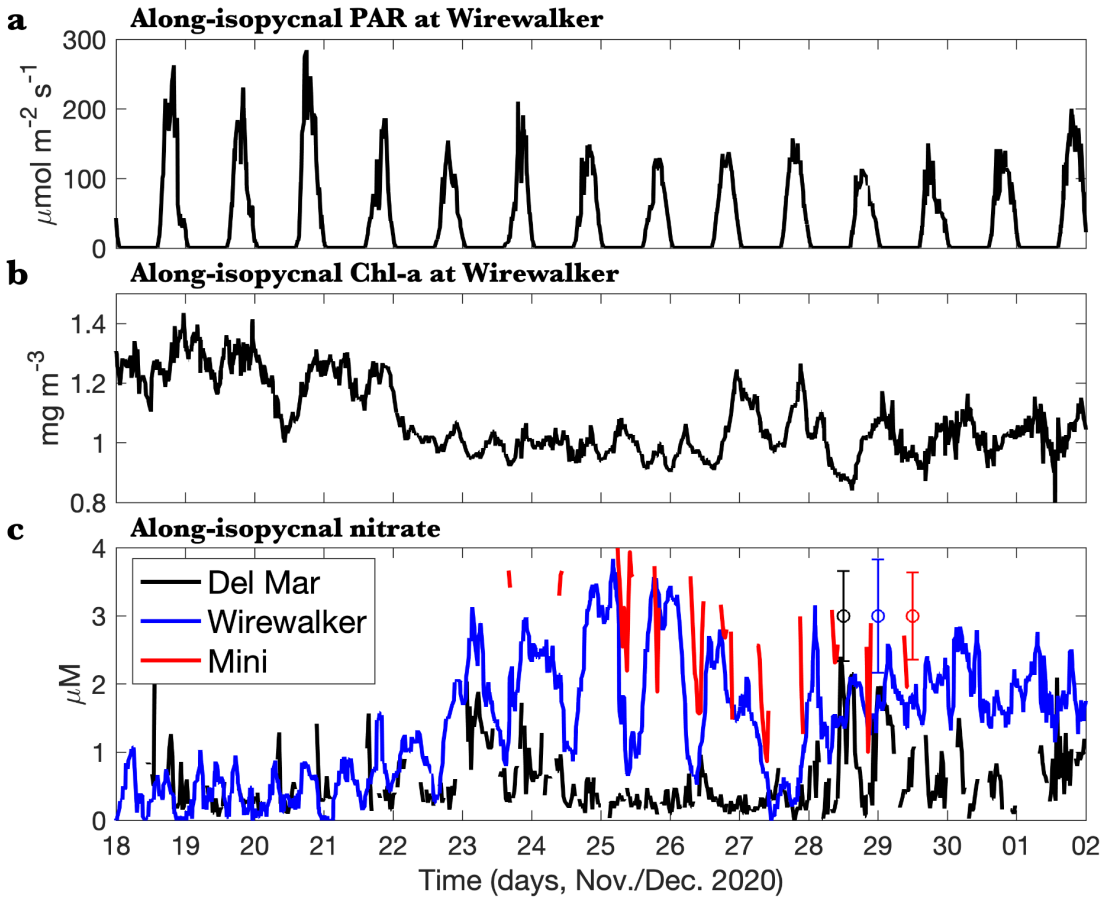

Figure 3.5 Along-isopycnal biogeochemical properties. a,b,c) depth-averaged PAR, Chl-a concentration, and nitrate concentration in the density layer between σ_0 24.6 kg m^{-3} and 24.84 kg m^{-3}, respectively. Error bars associated with each nitrate product were denoted in c. Note that the black line and the red line in c are partially discrete since this density layer might not always occur at the fixed location (20 m depth).

The nitrate-temperature (N-T) relationship is a valuable statistical tool to assess the distribution of nitrate in the water column. A consistent and stable N-T relationship was observed among all three moorings before the downwelling event, with nitrate concentration negatively correlated with temperature below 14.5 ºC and nearly undetectable above it (Fig. 3.6a). This pattern is consistent with the typical N-T relationship in the SCB under normal conditions, as reported in previous studies (Eppley 1992; McPhee-Shaw et al. 2007; Lucas et al. 2011). However, during the onset and persistence of the downwelling, a significant increase in nitrate concentration,

up to 4 mmol N m^{-3}, was detected at isotherms ranging from approximately 14 ºC to almost 16 ºC at the two onshore moorings (i.e., Mini mooring and Wirewalker) (Fig. 3.6b). This rise in nitrate is highly unusual as nitrate concentration above 14.5 ºC is typically close to zero in the SCB (Eppley et al. 1979; Lucas et al. 2011). Furthermore, it is important to note that the offshore mooring (i.e., Del Mar mooring) showed no significant increase in nitrate concentration irrespective of the evolution of the downwelling (Fig. 3.6b).

The Temperature-Salinity (T-S) relationship also shows a change associated with the downwelling, whereby a relatively linear curve replaced the previous bending curve at a T/S region, i.e., temperature from ~14 ºC to ~15.5 ºC and salinity from ~33.53 psu to 33.56 psu (Fig. 3.7). Note that the temperature range where both N-T and T-S relationships changed after the downwelling (i.e., from ~14 ºC to ~15.5 ºC) aligns with the measured temperature range on the sea floor at the Mini mooring (Fig. 3.3d), emphasizing near-bottom processes as potential agents for these changes.

With available observational data, the vertical turbulent diffusivity (K_z) was estimated via three independent approaches. First, we used the advection-diffusion equation for nitrate to quantify K_z.

$$\frac{\partial n}{\partial t} + \boldsymbol{v} \cdot \nabla \boldsymbol{n} = K_z \frac{\partial^2 n}{\partial z^2} + K_x \frac{\partial^2 n}{\partial x^2} + K_y \frac{\partial^2 n}{\partial y^2} - Bio, \tag{5}$$

where, $\boldsymbol{n}$ is nitrate concentration, $\boldsymbol{v}$ is velocity vector, K_x and K_y are two horizontal turbulent diffusivities, and Bio represents nitrate loss due to biological uptake. Assuming that horizontal diffusion is negligible (e.g., Eppley et al. 1979), averaging across multiple days would minimize advection signal, and biological uptake is ignored, Eq.5 can be further simplified as:

$$\frac{\partial n}{\partial t} = K_z \frac{\partial^2 n}{\partial z^2}. \tag{6}$$

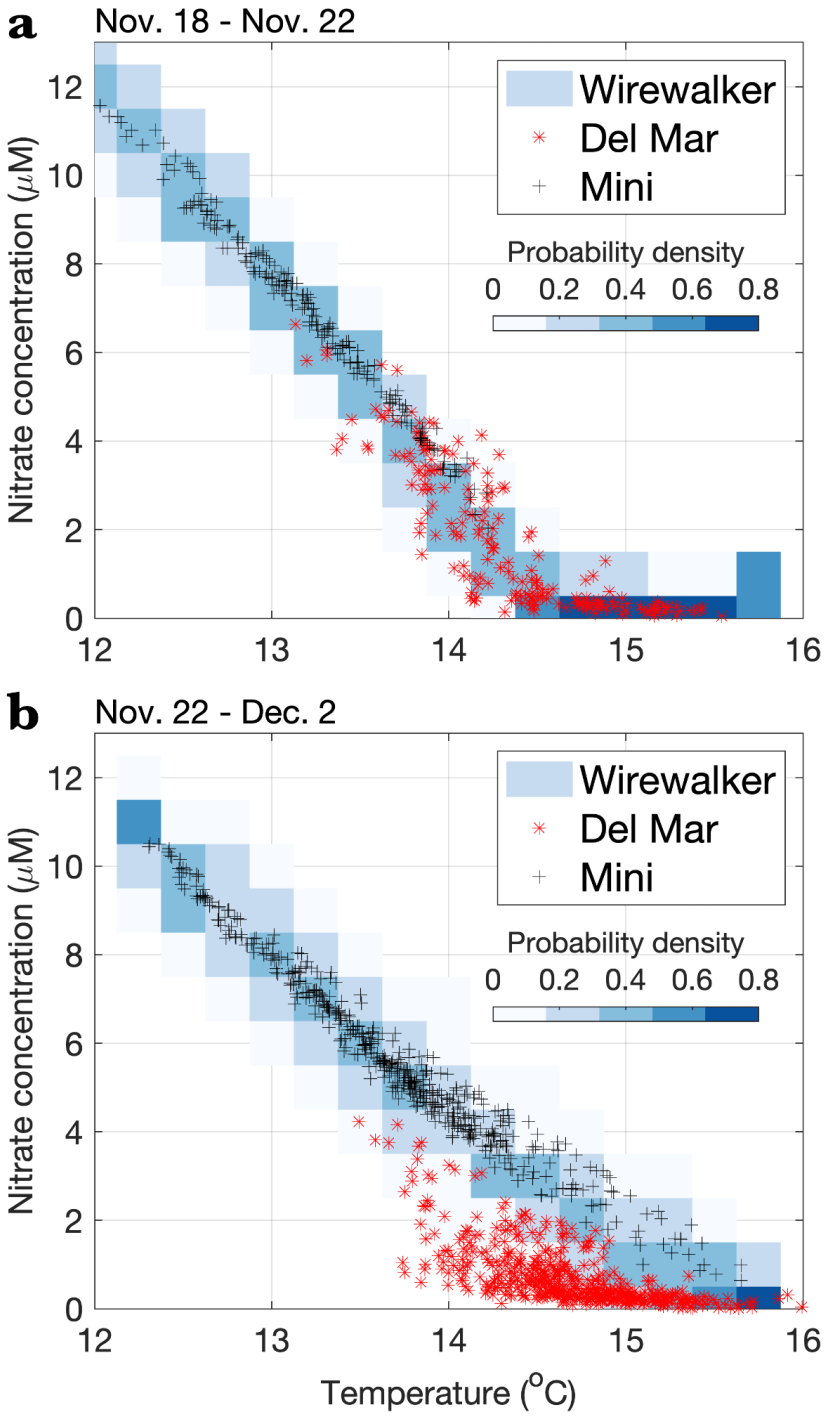

Figure 3.6 Nitrate-temperature (N-T) relationship before (a) and during (b) the downwelling at three moorings. The Wirewalker records were plotted as the combined probability density function (PDF) of nitrate for each 0.25 ºC temperature bin.

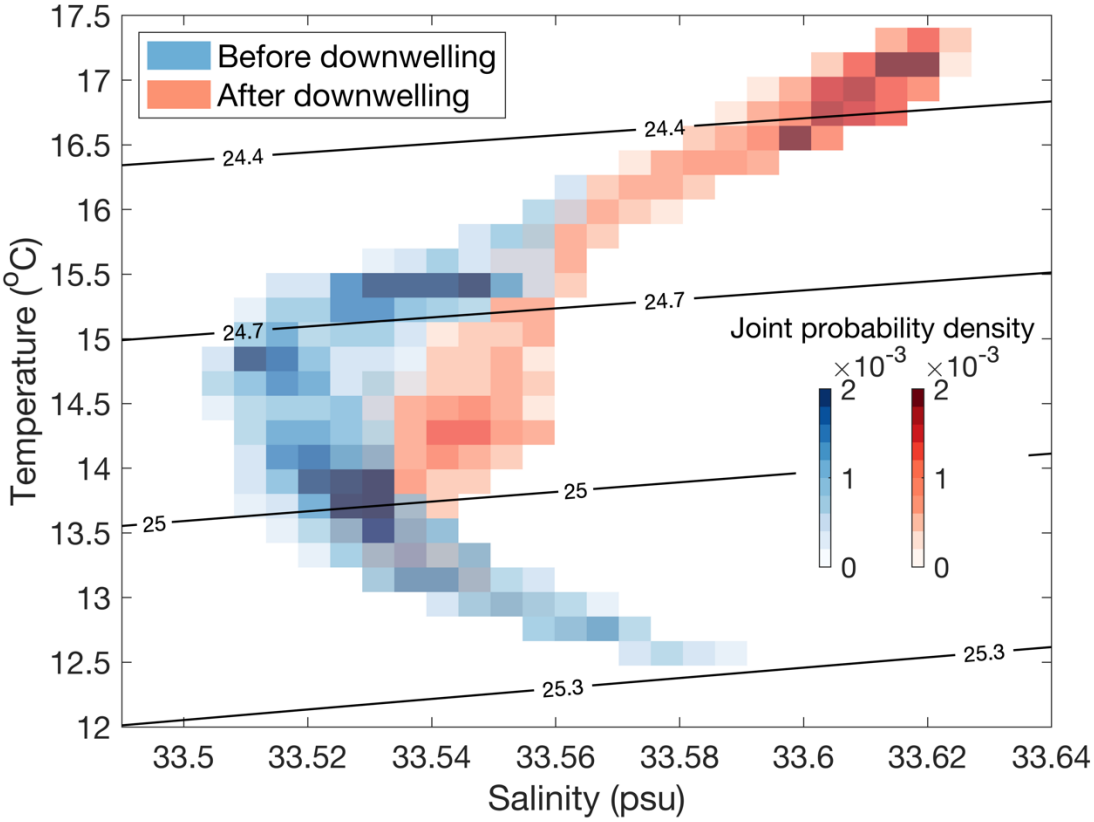

Figure 3.7 Temperature-Salinity relationship with data from the Wirewalker (upper 30 m) before the downwelling (Nov. 18 - Nov. 22) and after the downwelling (Nov. 22 - Nov. 27). Contour lines show σ_0 values.

From Nov. 22 to Nov. 27, we quantified the time-averaged temporal nitrate gradient ($\partial n/\partial t$), the vertical nitrate gradient ($\partial n/\partial z$), and the layer depth (dz) of the density layer (σ_0) between 24.6 kg m^{-3} and 24.94 kg m^{-3} (corresponding to a temperature region between 14 °C and 15.5 °C). An average K_z of 2.5*10^{-4} m^2 s^{-1} is obtained. Second, we used the advection-diffusion equation for salinity to quantify K_z:

$$\frac{\partial S}{\partial t} + \boldsymbol{v} \cdot \nabla \boldsymbol{s} = K_z \frac{\partial^2 S}{\partial z^2} + K_x \frac{\partial^2 S}{\partial x^2} + K_y \frac{\partial^2 S}{\partial y^2}, \quad (7)$$

where, s represents salinity. Again, assuming that horizontal diffusion is small and the horizontal advection signal is mostly averaged out, we can get:

$$\frac{\partial S}{\partial t} = K_z \frac{\partial^2 S}{\partial z^2}. \quad (8)$$

The estimated K_z is 5.1*10^{-4} m^2 s^{-1}, using the same density layer and time period as above. Third, the MacKinnon-Gregg diffusivity parameterization (details in Methods). Using the velocity and density records measured at the bottom of the Mini mooring from Nov. 22 to Nov. 27, an average K_z of 1.3*10^{-3} m^2 s^{-1} is obtained.

These three independent diffusivity estimations are all consistent with previous diffusivity estimations in this region (0.5-5*10^{-4} m^2 s^{-1}, Eppley et al. 1979, Lucas et al. 2011, Omand et al. 2012). Even though the MG method gives a relatively higher diffusivity value, these three quantifications are within one order of difference from each other -- justifying the reliability of the estimations.

Discussion

Through a comprehensive analysis of physical and biochemical measurements, including temperature, salinity, velocity, nitrate, Chl-a, and PAR, we identified an onshore-directed along-isopycnal cross-shore nitrate gradient over the inner continental shelf of SCB. This gradient was quantified as approximately 0.75 mmol m^{-3} km^{-1}. The appearance of this gradient coincided with changes in the hydrodynamic environment, whereby a persistent downwelling was apparent, leading to previously surfaced isopycnals intercepting the sea floor at the onshore end. Interestingly, the subsurface nitrate distribution was significantly altered at the onshore region after the onset of the downwelling. Specifically, nitrate concentrations increased by up to 4 mmol m^{-3} on isotherms above 14 ^{o}C, which is unusual as nitrate is typically undetectable in this temperature range. Moreover, a nitrate oscillation signal of approximately 1 cpd was observed at the middle mooring, with its amplitude bounded by the nitrate concentrations measured at the onshore and offshore locations. Overall, our findings highlight a highly dynamic nitrate field on

multiple temporal scales, from daily cycles to several days, and provide valuable insights into the effects of submesoscale features on the nitrate distribution in the SCB.

The nitrate source for the onshore region

In contrast to the previous findings of an offshore-directed along-isopycnal cross-shore nitrate gradient over the inner continental shelf of the SCB (Lucas et al. 2011), our study reveals a novel scenario of elevated onshore nitrate. In what follows, we provide evidence showing that the primary cause of this increase in nitrate was enhanced vertical flux due to the elevated turbulent diffusivity expected when nitrate layers encountered the bottom boundary layer (BBL), other than the terrestrial source or oceanic biochemical processes.

Terrestrial source

In coastal areas, nitrogen from land is primarily introduced into the adjacent ocean through wastewater discharge and water runoff (Lyon and Stein 2009). Recently, Sutula et al. (2021) studied terrestrial nitrogen flux from point-source wastewater treatment plants and river sources in the SCB and found that almost 97% of the terrestrial nitrogen is from wastewater effluent. This effluent is characterized by fresh and nutrient-rich water, with nitrogen concentrations reaching 30 mmol m^{-3} (Sutula et al. 2021). However, our data contradict the hypothesis of freshwater influx from land, as we observed decreased nitrate (Fig. 3.4d) and increased salinity (Fig. 3.7) at fixed depth from Nov. 23 to 28.

Water column chemical processes

An alternative hypothesis that could explain the elevated onshore nitrate is near-bottom nitrification (Ward et al. 2011; Haas et al. 2021). However, previous literature reported a near-bottom nitrification rate of only approximately 0.02-0.15 mmol m^{-3} N day^{-1} in the SCB region (Ward et al. 1982; Mclaughlin et al. 2021). This value is several to tens of times smaller than the

observed nitrate increase rate (Fig. 3.5c), suggesting that near-bottom nitrification is an unlikely explanation for the observed phenomenon.

Biological assimilation

The along-isopycnal nitrate gradient could also be influenced by biological processes, particularly the assimilation of nitrate by autotrophs. Specifically, a decrease in biomass and/or growth rate would result in a decrease in nitrate assimilation rate and, consequently, an increase in nitrate concentration, assuming that the nitrate supply rate remains constant. If biological assimilation were the primary cause of the elevated onshore nitrate, one would expect higher offshore concentrations of phytoplankton, which are responsible for nitrate assimilation. However, both satellite Chl-a images (Fig. 3.1a) and *in situ* Chl-a observations compared between the Del Mar mooring and the Wirewalker (not shown here) revealed higher phytoplankton concentrations onshore, suggesting that biological assimilation was unlikely to drive the gradients we observed.

Elevated turbulent nitrate flux in the bottom boundary layer (BBL-nitrate flux)

The elevated onshore nitrate may have also resulted from increases in nitrate supply to the isopycnal. One possible mechanism is the occurrence of a higher diapycnal turbulent nitrate flux when the isopycnal encountered the BBL -- the area where the ocean meets the topographic boundary, characterized by elevated turbulence that transports mass, energy, and momentum into the ocean interior through various physical processes (Trowbridge and Lentz 2018; Naveira Garabato et al. 2019).

Evidence of turbulent mixing came from the N-T and T-S relationship (Fig. 3.6, 7). Post-downwelling nitrate data (Fig. 3.6b) show a relatively linear distribution against temperature above ~14 ^{o}C, with boundary nitrate values consistent with those at 14 ^{o}C and 16 ^{o}C in the pre-downwelling condition (Fig. 3.6a). Additionally, the T-S property shows a similar linear change

(Fig. 3.7). This consistency and linear shape suggest active mixing between these temperature layers.

The reasonableness and consistency in the estimated turbulent diffusivity provide qualitative evidence to support the hypothesis that the change in the N-T and T-S relationship after the downwelling was induced by mixing processes, which subsequently supports the hypothesis that the elevated onshore nitrate can be supplied vertically through diapycnal diffusion processes in the BBL.

A physical model that illustrates the key points of the BBL-nitrate flux mechanism can be described as follows: flows induced by energetic internal waves periodically slosh up and down over the sloping sea floor for a distance of about 1.4 km every 12 hours. This interaction between internal waves and the sloping sea floor creates elevated near-bottom turbulence, which is responsible for the enhanced vertical nitrate flux observed in our study. This situation is similar to the numerical simulations conducted by Winters (2015). Additionally, previous studies (e.g., Alberty et al. 2017) suggest that as an isopycnal layer is strained, as shown in Fig. 3.3c, enhanced turbulent diffusion and elevated local turbulence levels may result. Similar to ocean ventilation, where nutrient-rich water is exchanged into the ocean interior through the ocean surface (e.g., Morrison et al. 2022), the BBL-nitrate flux mechanism allows for nitrate to be ventilated in the bottom of the coastal ocean, highlighting the biogeochemical importance of the bottom boundary layer over the inner continental shelf.

The spatial nitrate gradient we observed is likely to be intermittent over time. It is possible that other downwelling-related physical processes, such as eddies and fronts, could also cause on-isopycnal nitrate increases similar to what we observed if they interact with the BBL. Therefore,

the nitrate field over the shallow continental shelf may be more dynamically complex in space and time than previously reported.

Along-isopycnal cross-shore nitrate transport by near-inertial waves

Previous studies (e.g., Johnson 2010; Sakamoto et al. 2017) have reported diel nitrate cycles characterized by a decrease in nitrate during the daytime due to biological uptake by phytoplankton and an increase at night through physical nitrate supply. However, our observations (Fig. 3.5ac) revealed an opposite pattern where nitrate increased during the daytime. This pattern suggests that biological activity was not the primary driver of the ~1 cpd nitrate signal we observed.

Along-shore advection of nitrate is presumably not the reason for the observed ~1 cpd nitrate oscillation. The mean subtidal along-shore current was ~0.07 m s^{-1} from Nov. 22 to Nov. 27 (Fig. 3.8d). This mean flow leads to a net along-shore transportation distance of ~6 km per day. Thus, a periodic along-shore nitrate gradient with a spatial separation scale of 6 km must be present to match the observed nitrate oscillations. However, we can not see this periodicity in the surface nitrate field, when using satellite-measured sea surface temperature as a proxy for nitrate in the SCB.

Instead, we propose the NIW-advection hypothesis, whereby the ~1 cpd nitrate signal was primarily induced by the advection of the cross-shore nitrate gradient via near-inertial internal waves.

To test the NIW-advection hypothesis, the first step is to determine whether the oceanic velocity frequency matches the frequency observed in the nitrate record (~1 cpd). We performed wavelet analysis on the along-isopycnal velocity time series collected by the Del Mar Mooring (Fig. 3.8cd) and found that the dominant frequency of the velocity changed from ~2 cpd to ~1 cpd

on Nov. 22 and remained at ~1 cpd for the rest of the sampling period. This 1 cpd frequency not only indicates a direct correlation between the velocity and the nitrate record but also corresponds to the inertial frequency (f) at the mooring location --1.09 cpd. These findings provide the initial evidence supporting the NIW-advection hypothesis.

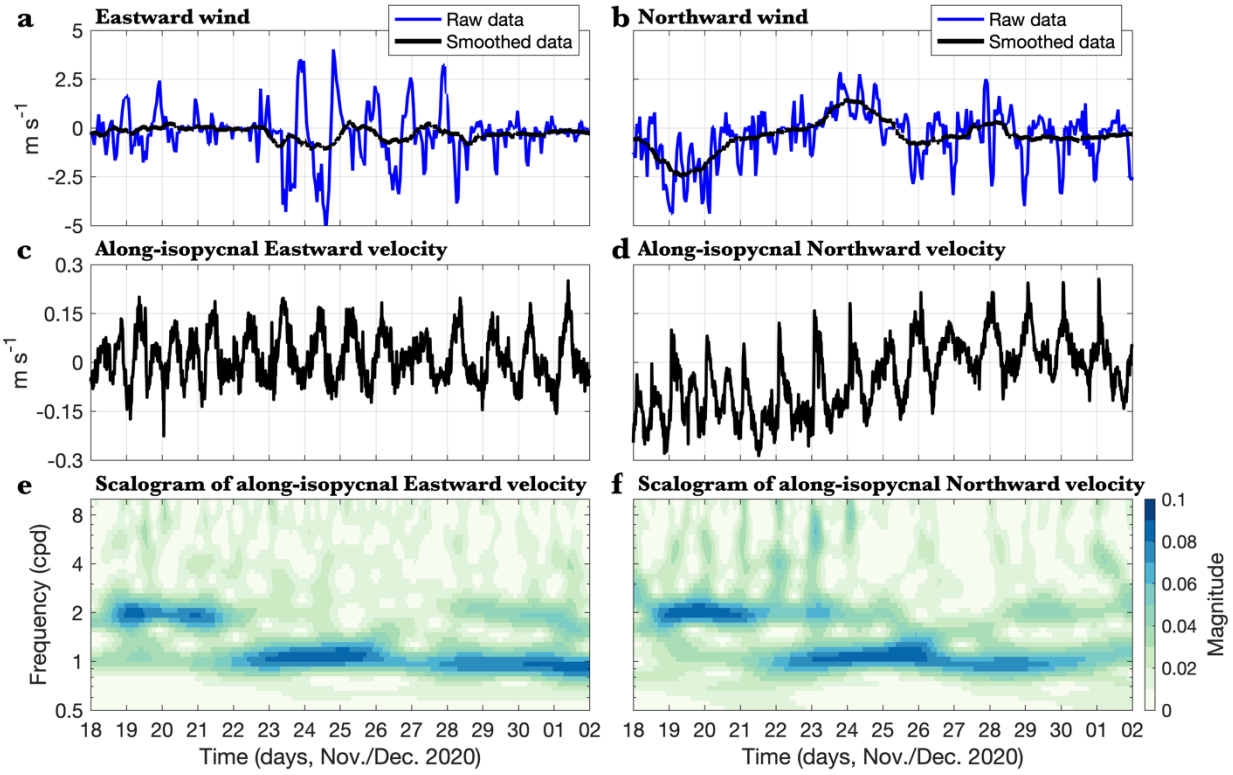

Figure 3.8 Wind and velocity measurements. a,b) Eastward and Northward wind measured at the SIO pier, with raw data in blue and 1-day running mean averaged data in black. c,d) depth-averaged Eastward and Northward velocity in the density layer between $\sigma 0$ 24.6 kg m^{-3} and 24.84 kg m^{-3} at the Del Mar mooring. e,f) scalograms showing wavelet analysis results performed onto the corresponding velocity time series in c,d.

The near-inertial waves that likely caused the observed nitrate signal were probably generated by winds. We observed that the dominant frequency of the velocity changed from ~2 cpd to ~1 cpd on Nov. 22, coinciding with a peak in the cross-shore wind (approximated by Eastward wind with respect to the nearly North-South-directed shoreline, Fig. 3.1a), which lasted several days (Fig. 3.8a). This is a common scenario for wind-generated near-inertial waves (Alford

et al. 2016b). Moreover, the along-isopycnal velocity field exhibited a clear upward phase, indicating downward energy propagation (e.g., Alford et al. 2016b), consistent with energy being transferred from the atmosphere to the ocean.

The second step to test the NIW-advection hypothesis involves investigating whether it would result in a constant estimated cross-shore nitrate gradient, and if so, whether this gradient matches the observed pattern. To do this, we utilized the PVD technique, which allows us to track the source locations of water parcels and estimate the spatial pattern of nitrate. We focused solely on the cross-shore component, and the results, shown in Fig. 3.9, indicate a consistently positive onshore nitrate gradient with an average slope of 0.83 mmol m^{-3} km^{-1} (median value of all individual slope estimations). This gradient is almost identical to the value obtained from nitrate measurements via the three moorings alone (0.75 mmol m^{-3} km^{-1}, Fig. 3.5), providing a second piece of evidence supporting the NIW-advection hypothesis.

Lucas et al. (2011) have demonstrated that the onshore-directed horizontal nitrate flux, which is mainly driven by internal tides, is the primary source of nitrate for sustaining the elevated primary productivity observed over the inner continental shelf region of the SCB. In this study, we extend this understanding by presenting evidence that the onshore region can also act as a nitrate source that supports offshore primary productivity via an offshore-directed horizontal nitrate flux mechanism. This mechanism requires a combination of an onshore-directed nitrate gradient and waves that drive advective processes.

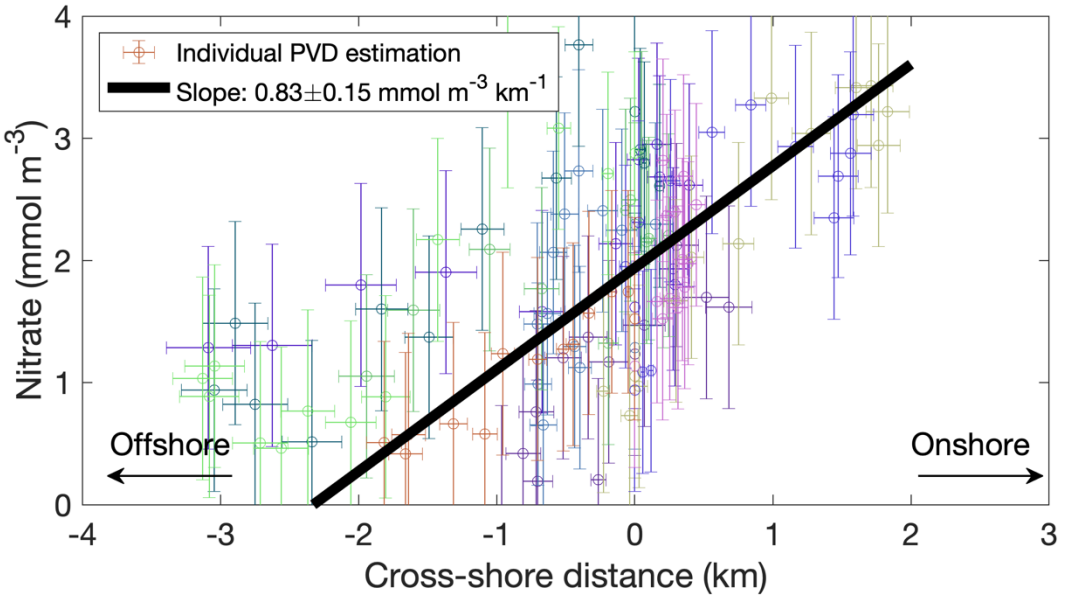

Figure 3.9 Progressive vector diagram (PVD)-estimated along-isopycnal cross-shore nitrate gradient. Each point is estimated from Wirewalker-measured nitrate concentration and Del Mar Mooring-measured velocity at the density layer -- σ_0 24.6 kg m^{-3} to 24.84 kg m^{-3} from the noon of Nov. 22 to the noon of Nov. 27. Data points of the same color represent the PVD estimation within each 12-hour segment. The solid black line is drawn from the median value of the slopes and intercepts obtained from least-squares fitting PVD estimations in all 12-hour segments. The error bar associated with nitrate concentration is determined by the Wirewalker nitrate measurements, the error bar associated with cross-shore distance is calculated from error propagation, and the error bar associated with the slope is calculated from the standard error of the slope under the linear regression theorem.

Conclusion

In summary, our study has uncovered a previously undocumented cross-shore nitrate gradient with elevated nitrate onshore over the inner continental shelf of Southern California Bight. We have provided evidence that the nitrate source at the onshore end was due to enhanced vertical turbulent nitrate flux in the bottom boundary layer, driven by energetic internal waves. The near-inertial internal waves were responsible for transporting the onshore nitrate offshore at a near-diurnal time scale, providing a novel mechanism for the onshore side of the inner continental shelf to fuel the primary productivity offshore.

Our study highlights the complex interplay between air, sea, and sea-floor interactions in coastal nitrate dynamics, which are temporally variable on multiple scales and spatially dependent. It is essential to incorporate these newly identified small-scale nitrate dynamics into relevant models to improve projections of coastal biogeochemistry, ranging from short-term coastal primary productivity estimations to long-term ecological predictions under the changing climate.

We also emphasize the importance of future observational campaigns to unveil and quantify the mechanistic processes governing nitrate dynamics, including its source, transport, and temporal-spatial patterns. An interdisciplinary approach is needed to measure relevant physical and biogeochemical variabilities with adequate spatial and temporal resolutions and coverages. This includes not only long-term monitoring with mooring arrays or spatially and temporally resolved moving instrument platforms such as gliders or floats but also short-term surveys on targeted oceanic features with additional ship-based operations. Fortunately, there has been a much-improved coverage of nitrate measurements, as well as other physical and biogeochemical variables, both globally (e.g., Claustre et al. 2020) and regionally (e.g., Oliver et al. 2022) over the past decade, which ultimately advances our understanding of ocean biogeochemical cycles.

Chapter 3, in part is currently being prepared for submission for publication of the material. Zheng, B., Lucas, A.J., Schlosser, T., Anderson, C., Send, U., Davis, K. (2023). The dissertation author was the primary researcher and author of this material.

REFERENCES

Alberty, M. S., S. Billheimer, M. M. Hamann, C. Y. Ou, V. Tamsitt, A. J. Lucas, and M. H. Alford, 2017: A reflecting, steepening, and breaking internal tide in a submarine canyon. *J. Geophys. Res. Ocean.*, **122**, 6872–6882, https://doi.org/10.1002/2016JC012583.

Alford, M. H., 2010: Sustained, Full-water-column observations of internal waves and mixing near Mendocino Escarpment. *J. Phys. Oceanogr.*, **40**, 2643–2660, https://doi.org/10.1175/2010JPO4502.1.

——, J. A. Mackinnon, H. L. Simmons, and J. D. Nash, 2016: Near-Inertial Internal Gravity Waves in the Ocean. *Ann. Rev. Mar. Sci.*, **8**, 95–123, https://doi.org/10.1146/annurev-marine-010814-015746.

Allen, W. E. ., 1938: "Red Water" along the West Coast of the United States in 1938. *Science (80-.).*, **88**, 55–56.

——, 1941: Twenty Years' Statistical Studies of Marine Plankton Dinoflagellates of Southern California. *Am. Midl. Nat.*, **26**, 603–635.

——, 1943: "Red Water" in La Jolla Bay in 1942. *Trans. Am. Microsc. Soc.*, **62**, 262–264.

——, 1946: "Red Water" in La Jolla Bay in 1945. *Trans. Am. Microsc. Soc.*, **65**, 149–153.

Anderson, C. R., S. K. Moore, M. C. Tomlinson, J. Silke, and C. K. Cusack, 2015: *Living with Harmful Algal Blooms in a Changing World: Strategies for Modeling and Mitigating Their Effects in Coastal Marine Ecosystems*. Elsevier Inc., 495–561 pp.

Anderson, D. M., A. D. Cembella, and G. M. Hallegraeff, 2012: Progress in understanding harmful algal blooms: Paradigm shifts and new technologies for research, monitoring, and management. *Ann. Rev. Mar. Sci.*, **4**, 143–176, https://doi.org/10.1146/annurev-marine-120308-081121.

——, and Coauthors, 2021: Marine harmful algal blooms (HABs) in the United States: History, current status and future trends. *Harmful Algae*, **102**, 101975, https://doi.org/10.1016/j.hal.2021.101975.

De Baar, H. J. W., 1994: von Liebig ' s Law of the Minimum and Plankton Ecology (1899-1991). *Prog. Oceanogr.*, **33**, 347–386.

Berdalet, E., and Coauthors, 2014: Understanding harmful algae in stratified systems: Review of progress and future directions. *Deep. Res. Part II Top. Stud. Oceanogr.*, **101**, 4–20, https://doi.org/10.1016/j.dsr2.2013.09.042.

Bluteau, C. E., N. L. Jones, and G. N. Ivey, 2016: Acquiring long-term turbulence measurements from moored platforms impacted by motion. *J. Atmos. Ocean. Technol.*, **33**, 2535–2551,

https://doi.org/10.1175/JTECH-D-16-0041.1.

Le Boyer, A., M. H. Alford, R. Pinkel, T. D. Hennon, Y. J. Yang, D. Ko, and J. Nash, 2020: Frequency Shift of Near-Inertial Waves in the South China Sea. *J. Phys. Oceanogr.*, **50**, 1121–1135, https://doi.org/10.1175/jpo-d-19-0103.1.

Brunson, J. K., and Coauthors, 2018: Biosynthesis of the neurotoxin domoic acid in a bloom-forming diatom. **1358**, 1356–1358.

Carlson, D. F., P. A. Muscarella, H. Gildor, B. L. Lipphardt, and E. Fredj, 2010: How useful are progressive vector diagrams for studying coastal ocean transport? *Limnol. Oceanogr. Methods*, **8**, 98–106, https://doi.org/10.4319/lom.2010.8.0098.

Claustre, H., K. S. Johnson, and Y. Takeshita, 2020: Observing the Global Ocean with Biogeochemical-Argo. *Ann. Rev. Mar. Sci.*, **12**, 23–48, https://doi.org/10.1146/annurev-marine-010419-010956.

Cullen, J. J., 1985: Diel vertical migration by dinoflagellates: roles of carbohydrate metabolism and behavioral flexibility. *Contrib. Mar. Sci*, **27**, 135–152.

Davis, R. E., M. D. Ohman, D. L. Rudnick, J. T. Sherman, and B. Hodges, 2008: Glider surveillance of physics and biology in the southern California Current System. *Limnol. Oceanogr.*, **53**, 2151–2168, https://doi.org/10.4319/lo.2008.53.5_part_2.2151.

Duda, T. F., and C. S. Cox, 1989: Vertical wave number spectra of velocity and shear at small internal wave scales. *J. Geophys. Res.*, **94**, 939, https://doi.org/10.1029/jc094ic01p00939.

Dugdale, R. C., and J. J. Goering, 1967: Uptake of New and Regenerated Forms of Nitrogen in Primary Productivity. *Limnol. Oceanogr.*, **12**, 196–206, https://doi.org/10.4319/lo.1967.12.2.0196.

Eppley, R. W., 1992: Chlorophyll, photosynthesis and new production in the Southern California Bight. *Prog. Oceanogr.*, **30**, 117–150, https://doi.org/10.1016/0079-6611(92)90010-W.

Eppley, R. W., and W. G. Harrison, 1975: Physiological ecology of Gonyaulax polyedra, a red water dinoflagellate off southern California. *Proceedings of THE FIRST INTERNATIONAL CONFERENCE ON TOXIC DINOFLAGELLATE BLOOMS*, 11–22.

Eppley, R. W., O. Holm-Hansen, and J. D. H. Strickland, 1968: SOME OBSERVATIONS ON THE VERTICAL MIGRATION OF DINOFLAGELLATES. *J. Phycol.*, **4**, 330–340.

Eppley, R. W., E. H. Renger, and W. G. Harrison, 1979: Nitrate and phytoplankton production in southern California coastal waters. *Limnol. Oceanogr.*, **24**, 483–494, https://doi.org/10.4319/lo.1979.24.3.0483.

Falkowski, P. G., R. T. Barber, and V. Smetacek, 1998: Biogeochemical controls and feedbacks

on ocean primary production. *Science (80-.).*, **281**, 200–206, https://doi.org/10.1126/science.281.5374.200.

Firing, E., 1959: Deep Ocean Acoustic Doppler Current Profiling. *Nucl. Phys.*, Vol. 13 of, 104–116.

Flament, P., 2002: A state variable for characterizing water masses and their diffusive stability: Spiciness. *Prog. Oceanogr.*, **54**, 493–501, https://doi.org/10.1016/S0079-6611(02)00065-4.

Franks, P. J. S., 2018: Recent Advances in Modelling of Harmful Algal Blooms. 359–377, https://doi.org/10.1007/978-3-319-70069-4_19.

Garwood, J. C., A. J. Lucas, P. Naughton, M. H. Alford, P. L. D. Roberts, J. S. Jaffe, L. deGelleke, and P. J. S. Franks, 2020: A novel cross-shore transport mechanism revealed by subsurface, robotic larval mimics: Internal wave deformation of the background velocity field. *Limnol. Oceanogr.*, **65**, 1456–1470, https://doi.org/10.1002/lno.11400.

——, ——, ——, P. L. D. Roberts, J. S. Jaffe, L. deGelleke, and P. J. S. Franks, 2021: Larval cross-shore transport estimated from internal waves with a background flow: The effects of larval vertical position and depth regulation. *Limnol. Oceanogr.*, **66**, 678–693, https://doi.org/10.1002/lno.11632.

Guerra, M., and J. Thomson, 2017: Turbulence measurements from five-beam acoustic doppler current profilers. *J. Atmos. Ocean. Technol.*, **34**, 1267–1284, https://doi.org/10.1175/JTECH-D-16-0148.1.

Guerra, M. (2021). Retrieved from https://github.com/mguerrap/5Beam- Turbulence-Methods.

Guidi, L., and Coauthors, 2016: Plankton networks driving carbon export in the oligotrophic ocean. *Nature*, **532**, 465–470, https://doi.org/10.1038/nature16942.

Haas, S., B. M. Robicheau, S. Rakshit, J. Tolman, C. K. Algar, J. LaRoche, and D. W. R. Wallace, 2021: Physical mixing in coastal waters controls and decouples nitrification via biomass dilution. *Proc. Natl. Acad. Sci. U. S. A.*, **118**, https://doi.org/10.1073/pnas.2004877118.

Hamann, M. M., 2019: The dynamics of internal tides and mixing in coastal systems. 168 pp.

Hand, W. G., P. A. Collard, and D. Davenport, 1965: The effects of temperature and salinity change on swimming rate in the dinoflagellates, Gonyaulax and Gyrodinium. *Biol. Bull.*, **128**, 90–101.

Harding, S., L. Kilcher, and J. Thomson, 2017: Turbulence measurements from compliant moorings. Part I: Motion characterization. *J. Atmos. Ocean. Technol.*, **34**, 1235–1247, https://doi.org/10.1175/JTECH-D-16-0189.1.

Harrison, W. G., 1976: Nitrate metabolism of the red tide dinoflagellate Gonyaulax polyedra Stein. *J. Exp. Mar. Bio. Ecol.*, **21**, 199–209, https://doi.org/10.1016/0022-0981(76)90115-5.

Hasle, G. R., 1950: Phototactic vertical migration in marine dinoflagellates. **2**, 162–175.

Heaney, S. I., and R. W. Eppley, 1981: Light, temperature and nitrogen as interacting factors affecting diel vertical migrations of dinoflagellates in culture. *J. Plankton Res.*, **3**, 331–344, https://doi.org/10.1093/plankt/3.2.331.

Holmes, R. W., P. M. Williams, and R. W. Eppley, 1967: RED WATER IN LA JOLLA BAY, 1964-1966. *Limonology Oceanogr.*, **12**, 503–512.

Howard, M. D. A., and Coauthors, 2014: Anthropogenic nutrient sources rival natural sources on small scales in the coastal waters of the Southern California Bight. *Limnol. Oceanogr.*, **59**, 285–297, https://doi.org/10.4319/lo.2014.59.1.0285.

Howarth, R. W., 1988: Nutrient Limitation of Net Primary Production in Marine Ecosystems. *Annu. Rev. Ecol. Syst.*, **19**, 89–110.

Jacox, M. G., C. A. Edwards, E. L. Hazen, and S. J. Bograd, 2018: Coastal Upwelling Revisited: Ekman, Bakun, and Improved Upwelling Indices for the U.S. West Coast. *J. Geophys. Res. Ocean.*, **123**, 7332–7350, https://doi.org/10.1029/2018JC014187.

Jeong, H. J., and Coauthors, 2015: A hierarchy of conceptual models of red-tide generation : Nutrition , behavior , and biological interactions. *Harmful Algae*, **47**, 97–115, https://doi.org/10.1016/j.hal.2015.06.004.

Johnson, K. S., 2010: Simultaneous measurements of nitrate, oxygen, and carbon dioxide on oceanographic moorings: Observing the Redfield ratio in real time. *Limnol. Oceanogr.*, **55**, 615–627, https://doi.org/10.4319/lo.2009.55.2.0615.

——, and L. J. Coletti, 2002: In situ ultraviolet spectrophotometry for high resolution and long-term monitoring of nitrate, bromide and bisulfide in the ocean. *Deep. Res. Part I Oceanogr. Res. Pap.*, **49**, 1291–1305, https://doi.org/10.1016/S0967-0637(02)00020-1.

——, J. N. Plant, J. P. Dunne, L. D. Talley, and J. L. Sarmiento, 2017: Annual nitrate drawdown observed by SOCCOM profiling floats and the relationship to annual net community production. *J. Geophys. Res. Ocean.*, **122**, 6668–6683, https://doi.org/10.1002/2017JC012839.

——, T. Maurer, J. Plant, H. Bittig, C. Schallenberg, and C. Schmechtig, 2021: *BGC-Argo quality control manual for nitrate concentration*. 1–28 pp.

Kahru, M., and Coauthors, 2021: Satellite detection of dinoflagellate blooms off California by UV reflectance ratios. *Elementa*, **9**, 1–10, https://doi.org/10.1525/elementa.2020.00157.

Kamykowski, D., 1981: Laboratory experiments on the diurnal vertical migration of marine dinoflagellates through temperature gradients. *Mar. Biol.*, **62**, 57–64, https://doi.org/10.1007/BF00396951.

Kamykowski, D., and S.-J. Zentara, 1977: The diurnal vertical migration of motile phytoplankton through temperature gradients. *Limnol. Oceanogr.*, **22**, 148–151, https://doi.org/10.31392/iscs.2021.18.099.

Kenitz, K. M., and Coauthors, 2023: Environmental and ecological drivers of harmful algal blooms revealed by automated underwater microscopy. *Limnol. Oceanogr.*, 1–18, https://doi.org/10.1002/lno.12297.

Kessouri, F., and Coauthors, 2021: Coastal eutrophication drives acidification, oxygen loss, and ecosystem change in a major oceanic upwelling system. *Proc. Natl. Acad. Sci. U. S. A.*, **118**, 1–8, https://doi.org/10.1073/pnas.2018856118.

Kilcher, L. F., J. Thomson, S. Harding, and S. Nylund, 2017: Turbulence Measurements from Compliant Moorings. Part II: Motion Correction. *J. Atmos. Ocean. Technol.*, **34**, 1249–1266, https://doi.org/10.1175/jtech-d-16-0213.1.

Lewis, J., and R. Hallett, 1997: LINGULODINIUM POLYEDRUM (GONYAULAX POLYEDRA) A BLOOMING DINOFLAGELLATE. *Oceanogr. Mar. Biol. an Annu. Rev.*, **35**, 89–153.

Lewis, M. R., W. G. Harrison, N. S. Oakey, D. Hebert, and T. Platr, 1986: Vertical Nitrate Fluxes in the Oligotrophic Ocean. *Science (80-.).*, **234**, 870–873.

Li, Q. P., P. J. S. Franks, M. D. Ohman, and M. R. Landry, 2012: Enhanced nitrate fluxes and biological processes at a frontal zone in the southern California current system. *J. Plankton Res.*, **34**, 790–801, https://doi.org/10.1093/plankt/fbs006.

Lilly, L. E., U. Send, M. Lankhorst, T. R. Martz, R. A. Feely, A. J. Sutton, and M. D. Ohman, 2019: Biogeochemical Anomalies at Two Southern California Current System Moorings During the 2014–2016 Warm Anomaly-El Niño Sequence. *J. Geophys. Res. Ocean.*, **124**, 6886–6903, https://doi.org/10.1029/2019JC015255.

Lucas, A., R. Pinkel, and M. Alford, 2017: Ocean Wave Energy for Long Endurance, Broad Bandwidth Ocean Monitoring. *Oceanography*, **30**, 126–127, https://doi.org/10.5670/oceanog.2017.232.

Lucas, A. J., C. L. Dupont, V. Tai, J. L. Largier, B. Palenik, and P. J. S. Franks, 2011a: The green ribbon: Multiscale physical control of phytoplankton productivity and community structure over a narrow continental shelf. *Limnol. Oceanogr.*, **56**, 611–626, https://doi.org/10.4319/lo.2011.56.2.0611.

——, P. J. S. Franks, and C. L. Dupont, 2011b: Horizontal internal-tide fluxes support elevated phytoplankton productivity over the inner continental shelf. *Limnol. Oceanogr. Fluids Environ.*, **1**, 56–74, https://doi.org/10.1215/21573698-1258185.

——, and Coauthors, 2016: Adrift upon a salinity-stratified sea. *Oceanography*, **29**, 134–145, https://doi.org/10.5670/oceanog.2016.46.

Lyon, G. S., and E. D. Stein, 2009: How effective has the Clean Water Act been at reducing pollutant mass emissions to the Southern California Bight over the past 35 years? *Environ. Monit. Assess.*, **154**, 413–426, https://doi.org/10.1007/s10661-008-0408-1.

MacKinnon, J. A., and M. C. Gregg, 2005: Spring mixing: Turbulence and internal waves during restratification on the New England shelf. *J. Phys. Oceanogr.*, **35**, 2425–2443, https://doi.org/10.1175/JPO2821.1.

Mayali, X., P. J. S. Franks, Y. Tanaka, and F. Azam, 2008: Bacteria-induced motility reduction in Lingulodinium polyedrum (Dinophyceae). *J. Phycol.*, **44**, 923–928, https://doi.org/10.1111/j.1529-8817.2008.00549.x.

Mclaughlin, K., and Coauthors, 2021: Influence of anthropogenic nutrient inputs on rates of coastal ocean nitrogen and carbon cycling in the Southern California Bight , United States. 1–24.

McPhee-Shaw, E. E., D. A. Siegel, L. Washburn, M. A. Brzezinski, J. L. Jones, A. Leydecker, and J. Melack, 2007: Mechanisms for nutrient delivery to the inner shelf: Observations from the Santa Barbara Channel. *Limnol. Oceanogr.*, **52**, 1748–1766, https://doi.org/10.4319/lo.2007.52.5.1748.

Moberg, E. G., 1928: The Interrelation between Diatoms, Their Chemical Environment, and Upwelling Water in the Sea, Off the Coast of Southern California. *Proc. Natl. Acad. Sci.*, **14**, 511–518, https://doi.org/10.1073/pnas.14.7.511.

Morrison, A. K., D. W. Waugh, A. M. C. Hogg, D. C. Jones, and R. P. Abernathey, 2022: Ventilation of the Southern Ocean Pycnocline. *Ann. Rev. Mar. Sci.*, **14**, 405–430, https://doi.org/10.1146/annurev-marine-010419-011012.

Naveira Garabato, A. C., and Coauthors, 2019: Rapid mixing and exchange of deep-ocean waters in an abyssal boundary current. *Proc. Natl. Acad. Sci. U. S. A.*, **116**, 13233–13238, https://doi.org/10.1073/pnas.1904087116.

Nortek. (2011). Retrieved from www.nortekgroup.com/products/signature-1000

Nortek. (2020). Retrieved from https://support.nortekgroup.com/hc/en-us/articles/360029820971- How-is-a-coordinate-transformation-done-

Oliver, H., W. G. Zhang, K. M. Archibald, A. J. Hirzel, W. O. Smith, H. M. Sosik, R. H. R.

Stanley, and D. J. McGillicuddy, 2022: Ephemeral Surface Chlorophyll Enhancement at the New England Shelf Break Driven by Ekman Restratification. *J. Geophys. Res. Ocean.*, **127**, 1–17, https://doi.org/10.1029/2021JC017715.

Olson, R. J., and H. M. Sosik, 2007: A submersible imaging-in-flow instrument to analyze nano- and microplankton: Imaging FlowCytobot. *Limnol. Oceanogr. Methods*, **5**, 195–203, https://doi.org/10.4319/lom.2007.5.195.

Omand, M. M., F. Feddersen, R. T. Guza, and P. J. S. Franks, 2012: Episodic vertical nutrient fluxes and nearshore phytoplankton blooms in Southern California. *Limnol. Oceanogr.*, **57**, 1673–1688, https://doi.org/10.4319/lo.2012.57.6.1673.

Osborn, T. R., 1980: Estimates of the Local Rate of Vertical Diffusion from Dissipation Measurements. *J. Phys. Oceanogr.*, **10**, 83–89.

Peacock, M. B., and R. M. Kudela, 2014: Evidence for active vertical migration by two dinoflagellates experiencing iron, nitrogen, and phosphorus limitation. *Limnol. Oceanogr.*, **59**, 660–673, https://doi.org/10.4319/lo.2014.59.3.0660.

Pinkel, R., 1980: Acoustic Doppler Techniques. *Air-Sea Interact. Instruments Methods*, 171–199, https://doi.org/10.1007/978-1-4615-9182-5.

Pinkel, R., 1983: Doppler sonar observations of internal waves, wave- field structure. *J. Phys. Oceanogr.*, **13**, 804–815.

——, and S. Anderson, 1997: Shear, strain, and Richardson number variations in the thermocline. Part I: Statistical description. *J. Phys. Oceanogr.*, **27**, 264–290, https://doi.org/10.1175/1520-0485(1997)027<0264:ssarnv>2.0.co;2.

Pinkel, R., M. A. Goldin, J. A. Smith, O. M. Sun, A. A. Aja, M. N. Bui, and T. Hughen, 2011: The Wirewalker: A vertically profiling instrument carrier powered by ocean waves. *J. Atmos. Ocean. Technol.*, **28**, 426–435, https://doi.org/10.1175/2010JTECHO805.1.

Prezelin, B. B., G. Samuelsson, and H. A. Matlick, 1986: Photosystem II photoinhibition and altered kinetics of photosynthesis during nutrient-dependent high-light photoadaptation in Gonyaulax polyedra. *Mar. Biol.*, **93**, 1–12, https://doi.org/10.1038/283903a0.

Rainville, L., and R. Pinkel, 2001: Wirewalker: An autonomous wave-powered vertical profiler. *J. Atmos. Ocean. Technol.*, **18**, 1048–1051, https://doi.org/10.1175/1520-0426(2001)018<1048:WAAWPV>2.0.CO;2.

Ralston, D. K., and S. K. Moore, 2020: Modeling harmful algal blooms in a changing climate. *Harmful Algae*, **91**, 101729, https://doi.org/10.1016/j.hal.2019.101729.

Ritzman, J., A. Brodbeck, S. Brostrom, S. McGrew, S. Dreyer, T. Klinger, and S. K. Moore, 2018: Economic and sociocultural impacts of fisheries closures in two fishing-dependent

communities following the massive 2015 U.S. West Coast harmful algal bloom. *Harmful Algae*, **80**, 35–45, https://doi.org/10.1016/j.hal.2018.09.002.

Roemmich, D., 1989: Mean transport of mass, heat, salt and nutrients in southern California coastal waters: implications for primary production and nutrient cycling. *Deep Sea Res. Part A, Oceanogr. Res. Pap.*, **36**, 1359–1378, https://doi.org/10.1016/0198-0149(89)90088-5.

Sakamoto, C. M., K. S. Johnson, and L. J. Coletti, 2009: Improved algorithm for the computation of nitrate concentrations in seawater using an in situ ultraviolet spectrophotometer. *Limnol. Oceanogr. Methods*, **7**, 132–143, https://doi.org/10.1002/lom3.10209.

Sakamoto, C. M., K. S. Johnson, L. J. Coletti, T. L. Maurer, G. Massion, J. T. Pennington, J. N. Plant, and H. W. Jannasch, 2017: HOURLY IN SITU NITRATE ON A COASTAL MOORING. *Oceanography*, **30**, 114–127.

Schlosser, T., Lucas, A. J., Omand, M., & Farrar, T. (2023). Monsoons, plumes, and blooms: intraseasonal variability of subsurface primary productivity in the Bay of Bengal. *[Manuscript submitted for publication]*.

Sengupta, A., F. Carrara, and R. Stocker, 2017: Phytoplankton can actively diversify their migration strategy in response to turbulent cues. *Nature*, **543**, 555–558, https://doi.org/10.1038/nature21415.

Shcherbina, A. Y., E. A. D'Asaro, and S. Nylund, 2018: Observing finescale oceanic velocity structure with an autonomous nortek acoustic doppler current profiler. *J. Atmos. Ocean. Technol.*, **35**, 411–427, https://doi.org/10.1175/JTECH-D-17-0108.1.

Simpson, J. H., & Sharples, J. (n.d.). *Introduction to the Physical and Biological Oceanography of Shelf Seas.* Cambridge University Press.

Smayda, T. J., 2002: Turbulence , watermass stratification and harmful algal blooms : an alternative view and frontal zones as " pelagic seed banks ." **1**, 95–112.

Smith, P. ., and R. W. Eppley, 1982: Primary production and the anchovy population in the Southern California Bight: Comparison of time series. *Limnol. Oceanogr.*, **27**, 1–17.

Sosik, H. M., and R. J. Olson, 2007: Automated taxonomic classification of phytoplankton sampled with imaging-in-flow cytometry. *Limnol. Oceanogr. Methods*, **5**, 204–216, https://doi.org/10.4319/lom.2007.5.204.

Spilling, K., K. Olli, J. Lehtoranta, A. Kremp, and L. Tedesco, 2018: Shifting Diatom — Dinoflagellate Dominance During Spring Bloom in the Baltic Sea and its Potential Effects on Biogeochemical Cycling. **5**, 1–17, https://doi.org/10.3389/fmars.2018.00327.

Sutula, M., M. Ho, A. Sengupta, F. Kessouri, K. McLaughlin, K. McCune, and D. Bianchi, 2021:

A baseline of terrestrial freshwater and nitrogen fluxes to the Southern California Bight, USA. *Mar. Pollut. Bull.*, **170**, 112669, https://doi.org/10.1016/j.marpolbul.2021.112669.

Taylor, J. (1997). *An Introduction to Error Analysis: The Study of Uncertainties in Physical Measurements.* University Science Books.

Todd, R. E., D. L. Rudnick, and R. E. Davis, 2009: Monitoring the greater San Pedro Bay region using autonomous underwater gliders during fall of 2006. *J. Geophys. Res. Ocean.*, **114**, 1–13, https://doi.org/10.1029/2008JC005086.

——, ——, J. T. Sherman, W. Brechner Owens, and L. George, 2017: Absolute velocity estimates from autonomous underwater gliders equipped with doppler current profilers. *J. Atmos. Ocean. Technol.*, **34**, 309–333, https://doi.org/10.1175/JTECH-D-16-0156.1.

Torrey, H. B., 1902: An unusual occurrence of dinoflagellata on the California coast. *Am. Nat.*, **36**, 187–192.

Trowbridge, J. H., and S. J. Lentz, 2018: The Bottom Boundary Layer. *Ann. Rev. Mar. Sci.*, **10**, 397–420, https://doi.org/10.1146/annurev-marine-121916-063351.

Ward, B., Arp, D., & Klotz, M. (2011). *Nitrification.* American Society for Microbiology Press.

Ward, B. B., R. J. Olson, and M. J. Perry, 1982: Microbial nitrification rates in the primary nitrite maximum off southern California. *Deep. Res. Part A-Oceanographic Res. Pap.*, **29**, 247–255.

Wilkerson, F. P., and R. C. Dugdale, 1987: The use of large shipboard barrels and drifters to study the effects of coastal upwelling on phytoplankton dynamics,. *Limnol. Oceanogr.*, **32**, 368–382, https://doi.org/10.4319/lo.1987.32.2.0368.

Winters, K. B., 2015: Tidally driven mixing and dissipation in the stratified boundary layer above steep submarine topography. *Geophys. Res. Lett.*, **42**, 7123–7130, https://doi.org/10.1002/2015GL064676.

Zheng, B., Lucas, A., Franks, P., Schlosser, T., Anderson, C., Send, U., Barton, A. (2023). Dinoflagellate vertical migration fuels an intense red tide. *[submitted]*.

Zippela, S. F., J. Thomson, and G. Farquharson, 2018: Turbulence from breaking surface waves at a River mouth. *J. Phys. Oceanogr.*, **48**, 435–453, https://doi.org/10.1175/jpo-d-17-0122.1.